

Enabling Chemically Accurate Quantum Phase Estimation in the Early Fault-Tolerant Regime

Shota Kanasugi,^{1,2,*} Riki Toshio,^{1,2} Kazunori Maruyama,^{1,2} and Hiroataka Oshima^{1,2}

¹*Quantum Laboratory, Fujitsu Research, Fujitsu Limited, 4-1-1 Kamikodanaka, Nakahara, Kawasaki, Kanagawa 211-8588, Japan*

²*Fujitsu Quantum Computing Joint Research Division, Center for Quantum Information and Quantum Biology, Osaka University, 1-2 Machikaneyama, Toyonaka, Osaka, 565-8531, Japan*

(Dated: March 31, 2026)

Quantum simulation of molecular electronic structure is one of the most promising applications of quantum computing. However, achieving chemically accurate predictions for strongly correlated systems requires quantum phase estimation (QPE) on fault-tolerant quantum computing (FTQC) devices. Existing resource estimates for typical FTQC architectures suggest that such calculations demand millions of physical qubits, thereby placing them beyond the reach of near-term devices. Here, we investigate the feasibility of performing QPE for chemically relevant molecular systems in an early-FTQC regime, characterized by partial fault tolerance, constrained qubit budgets, and limited circuit depth. Our framework is based on single-ancilla, Trotter-based QPE implementations combined with partially randomized time evolution. Within this framework, we develop a novel Hamiltonian optimization strategy, termed unitary weight concentration, that reduces algorithmic cost by reshaping linear-combination-of-unitaries representations. Applying this framework to active-space models of iron–sulfur clusters, cytochrome P450 active sites, and CO₂-utilization catalysts, we perform end-to-end resource estimation using the latest version of the space-time efficient analog rotation (STAR) architecture. Our results indicate that **ground-state energy estimation for active spaces of approximately 20–50 spatial orbitals—well beyond the reach of classical full configuration interaction—is achievable using $\sim 10^5$ physical qubits, with runtimes on the order of days to weeks.** These findings demonstrate that while full-fledged fault-tolerant quantum computers will be required for even larger molecular simulations, chemically meaningful quantum chemistry problems are already within reach in an experimentally relevant, early-FTQC regime.

I. INTRODUCTION

Quantum simulation of molecular electronic structures represents one of the most compelling applications of quantum computing. At its core, this promise stems from the fact that strongly correlated molecules often require a multireference description that treats a large set of partially occupied orbitals on an equal footing. In such regimes, complete active-space approaches must contend with an exponentially growing configuration space to capture near-degeneracy and many-body entanglement effects [1]. This exponential scaling ultimately limits the size of active spaces that can be treated exactly on classical computers, restricting full configuration interaction (full-CI) calculations to roughly 20 electrons in 20 (spatial) orbitals [2, 3], a scale often insufficient for chemically relevant transition-metal complexes and catalytic intermediates.

To extend applicability beyond this regime, classical heuristic approaches such as coupled-cluster theory [4], selected configuration interaction methods [5], and tensor-network methods like the density matrix renormalization group (DMRG) [6, 7] have been developed. However, their accuracy often relies on heuristic assumptions about wavefunction structure, and they generally lack systematically controlled guarantees at the

level of chemical accuracy required for reliable prediction of reaction energetics and catalytic processes [8]. These limitations motivate the exploration of quantum-computational approaches that offer a path toward controllable and certifiable accuracy beyond the classical frontier [9–11].

Recent progress in noisy intermediate-scale quantum (NISQ) hardware has enabled proof-of-principle demonstrations of quantum–classical hybrid algorithms, including the variational quantum eigensolver [12] and quantum-selected configuration interaction [13] (also known as sample-based quantum diagonalization [14]). These approaches aim to circumvent the exponential scaling of classical exact methods by leveraging quantum state preparation and measurement. However, their achievable accuracy strongly depends on ansatz design, optimization heuristics, and hardware noise. Moreover, their scalability to larger systems remains limited due to issues such as barren plateaus [15], measurement overhead [16], and increasing circuit complexity [17]. Crucially, they generally do not provide certified guarantees of achieving chemical accuracy, making it difficult to establish a definitive quantum advantage for high-precision quantum chemistry.

In contrast, quantum phase estimation (QPE) [18] provides a systematically controllable framework for ground-state energy estimation. By projecting onto exact eigenstates within a chosen active space, QPE enables energy calculations with explicitly quantifiable error bounds. As

* kanasugi.shota@fujitsu.com

such, QPE offers a principled route toward achieving chemical accuracy beyond the reach of classical heuristic approaches, such as coupled-cluster and DMRG methods, particularly in regimes where quantitatively reliable energy predictions are required [19]. However, implementing QPE at scale requires fault-tolerant quantum computing (FTQC) that demands millions of physical qubits and substantial space–time overhead for simulating chemically relevant molecular systems, judging from existing resource estimates for typical FTQC architectures. For instance, prior analyses of large transition-metal active sites, such as the iron-molybdenum co-factor (FeMoco), suggest total resource requirements exceeding 10^6 physical qubits under standard surface-code assumptions [20–26]. This places such calculations firmly beyond the reach of near-term quantum hardware.

Recent architectural proposals and experimental advances in quantum error correction suggest the emergence of an intermediate regime of early fault tolerance, bridging NISQ and full-fledged FTQC devices [27–31]. In this regime, quantum processors support encoded logical qubits with imperfect error suppression [27, 28]. Rather than relying on large-scale magic-state distillation and deep circuit decompositions, these architectures aim to reduce space–time overhead through tailored state-preparation protocols and hardware-aware implementations of non-Clifford operations [29–32]. Although such devices do not yet achieve full-fledged fault-tolerant operation, they represent a qualitatively distinct computational regime beyond purely noisy hardware.

A central open question is whether QPE-based electronic-structure calculations for chemically relevant molecules can become practical within this early-FTQC regime, and what resource trade-offs such feasibility would entail. Early-FTQC architectures operate under stringent constraints on logical qubit counts, circuit depth, and tolerable logical-error accumulation. Consequently, feasibility cannot be inferred by simply rescaling resource estimates derived for full-fledged FTQC architectures. Instead, assessing practicality in this regime necessitates an explicit co-design of algorithms, Hamiltonian representations, and architectural constraints imposed by error correction. Determining the parameter regimes in which these elements can be reconciled constitutes the central objective of the present study.

To this end, we introduce *unitary weight concentration* (UWC), a Hamiltonian-optimization technique, and **demonstrate the feasibility of performing** ground-state energy estimation for chemically relevant molecular active-space models on early-FTQC devices operating with $\sim 10^5$ physical qubits. The UWC method restructures the linear-combination-of-unitaries (LCU) Hamiltonian representation via *spectrally-invariant* Hamiltonian transformations, concentrating the coefficient distribution while leaving the eigenvalue spectrum in the target symmetry sector unchanged. In practice, this is achieved by combining orbital optimization (OO) [33, 34] and block-invariant symmetry shift (BLISS) [35, 36] trans-

formations. This leads to reductions in both overall gate cost and circuit depth when combined with *partially randomized* product-formula evolution [37–41]. Across the molecular systems considered, UWC consistently provides an additional order-of-magnitude reduction in total simulation cost beyond partial randomization alone. In this study, we adopt **single-ancilla, Trotter-based QPE implementations** [42–47] compatible with limited qubit budgets, bounded circuit depth, and partial fault tolerance. These implementations therefore depart from the qubitization-based approaches [21–26, 48, 49] typically assumed in resource estimation studies for full-fledged FTQC architectures.

We apply this framework to molecular models of practical relevance, including iron-sulfur clusters [19, 34, 50], cytochrome P450 active-site models [51], and ruthenium-based catalytic complexes for CO_2 utilization [22]. For each system, we construct UWC-optimized Hamiltonian representations and perform end-to-end resource estimation assuming execution on the *space-time efficient analog rotation* (STAR) architecture [29–32], incorporating the latest improvements of logical rotation gate operations, termed *STAR-magic mutation* (SMM) [52]. For each molecular instance, we quantify physical qubit requirements, maximum per-shot runtime, total time-to-solution, and achievable parallelism under fixed qubit-budget assumptions. Our results indicate that **tractable active spaces range from 20 to 50** orbitals using $\sim 10^5$ physical qubits, with total runtimes on the order of days to weeks, while larger systems remain beyond reach in this regime. Importantly, this qubit scale appears to fall within the anticipated single-cryostat range discussed in recent superconducting architectural proposals [53], potentially avoiding distributed FTQC overheads [54]. Although molecular systems in this active-space range remain smaller than those typically envisioned for full-fledged FTQC [20–26, 51, 55], they already extend into a regime that is not only inaccessible to classical full-CI methods [2, 3] but also encompasses chemically and industrially relevant molecular systems [22, 50, 51, 56–58]. Therefore, they represent a scientifically meaningful target for early fault-tolerant quantum simulation. Together, these results delineate a practically meaningful region between classical exact computations and millions-of-qubit full-fledged FTQC and provide a quantitative feasibility map that clarifies the architectural and algorithmic targets for early-FTQC in quantum chemistry.

The rest of the paper is organized as follows. In Sec. II, we introduce single-ancilla QPE and partially randomized product formulas as background for our work. In Sec. III, we describe Hamiltonian representations and our optimization strategy, UWC, for minimizing the partially randomized simulation cost for molecular electronic structure Hamiltonians. In Sec. IV, we present numerical results demonstrating the effectiveness of UWC in reducing the simulation cost of partially randomized QPE for chemically relevant molecular models. In Sec. V, we assess the feasibility of practical chemistry simulation on

early-FTQC hardware by performing comprehensive resource estimation for a range of molecular models on an improved variant of the STAR architecture, SMM. Finally, in Sec. VI, we conclude our discussion and outline future directions toward realizing quantum chemistry simulation in the era of early fault tolerance.

II. SINGLE-ANCILLA QUANTUM PHASE ESTIMATION AND PARTIALLY RANDOMIZED TIME EVOLUTION

In this section, we briefly review the single-ancilla QPE framework and the partially randomized time-evolution schemes upon which our work is built, largely following the presentation in Ref. [41].

A. Single-ancilla quantum phase estimation

First, we review a single-ancilla QPE framework tailored for early fault-tolerant quantum computers. We consider Hamiltonians of the form

$$\hat{H} = \sum_{\ell=1}^L c_{\ell} \hat{P}_{\ell}, \quad (1)$$

where $\hat{P}_{\ell} \in \{I, X, Y, Z\}^{\otimes N_q}$ are N_q -qubit Pauli string operators and $c_{\ell} \in \mathbb{R}$. Although our discussion can be generalized to other LCU representations (e.g., the double-factorized Hamiltonian representation [59]), we focus on this Pauli LCU representation throughout this work. This is because the Trotterized time evolution under the Pauli LCU representation can be implemented using small-angle Pauli rotations that are well suited to the early-FTQC architecture considered in Sec. V, whereas alternative LCU forms typically involve larger-angle operations, such as Givens rotations in the double-factorized Trotterization [59]. For electronic structure Hamiltonians expressed in a basis of N spatial orbitals, the number of qubits is $N_q = 2N$ and the number of terms is $L = \mathcal{O}(N^4)$. In the context of Hamiltonians specified by Eq. (1), we define the total weight or ℓ_1 -norm as

$$\lambda := \sum_{\ell=1}^L |c_{\ell}|. \quad (2)$$

Let $\{E_k, |\psi_k\rangle\}$ denote the eigenpairs of \hat{H} , ordered such that $E_0 \leq E_1 \leq \dots \leq E_d$, where $d = 2^{N_q}$. We assume access to an *initial state* $|\psi\rangle$ with a nonzero overlap with the ground state: $p_0 := |\langle \psi_0 | \psi \rangle|^2 \geq \eta$ for some known lower bound $\eta > 0$. The preparation of such a suitable initial state is a crucial research area in its own right [19, 34, 60–64]. In this work, however, we focus on the implementation cost of single-ancilla QPE itself and do not detail a specific state preparation protocol.

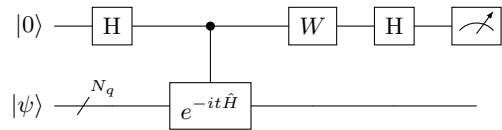


FIG. 1. Circuit for the Hadamard test to measure the expectation value $\langle \psi | e^{-it\hat{H}} | \psi \rangle$. The real part is obtained by setting $W = I$ (identity) and measuring the ancilla in the X basis. The imaginary part is obtained by setting $W = S^\dagger$ and measuring in the Y basis.

The single-ancilla QPE formulation we employ is based on the Hadamard test [42–47]. Starting from the state $|\psi\rangle$ on the data register and $|0\rangle$ on an ancilla qubit, the Hadamard test applies a Hadamard gate H to the ancilla, a controlled time-evolution unitary $e^{-it\hat{H}}$ acting on the data register, and a final rotation and measurement on the ancilla qubit (see Fig. 1). The expectation value of the complex-valued outcome of the Hadamard test $\mathbf{Z}(t)$ is then expressed as

$$g(t) := \mathbb{E}[\mathbf{Z}(t)] = \langle \psi | e^{-it\hat{H}} | \psi \rangle = \sum_k p_k e^{-itE_k}, \quad (3)$$

where $p_k = |\langle \psi_k | \psi \rangle|^2$. Thus, $g(t)$ is a complex signal whose frequency components correspond to the eigenenergies $\{E_k\}$. By sampling $\mathbf{Z}(t)$ at a set of times $\{t_m\}$ and applying an appropriate signal-processing routine, one can estimate E_0 to precision ϵ with Heisenberg-limited scaling in the total evolution time [45–47].

In this work, we specifically use the *robust phase estimation* (RPE) scheme of Ref. [47], as reviewed and analyzed in Ref. [41]. RPE chooses a sequence of evolution times $t_m = 2^m$ for $m = 0, 1, \dots, M$, with $M = \lceil \log_2(\epsilon^{-1}) \rceil$, and uses the outcomes of the Hadamard test at each time to iteratively refine an estimate of E_0 . The details of the procedure are summarized in Appendix A. For a constant ground-state overlap η above a known threshold $4 - 2\sqrt{3} \simeq 0.54$, this scheme achieves Heisenberg-limited scaling in its maximal evolution time $T_{\max} = \max\{t_m\} = \mathcal{O}(\epsilon^{-1})$ and total evolution time across all circuit executions, $T_{\text{total}} = \sum_m N_m t_m = \mathcal{O}(\epsilon^{-1})$ [47]. Here, N_m denotes the number of samples for the m -th round of the Hadamard test measurement.

Crucially for our purposes, when the initial state has a high fidelity to the ground state, i.e., $\eta = 1 - \omega$ with $\omega \ll 1$, RPE admits a trade-off between maximal and total evolution times parameterized by $\xi = \mathcal{O}(\omega)$ as follows [47]:

$$T_{\max} = \mathcal{O}\left(\frac{\xi}{\epsilon}\right), \quad T_{\text{total}} = \mathcal{O}\left(\frac{1}{\xi\epsilon}\right). \quad (4)$$

Therefore, decreasing ξ (enabled by a higher-fidelity initial state) reduces the maximum required evolution time at the cost of increasing the total evolution time. In our

early-FTQC setting, T_{\max} is directly related to the maximum circuit depth per shot, while T_{total} controls the total number of gate layers accumulated across all shots. This parameter ξ thus acts as a tunable knob that determines the trade-off between per-shot circuit depth and overall sampling overhead. The precise theoretical guarantees and algorithmic procedure we use are provided in Appendix A.

B. Partially randomized time evolution

The RPE framework described above assumes access to the exact time evolution unitary $e^{-it\hat{H}}$. In practice, we approximate this unitary using product formulas. Following Ref. [41], we distinguish three approaches: (i) deterministic product formulas, (ii) fully randomized product formulas, and (iii) *partially randomized* product formulas that interpolate between these extremes.

1. Deterministic product formula

Deterministic product formulas, often called Trotterization [65, 66], approximate the time-evolution unitary for a small timestep δ as

$$e^{-i\delta\hat{H}} \approx \hat{S}_p(\delta), \quad (5)$$

where $\hat{S}_p(\delta)$ is a p -th-order Suzuki-Trotter formula constructed from exponentials of the individual terms $\hat{H}_\ell := c_\ell \hat{P}_\ell$. For instance, the second-order Suzuki-Trotter product formula is

$$\hat{S}_2(\delta) = \prod_{\ell=1}^L e^{-i\frac{\delta}{2}\hat{H}_\ell} \prod_{\ell=L}^1 e^{-i\frac{\delta}{2}\hat{H}_\ell}, \quad (6)$$

where the terms in the first product are ordered from $\ell = 1$ to L , and in the reverse order for the second product. To simulate the evolution for a total time t , this formula is applied r times with a step size of $\delta = t/r$:

$$e^{-it\hat{H}} = (e^{-i\delta\hat{H}})^r \approx \hat{S}_p(\delta)^r. \quad (7)$$

The resulting simulation error can be characterized either by its operator norm or, more relevantly for QPE, by the induced bias in the ground-state energy [20, 41, 67]:

$$|E_0 - E_{\text{eff},0}| \leq C_{\text{gs}} \delta^p. \quad (8)$$

Here, $E_{\text{eff},0}$ is the ground-state energy of an effective Hamiltonian \hat{H}_{eff} defined by $\hat{S}_p(\delta) = e^{-i\delta\hat{H}_{\text{eff}}}$, and $C_{\text{gs}} = C_{\text{gs}}(p, \{\hat{H}_\ell\})$ is a Trotter constant that depends on the order p and the chosen permutation of the terms $\{\hat{H}_\ell\}$. While rigorous operator-norm bounds [68] suggest $C_{\text{gs}} = \mathcal{O}(\lambda^{p+1})$, it is well known that such worst-case bounds significantly overestimate the actual Trotter error in many practical scenarios [69–71]. To avoid such

overestimation, our resource estimates in Secs. IV and V utilize empirical values for the Trotter error constant C_{gs} reported in Ref. [41] (see Appendix B for details).

To estimate the ground-state energy E_0 with precision ϵ , the Trotter-induced energy bias in Eq. (8) must be suppressed to $\mathcal{O}(\epsilon)$, which requires a step size $\delta = \mathcal{O}((\epsilon/C_{\text{gs}})^{1/p})$. The cost per Trotter step is $\mathcal{O}(L)$ gates for a Hamiltonian with L terms. Combining these factors with the RPE time requirements from Eq. (4), the maximum gate count per shot (determined by T_{\max}) and the total gate count across all shots (determined by T_{total}) can be estimated. Specifically, the maximum gate count per shot is $\mathcal{O}(L \cdot T_{\max}/\delta) = \mathcal{O}(L\xi C_{\text{gs}}^{1/p} \epsilon^{-1-1/p})$, and the total gate count is $\mathcal{O}(L \cdot T_{\text{total}}/\delta) = \mathcal{O}(L\xi^{-1} C_{\text{gs}}^{1/p} \epsilon^{-1-1/p})$.

2. Randomized product formula

Randomized product formulas [72–77], such as the quantum stochastic drift (qDRIFT) protocol [72], randomized Taylor expansion (RTE) [74], and time-evolution by probabilistic angle interpolation (TEPAI) [77], simulate Hamiltonian evolution by stochastically sampling Hamiltonian terms $\{\hat{H}_\ell\}$ according to a probability distribution derived from their weights $\{|c_\ell|\}$. This approach leads to gate counts that scale with the total weight λ given in Eq. (2), rather than the number of terms L .

Specifically, the Hamiltonian is rewritten to define a probability distribution $\{b_\ell\}$:

$$\hat{H} = \lambda \sum_{\ell=1}^L b_\ell \hat{P}'_\ell, \quad b_\ell = \frac{|c_\ell|}{\lambda}, \quad (9)$$

where the sign of each coefficient c_ℓ is absorbed into the corresponding Pauli string, $\hat{P}'_\ell \rightarrow \text{sgn}(c_\ell) \hat{P}_\ell$. The qDRIFT protocol approximates the time evolution $e^{-it\hat{H}}$ by composing r stochastic steps. For a total time t , this corresponds to simulating the rescaled evolution $(e^{-i\tau(\hat{H}/\lambda)})^r$, where $\tau = \lambda t/r$ is an effective timestep. The key idea is to implement a unitary \hat{U}_ℓ in each step, sampled with probability b_ℓ , such that the expectation value over the sampling correctly reproduces the target short-time evolution. That is, we require

$$\mathbb{E}[\hat{U}_\ell] = \sum_{\ell=1}^L b_\ell \hat{U}_\ell \approx e^{-i\tau(\hat{H}/\lambda)}. \quad (10)$$

A common choice is $\hat{U}_\ell = e^{i\phi\hat{P}'_\ell}$, where ϕ is a fixed rotation angle [72]. The expectation value then becomes

$$\begin{aligned} \sum_{\ell=1}^L b_\ell e^{i\phi\hat{P}'_\ell} &= \sum_{\ell=1}^L b_\ell (\cos \phi \hat{I} + i \sin \phi \hat{P}'_\ell) \\ &= \cos \phi \hat{I} + i \sin \phi (\hat{H}/\lambda), \end{aligned} \quad (11)$$

where \hat{I} is the identity operator. By comparing this with the Taylor expansion $e^{-i\tau(\hat{H}/\lambda)} = I - i\tau(\hat{H}/\lambda) + \mathcal{O}(\tau^2)$, we see that the two expressions become proportional if we set $\phi = -\arctan(\tau)$ [41, 72, 74]. The full evolution is then approximated by applying a sequence of r randomly selected unitaries. Specifically, for a sequence of random indices $\vec{\ell} = (\ell_1, \dots, \ell_r)$ sampled with the probability $q_{\vec{\ell}} = b_{\ell_1} \cdots b_{\ell_r}$, the corresponding unitary is $\hat{W}_{\vec{\ell}} = e^{i\phi\hat{P}'_{\ell_1}} \cdots e^{i\phi\hat{P}'_{\ell_r}}$.

When this stochastic evolution is used in the Hadamard test, the expectation value of the measurement outcome $\bar{Z}_r(t)$ is given by

$$\bar{g}_r(t) := \mathbb{E}[\bar{Z}_r(t)] = \sum_{\vec{\ell}} q_{\vec{\ell}} \langle \psi | \hat{W}_{\vec{\ell}} | \psi \rangle. \quad (12)$$

As shown in Ref. [41], this expression evaluates to

$$\begin{aligned} \bar{g}_r(t) &= (1 + \tau^2)^{-r/2} \langle \psi | \left(\hat{I} - i\tau(\hat{H}/\lambda) \right)^r | \psi \rangle \\ &= (1 + \tau^2)^{-r/2} \sum_k p_k (1 - i\tau(E_k/\lambda))^r \\ &\approx \sum_k p_k e^{-\frac{1}{2}r\tau^2(1 - (E_k/\lambda)^2)} e^{-itE_k}, \end{aligned} \quad (13)$$

where the approximation holds for small τ (and thus small ϕ). The resulting signal $\bar{g}_r(t)$ is similar to the exact signal $g(t)$ in Eq. (3), but is suppressed by an eigenvalue-dependent damping factor. To prevent the sampling overhead from increasing exponentially with time, this damping must be kept constant, i.e., $\tau^2 r = \mathcal{O}(1)$. This condition implies that the number of required Pauli rotations is $r = \mathcal{O}(\lambda^2 t^2)$, with each rotation having a fixed angle of $\phi \approx -\tau = \mathcal{O}((\lambda t)^{-1})$.

Other randomized methods, such as RTE [74] and TE-PAI [77], also exhibit quadratic scaling in cost with λt . Their primary advantage over qDRIFT is that the resulting signal $\bar{g}_r(t)$ is unbiased, and has a damping factor that is independent of the eigenvalues E_k , i.e., $\bar{g}_r(t) \approx B(t)^{-1} g(t)$ [41, 77]. The sampling overhead $B(t)^2$ can be suppressed to $\mathcal{O}(1)$ by choosing $r = \mathcal{O}(\lambda^2 t^2)$, leading to the same overall cost scaling with qDRIFT.

While randomized product formulas remove the explicit dependence on $L = \mathcal{O}(N^4)$ seen in Trotterization, their cost scales quadratically with the simulation time t . This leads to an unfavorable scaling for QPE. Specifically, applying the results of Ref. [41], RPE based on randomized product formulas results in a maximum gate count per shot of $\mathcal{O}(\lambda^2 \xi^2 \epsilon^{-2})$ and a total gate count of $\mathcal{O}(\lambda^2 \epsilon^{-2})$.

3. Partially randomized product formula

Partially randomized product formulas [37–41] are designed to exploit the empirical structure of electronic structure Hamiltonians. In these Hamiltonians, a relatively small number of terms with large coefficients typically dominate the total weight λ , while the remaining

terms form a long tail of smaller contributions (see Fig. 2 for an example). The core idea is to treat the dominant, large-weight terms deterministically using Trotterization, while stochastically sampling the numerous small-weight terms. This approach aims to combine the favorable scaling of deterministic methods with respect to evolution time and the insensitivity of randomized methods to the number of terms L . The analysis in Ref. [41] shows that, when combined with RPE, this hybrid scheme can yield significantly improved performance compared to both purely deterministic and fully randomized approaches, especially for molecular Hamiltonians with highly inhomogeneous coefficient distributions.

The partially randomized simulation framework begins by partitioning the Hamiltonian (1) into a deterministic part \hat{H}_D and a randomized part \hat{H}_R :

$$\hat{H} = \underbrace{\sum_{\ell=1}^{L_D} \hat{H}_\ell}_{=: \hat{H}_D} + \underbrace{\sum_{\ell=L_D+1}^L \hat{H}_\ell}_{=: \hat{H}_R}, \quad (14)$$

where the terms $\hat{H}_\ell (= c_\ell \hat{P}_\ell)$ are assumed to be sorted in descending order of their coefficient magnitudes, $|c_1| \geq |c_2| \geq \cdots \geq |c_L|$. Here, \hat{H}_D comprises the L_D terms with the largest weights, while \hat{H}_R contains the remaining small-weight terms.

The evolution is then approximated using a Trotter formula applied to this partitioned Hamiltonian. For example, using a second-order formula, a target time evolution $e^{-it\hat{H}}$ is approximated as

$$e^{-it\hat{H}} \approx \hat{S}_2(\delta)^r = \left(\prod_{\ell=1}^{L_D} e^{-i\frac{\delta}{2}\hat{H}_\ell} e^{-i\delta\hat{H}_R} \prod_{\ell=L_D+1}^L e^{-i\frac{\delta}{2}\hat{H}_\ell} \right)^r, \quad (15)$$

where $\delta = t/r$. In this scheme, the evolution $e^{-i\delta\hat{H}_R}$ corresponding to the randomized part is implemented stochastically, as described in Sec. II B 2. This introduces a stochastic element into the simulation. As with the fully randomized method, performing a Hadamard test yields a signal that reproduces the desired expectation value $\langle \psi | \hat{S}_2(\delta)^r | \psi \rangle$, but with a damping factor that introduces additional sampling overhead. This overhead can be suppressed to $\mathcal{O}(1)$ by choosing the number of steps to scale as $r = \mathcal{O}(\lambda_R^2 \delta^2)$ [41], where λ_R is the total weight of the randomized part:

$$\lambda_R := \sum_{\ell=L_D+1}^L |c_\ell|. \quad (16)$$

The overall Trotter error from the deterministic part imposes an additional constraint on the step size δ . Combining these considerations, the total cost inherits features from both methods.

The overall simulation costs for partially randomized RPE are a hybrid of the deterministic and randomized

costs. As derived in Ref. [41], the maximum number of Pauli rotations per shot and the total number of rotations across all shots are given by

$$\begin{aligned} \text{Max per-shot cost: } & \mathcal{O}(L_D \xi C_{\text{gs}}^{1/p} \epsilon^{-1-1/p} + \lambda_R^2 \xi^2 \epsilon^{-2}), \\ \text{Total cost: } & \mathcal{O}(L_D \xi^{-1} C_{\text{gs}}^{1/p} \epsilon^{-1-1/p} + \lambda_R^2 \epsilon^{-2}). \end{aligned}$$

These expressions clearly show that partial randomization is effective when a partition exists such that both $L_D \ll L$ and $\lambda_R \ll \lambda$. For comparison, the simulation costs for the three approaches are summarized in Table I.

4. Algorithmic cost model for partially randomized robust phase estimation

In the remainder of this work, we shift our focus from the asymptotic precision guarantees of RPE to the concrete circuit cost of implementing the time-evolution unitaries that appear in each shot. Following Ref. [41], we formulate this cost at the level of the logical circuit, in terms of the number of elementary gate applications required by the partially randomized RPE scheme.

The optimal partitioning of the Hamiltonian into deterministic and randomized parts (Eq. (14)) is found by minimizing the simulation cost of the resulting circuit. For partially randomized RPE, the gate cost for a single RPE iteration at time $t_m = 2^m$ is given by

$$\begin{aligned} G_m &= \min_{L_D} \left[g_m^{(\text{det})} L_D + g_m^{(\text{rand})} \lambda_R^2 \right] \\ &= \min_{L_D} \left[g_m^{(\text{det})} L_D + g_m^{(\text{rand})} \left(\sum_{\ell=L_D+1}^L |c_\ell| \right)^2 \right]. \end{aligned} \quad (17)$$

The factors $g_m^{(\text{det})}$ and $g_m^{(\text{rand})}$ encapsulate algorithm-specific details and are provided in Appendix B. The gate cost G_m quantifies the number of elementary gates that are considered the primary bottleneck for a given quantum computing architecture. For the early fault-tolerant setting discussed in Sec. V, this bottleneck is the implementation of non-Clifford Pauli rotation gates. In this context, G_m represents the number of non-Clifford gates required to implement the evolution for time t_m .

Since RPE evaluates the Hadamard test at a sequence of evolution times $\{t_m\}$, the total logical gate cost of the entire procedure is the sum over all iterations:

$$G_{\text{total}} = \sum_{m=0}^M e N_m G_m, \quad (18)$$

where N_m is the number of shots required for the time step t_m , and $e \simeq 2.72$ is a constant overhead factor inherent to the randomized protocol. As detailed in Appendix B, the overall cost G_{total} is heavily dominated by the contribution from the final iteration ($m = M$) and can be approximated as $G_{\text{total}} \simeq e N_M G_M$.

In Sec. III, we will consider the total gate cost G_{total} as a function of the Hamiltonian representation—specifically, of the Pauli coefficient distribution $\{c_\ell\}$. The UWC method introduced there is formulated as an optimization problem that seeks to find Hamiltonian representations that minimize this total cost, subject to preserving the energy spectrum of the underlying electronic structure Hamiltonian.

III. HAMILTONIAN REPRESENTATION AND OPTIMIZATION

As described in Sec. II, the partially randomized time evolution leads to an algorithmic simulation cost that depends on the structure of its coefficient distribution $\{c_\ell\}$ and on the number of large-weight terms promoted into the deterministic segment of the time evolution. In this setting, different representations of the same Hamiltonian can lead to distinct values of the total simulation cost, even when their spectra are identical.

Motivated by this observation, we do not restrict ourselves to a single representation of \hat{H} , but instead treat the Hamiltonian representation itself as an optimization degree of freedom. In particular, we consider Hamiltonian transformations that preserve the eigenvalue spectrum within a relevant symmetry sector, while allowing the coefficient distribution to be reshaped. We refer to the resulting optimization problem as UWC. This nomenclature reflects the conceptual goal of promoting concentrated Pauli coefficient distributions, which are characterized by a small number of dominant terms that significantly contribute to the total weight.

A. Electronic structure Hamiltonian

We consider active-space electronic structure Hamiltonians for molecules in the second-quantized form:

$$\begin{aligned} \hat{H} &= \sum_{pq} \sum_{\sigma=\uparrow,\downarrow} h_{pq} \hat{a}_{p\sigma}^\dagger \hat{a}_{q\sigma} + \frac{1}{2} \sum_{pqrs} \sum_{\sigma\tau} g_{pqrs} \hat{a}_{p\sigma}^\dagger \hat{a}_{r\tau}^\dagger \hat{a}_{s\tau} \hat{a}_{q\sigma} \\ &=: \sum_{pq} k_{pq} \hat{F}_{pq} + \frac{1}{2} \sum_{pqrs} g_{pqrs} \hat{F}_{pq} \hat{F}_{rs}, \end{aligned} \quad (19)$$

where $\hat{a}_{p\sigma}$ and $\hat{a}_{p\sigma}^\dagger$ are fermionic annihilation and creation operators for a p -th orbital electron with spin σ , N is the number of spatial orbitals in the active space, and h_{pq} and g_{pqrs} are the corresponding one- and two-electron integrals. For convenience, we have introduced $\hat{F}_{pq} := \sum_{\sigma} \hat{a}_{p\sigma}^\dagger \hat{a}_{q\sigma}$ and $k_{pq} := h_{pq} - \frac{1}{2} \sum_r g_{prrq}$ in Eq. (19).

After a fermion-to-qubit mapping, such as the Jordan-Wigner transformation, \hat{H} takes the Pauli LCU form of Eq. (1). For the electronic structure Hamiltonian, this Pauli LCU representation can be written as a sum of

TABLE I. Comparison of asymptotic simulation costs for the RPE algorithm using different time-evolution methods: deterministic (p -th order Suzuki-Trotter), fully randomized, and partially randomized product formulas, according to Ref. [41]. The costs are expressed in terms of Pauli rotations per shot and total Pauli rotations across all shots, indicating their dependencies on Hamiltonian parameters (L , L_D , λ , λ_R , C_{gs}), RPE parameters (ξ , ϵ), and Trotter order (p).

Method	Maximum per-shot simulation cost	Total simulation cost
Deterministic (p -th order Suzuki-Trotter)	$\mathcal{O}(L\xi C_{\text{gs}}^{1/p} \epsilon^{-1-1/p})$	$\mathcal{O}(L\xi^{-1} C_{\text{gs}}^{1/p} \epsilon^{-1-1/p})$
Randomized	$\mathcal{O}(\lambda^2 \xi^2 \epsilon^{-2})$	$\mathcal{O}(\lambda^2 \epsilon^{-2})$
Partially randomized	$\mathcal{O}(L_D \xi C_{\text{gs}}^{1/p} \epsilon^{-1-1/p} + \lambda_R^2 \xi^2 \epsilon^{-2})$	$\mathcal{O}(L_D \xi^{-1} C_{\text{gs}}^{1/p} \epsilon^{-1-1/p} + \lambda_R^2 \epsilon^{-2})$

products of Majorana operators [33]:

$$\begin{aligned} \hat{H} = & \frac{i}{2} \sum_{pq,\sigma} \left(k_{pq} + \sum_r g_{pqrr} \right) \hat{\gamma}_{p\sigma} \hat{\gamma}_{q\sigma} \\ & + \frac{1}{4} \sum_{p>r,s>q} \sum_{\sigma} (g_{pqrs} - g_{psrq}) \hat{\gamma}_{p\sigma} \hat{\gamma}_{r\sigma} \hat{\gamma}_{q\sigma} \hat{\gamma}_{s\sigma} \\ & + \frac{1}{4} \sum_{pqrs} g_{pqrs} \hat{\gamma}_{p\uparrow} \hat{\gamma}_{r\downarrow} \hat{\gamma}_{q\uparrow} \hat{\gamma}_{s\downarrow} + \text{const.}, \end{aligned} \quad (20)$$

where the Majorana operators are defined as

$$\hat{\gamma}_{p\sigma} = \hat{a}_{p\sigma} + \hat{a}_{p\sigma}^\dagger, \quad \hat{\gamma}_{p\sigma} = -i(\hat{a}_{p\sigma} - \hat{a}_{p\sigma}^\dagger). \quad (21)$$

Each product of Majorana operators in Eq. (20) corresponds to one of the Pauli strings $\{P_\ell\}$ in the Pauli LCU representation (1). Although the explicit form of the Pauli string depends on the chosen fermion-to-qubit mapping, the Pauli coefficient distribution $\{c_\ell\}$ is solely determined by the electron integrals h_{pq} and g_{pqrs} , as expressed in Eq. (20), irrespective of the choice of the fermion-to-qubit mapping.

B. Spectrally-invariant Hamiltonian transformations

Before introducing UWC, we define a structured family of Hamiltonian transformations that will serve as its foundation. We refer to these transformations as *spectrally-invariant* transformations, as they preserve the eigenvalue spectrum within a specified target symmetry sector while modifying the Hamiltonian representation. In this work, this family is characterized by the following two complementary layers.

1. Orbital optimization

The first layer is an OO transformation [33, 34], which consists of a unitary rotation in the one-particle basis before fermion-to-qubit mapping. This unitary transformation preserves the entire eigenvalue spectrum of \hat{H} , while altering the Pauli coefficient distribution $\{c_\ell\}$. OO is realized through the rotation of molecular orbital bases

as

$$\hat{a}'_{i\sigma} = \sum_p^N (U_{\text{oo}})_{ip} \hat{a}_{p\sigma}, \quad (22)$$

where $U_{\text{oo}} := e^{-K}$ is an orbital rotation unitary, and K is a skew-symmetric matrix (i.e., $K^T = -K$) defined as

$$K := \begin{pmatrix} 0 & \kappa_{12} & \kappa_{13} & \cdots & \kappa_{1N} \\ -\kappa_{12} & 0 & \kappa_{23} & \cdots & \kappa_{2N} \\ -\kappa_{13} & -\kappa_{23} & 0 & \cdots & \kappa_{3N} \\ \vdots & \vdots & \vdots & \ddots & \vdots \\ -\kappa_{1N} & -\kappa_{2N} & -\kappa_{3N} & \cdots & 0 \end{pmatrix}. \quad (23)$$

For real-valued molecular orbitals, the parameters κ_{ij} can be assumed real without loss of generality, leading to $N(N-1)/2$ controllable parameters in total. Denoting these parameters as $\vec{\kappa} = \{\kappa_{ij} \mid i < j\}$, the OO-transformed Hamiltonian is written as

$$\begin{aligned} \hat{H}'(\vec{\kappa}) & := \hat{U}_{\text{oo}}^T(\vec{\kappa}) \hat{H} \hat{U}_{\text{oo}}(\vec{\kappa}) \\ & = \sum_{pq}^N k'_{pq}(\vec{\kappa}) \hat{F}_{pq} + \frac{1}{2} \sum_{pqrs}^N g'_{pqrs}(\vec{\kappa}) \hat{F}_{pq} \hat{F}_{rs}, \end{aligned} \quad (24)$$

where $\mathcal{U}_{\text{oo}} := U_{\text{oo}} \otimes U_{\text{oo}}$ and

$$h'_{pq}(\vec{\kappa}) = \sum_{ij}^N [e^{-K}]_{ip} h_{ij} [e^{-K}]_{jq}, \quad (25)$$

$$g'_{pqrs}(\vec{\kappa}) = \sum_{ijkl}^N [e^{-K}]_{ip} [e^{-K}]_{jq} g_{ijkl} [e^{-K}]_{kr} [e^{-K}]_{ls}, \quad (26)$$

with $k'_{pq}(\vec{\kappa}) := h'_{pq}(\vec{\kappa}) - \frac{1}{2} \sum_r g'_{prrq}(\vec{\kappa})$. In practice, the success of OO is sensitive to the choice of the initial orbitals [33, 34]. In this work, among the initial orbitals (specifically, those provided in the literature and those rotated along Cholesky vectors [41]), the one with the smallest ℓ_1 -norm is selected as the initial orbital for OO (see Appendix D for details).

2. Block-invariant symmetry shift

The second layer is a BLISS transformation [35, 36], which applies block-diagonal shift transformations within

fixed symmetry sectors of the Hamiltonian (e.g., particle number, spin, and relevant point-group irreducible representations). BLISS preserves the spectrum within a specific target block, while possibly changing the spectra of other blocks. The definition of the BLISS transformation depends on the target symmetry sector and corresponding symmetry operation.

For instance, when we wish to preserve the eigenvalue spectrum in a fixed particle-number sector with N_e electrons, the corresponding BLISS operator is defined as [35, 36]

$$\hat{T}(\vec{\mu}, \vec{\xi}) := \mu_1(\hat{N}_e - N_e) + \mu_2(\hat{N}_e^2 - N_e^2) + \sum_{pq}^N \xi_{pq} \hat{F}_{pq} (\hat{N}_e - N_e), \quad (27)$$

where $\mu_1, \mu_2, \xi_{pq} \in \mathbb{R}$ with $\xi_{pq} = \xi_{qp}$, and $\hat{N}_e := \sum_{p,\sigma} \hat{a}_{p\sigma}^\dagger \hat{a}_{p\sigma}$ is the particle number operator. The parameters are denoted as $\vec{\mu} := \{\mu_1, \mu_2\}$ and $\vec{\xi} := \{\xi_{pq} \mid p \leq q\}$, leading to $2 + N(N+1)/2$ independent parameters for optimization. The Hamiltonian \hat{H} is transformed as

$$\begin{aligned} \hat{H}'(\vec{\mu}, \vec{\xi}) &:= \hat{H} - \hat{T}(\vec{\mu}, \vec{\xi}) \\ &= \sum_{pq}^N k'_{pq}(\vec{\mu}, \vec{\xi}) \hat{F}_{pq} + \frac{1}{2} \sum_{pqrs}^N g'_{pqrs}(\vec{\mu}, \vec{\xi}) \hat{F}_{pq} \hat{F}_{rs} \\ &\quad + \mu_1 N_e + \mu_2 N_e^2, \end{aligned} \quad (28)$$

where

$$h'_{pq}(\vec{\mu}, \vec{\xi}) = h_{pq} - (\mu_1 + \mu_2) \delta_{pq} + (N_e - 1) \xi_{pq}, \quad (29)$$

$$g'_{pqrs}(\vec{\mu}, \vec{\xi}) = g_{pqrs} - 2\mu_2 \delta_{pq} \delta_{rs} - (\xi_{pq} \delta_{rs} + \delta_{pq} \xi_{rs}), \quad (30)$$

with $k'_{pq}(\vec{\mu}, \vec{\xi}) := h'_{pq}(\vec{\mu}, \vec{\xi}) - \frac{1}{2} \sum_r g'_{prrq}(\vec{\mu}, \vec{\xi})$. Since $\hat{T}(\vec{\mu}, \vec{\xi}) |\psi\rangle = 0$ for any N_e -electron state $|\psi\rangle$ by definition, the BLISS transformation in Eq. (28) preserves the eigenvalue spectrum in the target N_e -electron particle-number sector. The BLISS operator $\hat{T}(\vec{\mu}, \vec{\xi})$ is Hermitian and has the same fermionic polynomial degrees as \hat{H} . These properties are desired constraints for BLISS, as they simplify analysis and optimization [35]. In this work, BLISS operations are also employed for spin symmetry, as detailed in Appendix C.

C. Unitary weight concentration

Here, we describe our Hamiltonian optimization strategy based on spectrally invariant transformations to minimize the gate cost of partially randomized QPE.

Let $\mathcal{F}(\hat{H})$ denote a set of spectrally-invariant transformations applicable to the original Hamiltonian \hat{H} , such as OO and BLISS. We then express a possible Hamiltonian representation under spectrally-invariant transformations as

$$\hat{H}'(\vec{\chi}) = f_{\vec{\chi}}(\hat{H}), \quad f_{\vec{\chi}} \in \mathcal{F}(\hat{H}) \quad (31)$$

where $\vec{\chi}$ is a set of parameters characterizing the Hamiltonian transformation $f_{\vec{\chi}}$. In this work, the $f_{\vec{\chi}}$ consists of the OO and BLISS transformations. These OO and BLISS transformations alter only the coefficient distribution $\{c_\ell\}$, without introducing Majorana polynomials not included in the original Hamiltonian (20), and preserve the Pauli string set $\{P_\ell\}$. The Pauli LCU representation for the transformed Hamiltonian $\hat{H}'(\vec{\chi})$ is then given by

$$\hat{H}'(\vec{\chi}) = \sum_{\ell} c'_\ell(\vec{\chi}) \hat{P}_\ell. \quad (32)$$

The transformed coefficients $\{c'_\ell(\vec{\chi})\}$ are determined by the transformed electron integrals $h'_{pq}(\vec{\chi})$ and $g'_{pqrs}(\vec{\chi})$, as expressed in Eq. (20), and therefore $c'_\ell(\vec{\chi})$ is a functional of these transformed integrals, i.e., $c'_\ell(\vec{\chi}) := c'_\ell[\{h'_{pq}(\vec{\chi}), g'_{pqrs}(\vec{\chi})\}]$. With this transformed coefficient distribution $\{c'_\ell(\vec{\chi})\}$, we evaluate the total algorithmic cost G_{total} (Eq. (18)), which was introduced in Sec. II B 4.

In this setup, our goal is to solve the following optimization problem:

$$\vec{\chi}^* = \arg \min_{\vec{\chi}} G_{\text{total}}(\hat{H}'(\vec{\chi})), \quad (33)$$

where we denote G_{total} as a function of the Hamiltonian representation $\hat{H}'(\vec{\chi})$. As described in Sec. II B 4, the total simulation cost G_{total} is dominated by the contribution from the last round $m = M$. Thus, the optimization problem (33) can be approximated as

$$\vec{\chi}^* \approx \arg \min_{\vec{\chi}} G_M(\hat{H}'(\vec{\chi})). \quad (34)$$

We note that, in principle, one could perform a round-dependent optimization and determine a distinct Hamiltonian representation for each m . However, this would increase the classical optimization overhead by roughly a factor of M . Since the total computational cost of RPE is dominated by the final round ($m = M$), with earlier rounds contributing only marginally, optimizing G_M alone captures the dominant effect on resource reduction.

However, solving this optimization problem is notably challenging due to two primary factors. First, estimating the objective function G_M for a given Hamiltonian representation $\hat{H}'(\vec{\chi})$ is itself an optimization problem with respect to the deterministic/randomized partitioning point L_D , as described in Eq. (17). This bilevel optimization structure significantly increases computational cost, rendering exact solutions for the problem (34) computationally intractable in practice. Second, the embedded sorting operation for $\{c'_\ell(\vec{\chi})\}$, which is necessary to determine the optimal deterministic/randomized partitioning, introduces severe non-differentiability, non-smoothness, and combinatorial complexity, thus precluding the use of traditional gradient-based optimization methods.

To circumvent such difficulties, the UWC method instead aims to solve the following softened optimization problem:

$$\bar{\chi}^* = \arg \min_{\bar{\chi}} G_{\text{soft}}(\hat{H}'(\bar{\chi})),$$

$$\text{for } G_{\text{soft}}(\hat{H}'(\bar{\chi})) := g_M^{(\text{det})} \sum_{\ell=1}^L \varsigma \left(\frac{|c'_\ell(\bar{\chi})| - w_{\text{soft}}}{\epsilon_{\text{soft}}} \right) + g_M^{(\text{rand})} \left(\sum_{\ell=1}^L |c'_\ell(\bar{\chi})| \left[1 - \varsigma \left(\frac{|c'_\ell(\bar{\chi})| - w_{\text{soft}}}{\epsilon_{\text{soft}}} \right) \right] \right)^2, \quad (35)$$

where $\varsigma(x) := 1/(1+\exp(-x))$ is the sigmoid function and $\epsilon_{\text{soft}} > 0$ is a constant used for the sigmoid regularization. Here, w_{soft} is defined as the mean coefficient weight at the optimal deterministic/randomized partitioning point for the initial Hamiltonian \hat{H} :

$$w_{\text{soft}} := \frac{|c_{L_D}^*| + |c_{L_D+1}^*|}{2}, \quad (36)$$

$$L_D^* := \arg \min_{L_D} \left[g_M^{(\text{det})} L_D + g_M^{(\text{rand})} \lambda_R^2 \right]. \quad (37)$$

In Eq. (35), the bilevel structure of the original problem (34) is simplified by incorporating information about the deterministic/randomized partitioning solely from the initial coefficient distribution $\{c_\ell\}$ as the hyperparameter w_{soft} . Furthermore, discontinuous behaviors arising from the sorting operations are mitigated by introducing a sigmoid regularization with a smoothness hyperparameter ϵ_{soft} : the objective function G_{soft} approaches the original cost function G_M as $\epsilon_{\text{soft}} \rightarrow 0$. In practice, UWC is performed as an iterative optimization of combined OO and BLISS transformations, adjusting the hyperparameter w_{soft} at each iteration. Iterations are terminated when the relative improvement in the cost function G_{soft} falls below a prescribed threshold. A detailed description of the numerical optimization procedure is given in Appendix D.

It is worth noting that both OO and BLISS were originally proposed for minimizing the ℓ_1 -norm λ [33, 35]. Optimizing the ℓ_1 -norm generally leads to a sparse coefficient distribution and is also effective in reducing the partially randomized simulation cost [41]. However, as demonstrated in Appendix D 3, UWC generally exhibits better performance for reducing the partially randomized simulation cost compared to ℓ_1 -norm optimization, even though both methods utilize the same OO and BLISS transformations.

IV. NUMERICAL VALIDATION AND BENCHMARK RESULTS OF UWC

In this section, we present numerical results validating the effectiveness of UWC and quantify its impact on the cost of partially randomized QPE for chemically relevant molecular models. First, using a representative molecular instance, we demonstrate how UWC reshapes the coefficient distribution of Pauli-LCU Hamiltonians and alters the balance between deterministic and randomized segments. Subsequently, we assess the practical

consequences of this reshaping by quantifying gate-count reductions across representative molecular active-space models.

A. Representative molecular models

To assess the practical impact of UWC under early-FTQC constraints, we consider a set of molecular active-space models drawn from three chemically and industrially relevant families: iron-sulfur clusters [19, 34, 50], cytochrome P450 active-site models [51], and ruthenium-based catalysts for transforming CO₂ to high-value chemical methanol [22]. All molecular Hamiltonians and active-space definitions used in this work were adopted from established prior studies [22, 34, 51], and were not constructed specifically for the present analysis. Consequently, the benchmark set comprises chemically motivated and well-studied electronic-structure models that have been extensively analyzed in the quantum computing for chemistry literature.

For each molecular family, we select representative active-space models spanning approximately 20 to 40 spatial orbitals. The information for each active-space model is summarized in Table II. These active spaces, while possessing Hilbert-space dimensions approaching or exceeding the practical limits of classical full-CI computation (typically $\sim 10^{12}$ [2, 3]), are nevertheless expected to be potentially accessible on early-FTQC hardware. The chosen models capture chemically relevant valence and near-valence orbitals that govern bonding, spin character, and catalytic reactivity, following active-space constructions proposed in the original references (see Appendix E 1 for details).

Across all benchmark systems, the electronic Hamiltonians are expressed in second-quantization form (Eq. (19)), and their corresponding Pauli-LCU representation is represented using the electron integrals h_{pq} and g_{pqrs} , as presented in Eq. (20). This uniform treatment enables a controlled comparison of deterministic, partially randomized, and UWC-optimized evolutions across different molecular families and active-space sizes.

Detailed information regarding the source references, active-space definitions, and symmetry sectors for each benchmark system is provided in Appendix E 1. In the following subsections, we use these models to examine how UWC reshapes Hamiltonian coefficient distributions and how this reshaping translates into reductions in the

TABLE II. Representative molecular models considered in the main text. They present models from chemically and industrially relevant areas, including bioinorganic clusters, enzymatically active sites, and homogeneous catalysts for CO₂ utilization. The active spaces are specified in terms of the number of correlated electrons and orbitals. The ‘‘Molecule ID’’ identifies the molecule species and active space size, as detailed in Appendix E 1.

Molecule ID	Orbitals	Electrons	Hilbert space dimension
(a) Iron-sulfur clusters [34]			
[2Fe-2S] ⁻³	20	31	7.51×10^7
[2Fe-2S] ⁻²	20	30	2.40×10^8
[4Fe-4S] ⁻²	36	54	8.86×10^{15}
[4Fe-4S]	36	52	6.46×10^{16}
(b) Cytochrome P450 [51]			
P450-Cpd I (D)	23	15	5.61×10^{11}
P450-Cpd I (E)	31	33	3.74×10^{16}
P450-Cpd I (F)	41	45	2.77×10^{22}
P450-Cpd I (G)	43	47	4.43×10^{23}
(c) Ruthenium-based catalysts for CO ₂ utilization [22]			
Ru-XVIII (Md)	20	28	1.50×10^9
Ru-IX (Md)	26	32	2.82×10^{13}
Ru-II-III (Md)	29	38	4.01×10^{14}
Ru-VIII (Md)	29	40	1.00×10^{14}

cost of partially randomized QPE.

B. Concentrated coefficient distribution and partially randomized simulation cost

We first examine how UWC reshapes the coefficient distribution for the Pauli-LCU representation of electronic structure Hamiltonians. To isolate this effect and provide a clear mechanistic picture, we focus on a single representative molecular active-space model of intermediate size from the benchmark set. Specifically, we choose a model of the compound I (Cpd I) in the P450 catalytic cycle, characterized by an intermediate-sized 31-orbital active space E [51] (see Appendix E 1 for chemical details of this active space).

Figure 2 compares the Pauli coefficient distribution before and after applying UWC. The computational details for obtaining the UWC-optimized Hamiltonian are summarized in Appendix D. Although the two Hamiltonian representations are spectrally equivalent within each symmetry sector, the UWC-optimized representation exhibits a markedly more concentrated coefficient distribution: a larger fraction of the total weight is carried by a smaller number of leading terms, while simultaneously, the weight of the small-weight tail terms is significantly suppressed. Such a concentrated weight profile is particularly relevant for the partially randomized QPE scheme, as explained in Sec. II B 4.

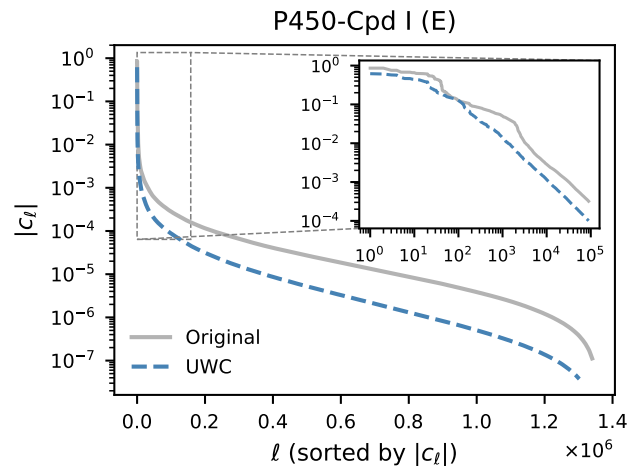


FIG. 2. Demonstration of Pauli coefficient concentration induced by UWC for the P450-Cpd I (E) model. The main panel shows the magnitudes of Pauli-LCU coefficients $\{|c_\ell|\}$, sorted in descending order, for the original (gray solid line) and UWC-optimized (blue dashed line) Hamiltonian representations. The inset presents a magnified view of the large-weight region.

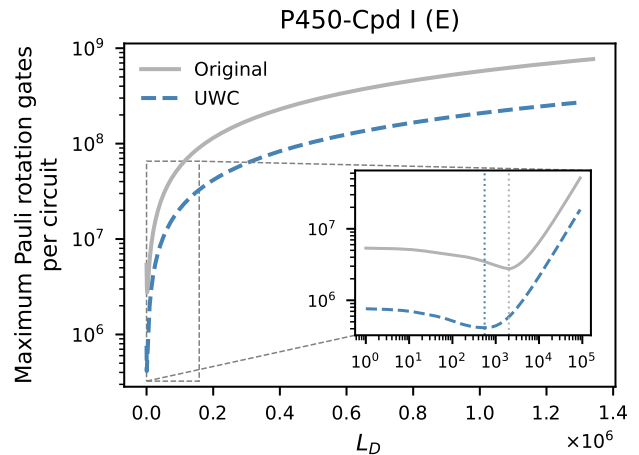


FIG. 3. Maximum per-shot Pauli-rotation gate count of partially randomized RPE with $\xi = 0.01$ as a function of the number of deterministic terms, L_D (up to a maximum of L), for the P450-Cpd I (E) model. Results are shown for the original (gray solid line) and UWC-optimized (blue dashed line) Hamiltonian representations. UWC lowers the overall cost and shifts the optimal deterministic partitioning to a smaller L_D , as shown in the inset, reflecting the more concentrated coefficient distribution in Fig. 2.

We next examine how this coefficient concentration induced by UWC translates into changes in the cost structure of partially randomized RPE. In the partially randomized framework, the Hamiltonian is partitioned into a deterministic segment, consisting of the L_D largest Pauli terms, and a randomized segment formed from the re-

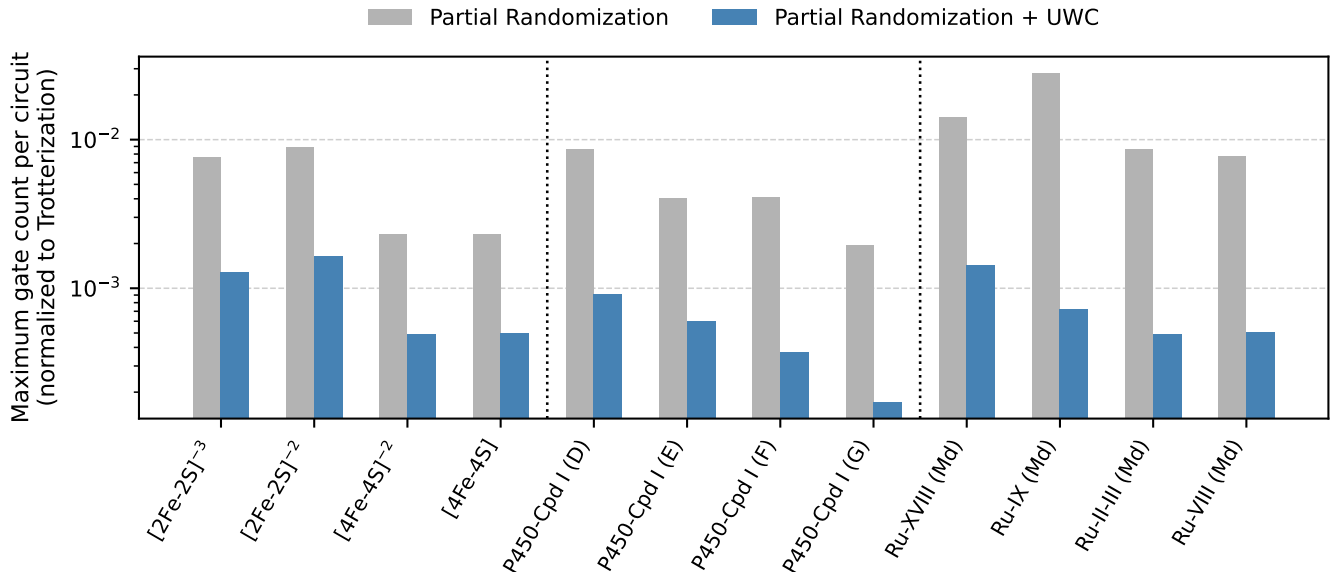


FIG. 4. Normalized maximum per-shot Pauli-rotation gate counts for representative molecular active-space models. Results are shown for partially randomized time evolution (gray bars) and for partially randomized time evolution combined with UWC (blue hatched bars), for the initial-state parameter $\xi = 0.01$. The values are normalized to the gate count for deterministic second-order Trotterization.

remaining terms. The total gate cost depends nontrivially on the choice of L_D , as described in Sec. II B 4, reflecting a trade-off between the cost of deterministic evolution and the variance contributed by the randomized tail. In all the following resource estimations for partially randomized RPE, we assume that the deterministic terms are handled by the second-order Suzuki-Trotter product formula, while the randomized part is implemented via the qDRIFT protocol, unless otherwise mentioned.

Figure 3 shows the maximum Pauli rotation gate count per circuit as a function of the number of deterministically treated terms, L_D , for the P450-Cpd I (E) model. Here, the initial state parameter ξ for RPE is fixed at $\xi = 0.01$, corresponding to $p_0 > 0.99$. For the original Hamiltonian representation, the cost curve exhibits a sharp minimum at relatively small $L_D (\ll L)$, indicating that the Pauli-LCU coefficient distribution of this molecular Hamiltonian is concentrated and partial randomization is effective in reducing the product-formula simulation cost [41]. When UWC is applied, the cost curve is uniformly lowered and its minimum shifts to smaller values of L_D . This shift directly reflects the enhanced dominance of the leading coefficients observed in Fig. 2: owing to a greater concentration of the total weight in fewer terms, a more efficient partially randomized treatment can be achieved with a smaller deterministic fragment.

Having established the mechanistic origin of coefficient concentration and its impact on the cost structure of partially randomized time evolution, we now assess the aggregate performance of UWC across the full benchmark

set of molecular active-space models. This analysis allows us to quantify how consistently the benefits observed in the representative example extend to chemically diverse systems and a range of active-space sizes.

Figure 4 summarizes normalized gate counts for the representative molecular models in Table II under partially randomized time evolution and UWC, with all values reported relative to deterministic second-order Trotterization. Across all models, partial randomization alone reduces the gate count to approximately 10^{-2} of the deterministic Trotter baseline, while the additional application of UWC further suppresses the cost to the 10^{-3} level. This additional reduction reflects the systematic enhancement of coefficient concentration induced by UWC, as demonstrated in Figs. 2 and 3. Although the absolute magnitude of the UWC-induced improvement varies across molecular instances, the qualitative trend is robust: UWC consistently provides an additional order-of-magnitude reduction beyond partial randomization alone.

Taken together, these results demonstrate that partially randomized time evolution delivers the dominant improvement over deterministic Trotterization, while UWC acts as a complementary optimization that further refines the Hamiltonian representation and yields substantial additional reductions in gate cost. In the following section, we incorporate these UWC-optimized Hamiltonians into end-to-end resource estimates to assess the feasibility of QPE on early-FTQC hardware.

V. RESOURCE ESTIMATION FOR EARLY FAULT-TOLERANT QUANTUM HARDWARE

Having established that partially randomized QPE combined with UWC can reduce algorithmic gate counts by up to three orders of magnitude relative to deterministic Trotterization, we now assess whether these improvements translate into practical feasibility on realistic quantum hardware. In this section, we present end-to-end resource estimates for executing the partially randomized RPE algorithm on early-FTQC hardware, focusing on devices with physical qubit budgets on the order of 10^5 .

A. Partially fault-tolerant quantum computing architecture based on STAR-magic mutation

We begin by outlining the early-FTQC framework used for resource estimation throughout this work. To translate algorithmic gate counts into physically meaningful resource estimates, we adopt a resource estimation framework based on an improved variant of the STAR architecture [29–31]. This improved variant is detailed in a separate work [52]. Here, we summarize only the features directly relevant to our resource estimation, and defer implementation details to Ref. [52].

The defining feature of the STAR architecture is its direct support for analog Pauli rotation gates $\hat{R}_P(\theta_L) := e^{i\theta_L \hat{P}}$, where \hat{P} is a Pauli string operator and $\theta_L \in \mathbb{R}$ is a logical rotation angle. Such analog rotation gates form the dominant cost component in Trotter-based quantum simulation and single-ancilla QPE. Rather than decomposing these rotation gates into long sequences of T -gates [78], which typically requires a costly magic-state distillation protocol [79–81], the STAR architecture enables their execution as native logical operations. This capability is particularly well-suited to early-FTQC regimes, where large-scale magic-state factories may be impractical due to the physical-qubit overhead.

Specifically, the STAR architecture implements analog rotation gates by preparing a special non-Clifford ancilla state $|m_{\theta_L}\rangle_L := e^{i\theta_L \hat{Z}_L} |+\rangle_L$ in a non-fault-tolerant manner, and then uses this state to perform a Pauli- Z rotation $\hat{R}_{z,L}(\theta_L) := e^{i\theta_L \hat{Z}_L}$ via gate teleportation [29]. This gate-teleportation protocol is stochastically implemented as a *repeat-until-success* (RUS) process: a failure event, occurring with a probability of $1/2$, is corrected by an inverse rotation, thereby doubling the logical rotation angle until teleportation succeeds. On average, this RUS process succeeds in two trials. The residual logical error arising from this RUS process is addressed using error mitigation techniques such as probabilistic error cancellation [82, 83]. In contrast, logical Clifford gates are implemented fault-tolerantly based on lattice surgery [84]. In this sense, the STAR architecture provides a means to achieve partial fault tolerance on limited-scale, near-term quantum hardware.

In the improved version of the STAR architecture considered throughout this work, logical analog rotations are executed using a protocol called *STAR-magic mutation* (SMM) [52]. SMM combines the STAR-based analog rotation protocol with *magic state cultivation* [85–87], a technique to prepare a clean magic state using only a single surface code patch. In the RUS process, failure events cause a sequential doubling of the rotation angle, leading to an increase from θ_L to $\theta_{\text{RUS}} (> \theta_L)$. In the SMM protocol, once the post-RUS angle θ_{RUS} exceeds a certain threshold θ_{th} , the target rotation gate $\hat{R}_P(\theta_{\text{RUS}})$ is decomposed into a sequence of T -gates, each executed using the magic state cultivation protocol. This significantly increases the efficiency of the RUS process and results in an effective logical error rate for analog rotation gates of $\mathcal{O}(\theta_L^{2(1-\Theta(1/d))} p_{\text{ph}})$ [52], where d is the code distance of the underlying surface code. This error scaling indicates that the SMM protocol is particularly beneficial for small-angle rotation gates, which are the main components of product-formula circuits.

Under the SMM protocol, the effective logical error rate for executing an analog rotation gate $\hat{R}_P(\theta_L)$ is formally described as

$$P_L(\theta_L) = \alpha_{\text{RUS}}(\theta_L) \cdot \theta_L \cdot p_{\text{ph}}, \quad (38)$$

where p_{ph} is the physical error rate, and $\alpha_{\text{RUS}}(\theta_L)$ is defined as the RUS factor [52]. The angular dependence of the RUS factor $\alpha_{\text{RUS}}(\theta_L)$ accounts for parameter choices such as the threshold θ_{th} and physical error rate p_{ph} , as demonstrated in Ref. [52] and Appendix F. In the SMM protocol, this logical error arising from the $\hat{R}_P(\theta_L)$ gate is mitigated using the probabilistic error cancellation technique [82, 83]. This error mitigation process is accompanied by an increased sampling overhead $\gamma_{\theta_L}^2$, which is approximately given by $\gamma_{\theta_L}^2 \simeq 1 + 4P_L(\theta_L)$ [52].

Now, consider a quantum circuit composed of N_{rot} analog Pauli rotation gates with rotation angles $\{\theta_j\}_{j=1,2,\dots,N_{\text{rot}}}$. The total logical error rate for this circuit is described as

$$P_{\text{total}} = \sum_{j=1}^{N_{\text{rot}}} P_L(\theta_j) = \sum_{j=1}^{N_{\text{rot}}} \alpha_{\text{RUS}}(\theta_j) \cdot |\theta_j| \cdot p_{\text{ph}}, \quad (39)$$

and the corresponding total sampling overhead is given by

$$\gamma_{\text{total}}^2 = \prod_{j=1}^{N_{\text{rot}}} \gamma_{\theta_j}^2 \simeq e^{4P_{\text{total}}}. \quad (40)$$

In the following resource estimation, we estimate the total time-to-solution by considering the error mitigation overhead based on Eq. (40).

B. Resource estimation framework

We now describe the detailed resource estimation framework based on the SMM protocol. Our goal is

not to provide asymptotic bounds, but rather to obtain concrete, end-to-end estimates for QPE execution under early-FTQC constraints. Accordingly, we focus on physically meaningful metrics that directly capture early-FTQC hardware limitations, including physical qubit counts, circuit execution time, total time-to-solution, and achievable parallelism.

To obtain these physical resource estimates, we first determine the algorithmic gate cost for partially randomized RPE, as described in Sec. II B 4. Specifically, for product-formula circuits $\{\mathcal{C}_m\}_{m=0,1,\dots,M}$ approximating the time evolution $e^{-it_m\hat{H}}$ ($t_m = 2^m$), we estimate the number of non-Clifford Pauli rotation gates, denoted $\{G_m\}_{m=0,1,\dots,M}$, and the number of shots for each circuit, $\{N_m\}_{m=0,1,\dots,M}$, required to execute the RPE algorithm. Throughout this paper, algorithmic costs are estimated for a target precision corresponding to chemical accuracy, $\epsilon = 1.6$ mHa.

Next, we translate the algorithmic cost into physical resource estimates using the SMM-based partially fault-tolerant quantum computing architecture. In this scheme, time-evolution circuits are decomposed into a sequence of Clifford gates and non-Clifford Pauli-rotation gates, which are then implemented via sequential Pauli-based computation [84], combined with SMM. To estimate physical resources, we first determine the code distance d of the underlying surface code, which is chosen to suppress logical errors from Clifford operations. Specifically, we adopt prior results for a rotated surface code, which state that the logical error rate per code cycle is approximately given by [88]

$$p_L(p_{\text{ph}}, d) = 0.1 \times (100p_{\text{ph}})^{(d+1)/2}. \quad (41)$$

The optimal code distance d is determined such that the probability of a single logical error on any of the logical patches is less than 1%, following prior studies [30, 49, 84]. For a quantum circuit composed of N_{rot} Pauli rotations with rotation angles $\{\theta_j\}_{j=1,\dots,N_{\text{rot}}}$, this condition is formally expressed as

$$p_L(p_{\text{ph}}, d)^{-1} \geq 100 \times d N_{\text{patch}} C_{\text{total}}, \quad (42)$$

where N_{patch} is the number of logical code patches and C_{total} denotes the total number of “clocks”—corresponding to d code cycles—required to execute the circuit, and is defined as

$$C_{\text{total}} := \sum_{j=1}^{N_{\text{rot}}} C_{\text{smm}}(\theta_j). \quad (43)$$

Here, $C_{\text{smm}}(\theta_L)$ denotes the number of clocks required to execute a single analog rotation with angle θ_L using SMM. The remaining Clifford errors, kept to at most 1%, can then be mitigated with almost negligible overhead using probabilistic error cancellation [28, 89]. We determine the optimal code distance d_m for each circuit \mathcal{C}_m according to Eq. (42). Note that the code distance can

be chosen separately for each circuit \mathcal{C}_m , as each is executed independently in the single-ancilla QPE scheme.

Once the code distance is determined, the physical space-time costs for the RPE algorithm can be estimated. The number of physical qubits required per quantum processing unit (QPU) is estimated as $\mathcal{Q}_{\text{QPU}} = N_{\text{patch}} \times 2d_{\text{max}}^2$, where $d_{\text{max}} := d_M$ is the maximum code distance across the circuit set $\{\mathcal{C}_m\}_{m=0,1,\dots,M}$. Throughout this paper, we assume that lattice surgery operations are executed using the *fast block layout* [84], which requires $2N_L + \sqrt{8N_L} + 1$ patches to store N_L logical data qubits. In the SMM protocol, an additional 10 patches are introduced to ensure a sufficient supply of non-Clifford ancilla states, resulting in a code layout with $N_{\text{patch}} = 2N_L + \sqrt{8N_L} + 11$ [52]. The time cost is estimated by specifying a physical timescale for a single code cycle. Current superconducting qubit chips achieve single-round syndrome measurements in less than 1 μs [90, 91]. Therefore, we assume a 1 μs duration for a single code cycle, consistent with previous works [30, 49, 92, 93]. The circuit runtime per single shot of the RPE algorithm is therefore evaluated as

$$\mathcal{T}_m = C_{\text{total},m} d_m \quad [\mu\text{s}], \quad (44)$$

where $C_{\text{total},m} := \sum_{j=1}^{G_m} C_{\text{smm}}(\theta_j)$ denotes the total number of clocks required for executing circuit \mathcal{C}_m . Since the last round ($m = M$) requires the deepest circuit, the maximum per-shot circuit runtime is given by $\mathcal{T}_{\text{max}} := \mathcal{T}_M$. Multiplying the sampling cost by each circuit runtime \mathcal{T}_m , the total time-to-solution is formally expressed as

$$\mathcal{T}_{\text{total}} = \sum_{m=0}^M e\gamma_m^2 N_m \mathcal{T}_m \quad [\mu\text{s}], \quad (45)$$

where $\gamma_m^2 \simeq e^{4P_{\text{total},m}}$ with $P_{\text{total},m} = \sum_{j=1}^{G_m} \alpha_{\text{RUS}}(\theta_j) \cdot |\theta_j| \cdot p_{\text{ph}}$ is the sampling overhead for probabilistic error cancellation, as given by Eq. (40). The prefactor $e \simeq 2.72$ arises from the sampling overhead associated with the randomized product formula.

To estimate physical space-time resources according to this procedure, we also need to specify the actual rotation-angle dependence of $C_{\text{smm}}(\theta_L)$ and $\alpha_{\text{RUS}}(\theta_L)$. This dependence is determined by implementation details of SMM, such as the threshold θ_{th} and the physical error rate p_{ph} . We remark here that the SMM protocol exhibits a trade-off between per-gate execution time $C_{\text{smm}}(\theta_L)$ and the logical error factor $\alpha_{\text{RUS}}(\theta_L)$, especially when the target logical rotation angle θ_L is relatively large [52]. In the SMM protocol, large-angle rotation gates are primarily executed through the magic state cultivation process [85], which is accurate but slow due to T -gate synthesis. This process can be accelerated by directly executing such large-angle rotations without T -gate synthesis, by choosing a sufficiently large threshold ratio $\theta_{\text{th}}/\theta_L$. However, this simultaneously increases the failure probability of the RUS process and the logical error rate.

Maximizing the performance of SMM therefore requires careful adjustment of the threshold angle θ_{th} . In this paper, for simplicity, we determine $C_{\text{smm}}(\theta_L)$ and $\alpha_{\text{RUS}}(\theta_L)$ for two distinct patterns:

1. In the ‘‘accuracy-prioritized’’ setting, the threshold θ_{th} is optimized for each target angle θ_L such that the resulting logical error rate and RUS factor $\alpha_{\text{RUS}}(\theta_L)$ are minimized.
2. In the ‘‘speed-prioritized’’ setting, the maximum threshold ratio $\theta_{\text{th}}/\theta_L$ is fixed to a sufficiently large value, leading to low accuracy but fast execution of large-angle analog rotations.

Further technical details and the actual θ_L -dependence of $C_{\text{smm}}(\theta_L)$ and $\alpha_{\text{RUS}}(\theta_L)$ are presented in Appendix F. It is worth noting that a more granular adjustment of the threshold ratio $\theta_{\text{th}}/\theta_L$ might further reduce space-time resources. Such optimization of SMM performance is left for future study.

Finally, we account for the possibility of parallel execution across multiple QPUs operating concurrently. For a given physical-qubit budget $\mathcal{Q}_{\text{budget}}$, we define the maximum parallelism factor $k^* = \lfloor \mathcal{Q}_{\text{budget}}/\mathcal{Q}_{\text{QPU}} \rfloor$ as the largest number of identical QPUs that can be instantiated simultaneously without exceeding the total qubit budget. The corresponding parallelized time-to-solution is obtained by dividing the single-QPU runtime by k^* . Here, we emphasize that these QPUs are assumed to operate independently without coherent interconnection, in contrast to distributed quantum computing architectures [53, 54]. The distinction between single-QPU and multi-QPU execution is essential for assessing the feasibility of single-ancilla QPE schemes (such as RPE), where the total time-to-solution can be substantially shortened by executing individual circuits in parallel within a fixed hardware budget. For the following resource estimation, we set $\mathcal{Q}_{\text{budget}} = 5 \times 10^5$. This budget is significantly smaller than the physical qubit requirement for a full-fledged fault-tolerant QPE framework, which typically exceeds millions of qubits for large-scale molecular models [20–26, 51]. For reference, we present resource estimates for qubitized QPE under a full-fledged FTQC architecture in Appendix H.

C. End-to-end resource estimates for molecules

We now present end-to-end resource estimates for executing QPE on early-FTQC hardware, following the framework described in Sec. VB. Our analysis combines the algorithmic gate counts obtained from partially randomized time evolution with UWC-optimized Hamiltonians (Sec. III) and the SMM-based resource estimation framework to yield physical space-time costs for a broad set of molecular active-space models. The following resource estimations primarily focus on a currently realistic physical error rate of $p_{\text{ph}} = 10^{-3}$. Resource estimates

for more optimistic physical error rates, reflecting anticipated improvements in future hardware performance (specifically, $p_{\text{ph}} = 5 \times 10^{-4}$ and $p_{\text{ph}} = 10^{-4}$), are presented in Sec. VC4.

1. Resource reduction by partial randomization and UWC

We first demonstrate the impact of partial randomization and UWC on physical resource estimates. Figure 5 compares the single-QPU time-to-solution $\mathcal{T}_{\text{total}}$ for the initial-state parameter $\xi = 0.01$ across three schemes: second-order Trotterized evolution, partially randomized product-formula evolution, and partially randomized product-formula evolution combined with UWC. For the second-order Trotterized evolution estimates, we truncate the smallest coefficients of the Hamiltonian \hat{H} such that the total weight of truncated terms is at most a small threshold 10^{-3} [41]. The partially randomized product formula is composed of deterministic second-order Trotterization and randomized qDRIFT parts, as described in Sec. IV B. Across all benchmark models, partial randomization alone achieves a one-to-two orders of magnitude reduction in time-to-solution from fully deterministic Trotterization. Combining UWC with partial randomization further yields an additional one-to-two orders of magnitude reduction in time-to-solution compared to the partial randomization alone. In total, partial randomization combined with UWC achieves a two-to-three orders of magnitude reduction in time-to-solution, reflecting the gate-count reduction shown in Fig. 4.

The absolute values of the time-to-solution in Fig. 5 are also noteworthy. For Trotterized evolution of the original Hamiltonian representation, the time-to-solution lies in the range of 10^3 to 10^5 days, or equivalently, several years to centuries, rendering it impractical. Partial randomization and UWC reduce this unrealistic time-to-solution to a realistic range of several days to weeks.

It is also worth noting that the code distance and the resulting physical qubit count per QPU (\mathcal{Q}_{QPU}) are reduced due to the gate count reduction enabled by partial randomization and UWC. For instance, the physical qubit count required to simulate the P450-Cpd I (E) model for $\xi = 0.01$ is $\mathcal{Q}_{\text{QPU}} = 2.32 \times 10^5$ for Trotterization, while $\mathcal{Q}_{\text{QPU}} = 1.41 \times 10^5$ for partial randomization combined with UWC, representing an approximately 40% reduction in physical qubit overhead. This physical qubit reduction also influences the time-to-solution when using multiple QPUs, since the available QPU parallelism k^* increases under a fixed qubit budget.

2. Physical resource estimates for molecular active-space models

We now present physical resource estimates for a range of chemically relevant molecular active-space models employing partial randomization combined with UWC.

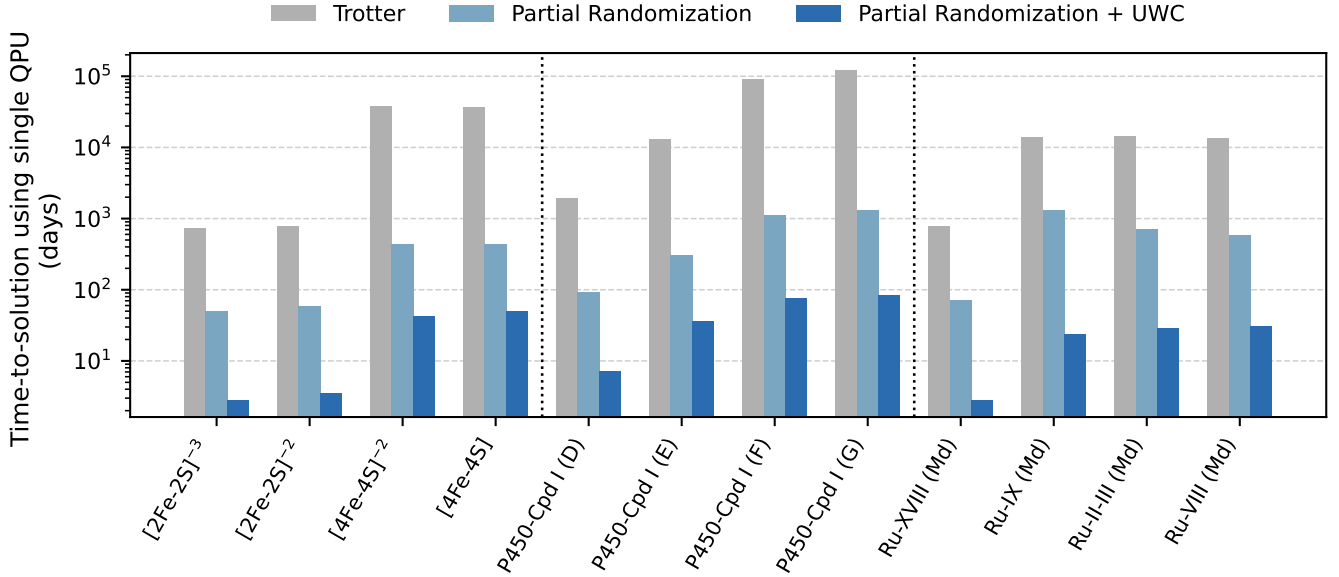


FIG. 5. Time-to-solution for representative molecular active-space models, utilizing a single QPU. The figure compares three schemes: second-order Trotterization (gray bars), partially randomized time evolution (light-blue cross-hatched bars), and partially randomized time evolution combined with UWC (blue hatched bars), all calculated for an initial-state parameter of $\xi = 0.01$. All values are presented in days. The target accuracy ϵ and physical error rate p_{ph} are assumed to be $\epsilon = 1.6$ mHa and $p_{\text{ph}} = 10^{-3}$, respectively.

TABLE III. Physical resource estimates for the RPE algorithm applied to representative molecular active-space models. These estimates are derived from partially randomized product-formula circuits and UWC-optimized Pauli-LCU Hamiltonian representations. The initial-state infidelity parameter is set to $\xi = 0.01$, corresponding to an initial-state overlap $p_0 = |\langle \psi_0 | \psi \rangle|^2 > 0.99$. The target accuracy ϵ and physical error rate p_{ph} are assumed to be $\epsilon = 1.6$ mHa and $p_{\text{ph}} = 10^{-3}$, respectively.

Molecule ID	Physical qubits per QPU	Maximum per-shot runtime [s]	Time-to-solution (single QPU) [days]	QPU parallelism k^* ($Q_{\text{budget}} = 5 \times 10^5$)	Time-to-solution (k^* QPUs) [days]
(a) Iron-sulfur clusters					
[2Fe-2S] ⁻³	8.02×10^4	2.40×10^0	2.81×10^0	6	4.68×10^{-1}
[2Fe-2S] ⁻²	8.02×10^4	3.09×10^0	3.39×10^0	6	5.65×10^{-1}
[4Fe-4S] ⁻²	1.60×10^5	4.92×10^1	4.23×10^1	3	1.41×10^1
[4Fe-4S]	1.60×10^5	4.97×10^1	4.88×10^1	3	1.63×10^1
(b) Cytochrome P450					
P450-Cpd I (D)	8.98×10^4	6.36×10^0	7.19×10^0	5	1.44×10^0
P450-Cpd I (E)	1.41×10^5	3.29×10^1	3.58×10^1	3	1.19×10^1
P450-Cpd I (F)	2.15×10^5	6.76×10^1	6.89×10^1	2	3.44×10^1
P450-Cpd I (G)	2.24×10^5	7.85×10^1	8.40×10^1	2	4.20×10^1
(c) Ruthenium-based catalysts for CO ₂ utilization					
Ru-XVIII (Md)	8.02×10^4	2.78×10^0	2.78×10^0	6	4.63×10^{-1}
Ru-IX (Md)	1.21×10^5	1.91×10^1	2.36×10^1	4	5.91×10^0
Ru-II-III (Md)	1.33×10^5	2.01×10^1	2.81×10^1	3	9.37×10^0
Ru-VIII (Md)	1.33×10^5	2.10×10^1	3.03×10^1	3	1.01×10^1

Table III summarizes the physical resource estimates for representative molecular models, first listed in Table II, for $\xi = 0.01$. For each molecular instance, we list the number of physical qubits required per QPU (Q_{QPU}), the maximum per-shot circuit execution time

($\mathcal{T}_{\text{max}} = \mathcal{T}_M$), the total time-to-solution assuming a single QPU ($\mathcal{T}_{\text{total}}$), and the degree of QPU parallelism ($k^* = \lfloor Q_{\text{budget}} / Q_{\text{QPU}} \rfloor$) achievable given a budget of $Q_{\text{budget}} = 5 \times 10^5$ physical qubits. The logical resources used to derive these values, such as the analog rotation

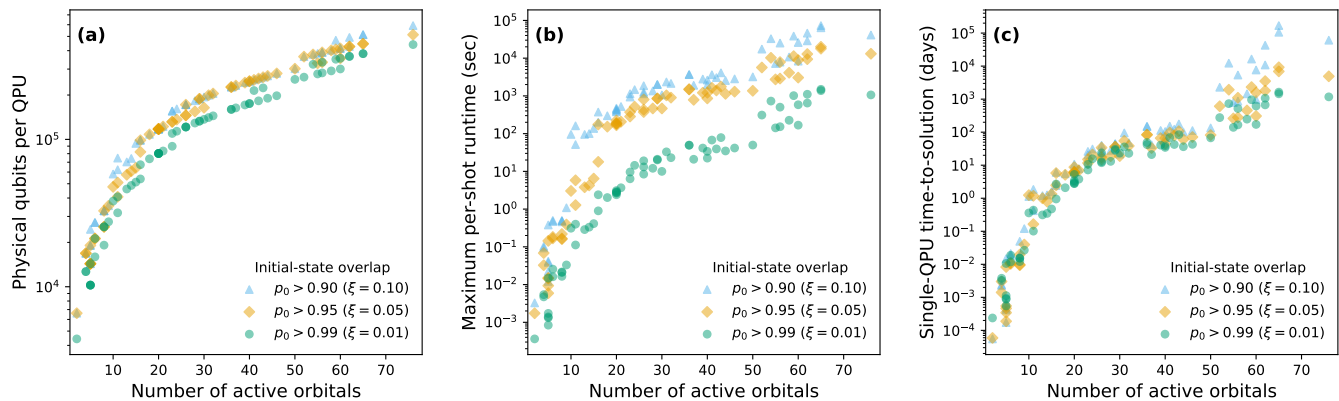


FIG. 6. Scaling of key resource components for partially randomized RPE on SMM-based partially fault-tolerant quantum computing architectures. (a) Number of physical qubits required per QPU (\mathcal{Q}_{QPU}), (b) Maximum per-shot runtime (\mathcal{T}_{max}), and (c) time-to-solution for single QPU execution ($\mathcal{T}_{\text{total}}$) as a function of the number of active orbitals. The marker shape in all panels indicates the initial-state infidelity parameter ξ , along with the corresponding lower bound for the initial-state overlap $p_0 = |\langle \psi_0 | \psi \rangle|^2$. Panels (b) and (c) use different time units to emphasize the distinct physical meanings of per-circuit execution cost and overall computational effort. All data points are derived from UWC-optimized Hamiltonian representations of benchmark molecular active-space models, detailed in Appendix E 1, encompassing hydrogen chains, iron-sulfur clusters, P450 active sites, and ruthenium-based catalysts. The target accuracy ϵ and physical error rate p_{ph} are assumed to be $\epsilon = 1.6$ mHa and $p_{\text{ph}} = 10^{-3}$, respectively.

gate count and code distance, are provided for all molecular models in Appendix E 2 a.

For instance, ground-state energy estimation for the 31-orbital P450-Cpd I (E) model can be executed within 36 days using a QPU with 1.41×10^5 physical qubits, assuming $p_{\text{ph}} = 10^{-3}$. The physical qubit count is on the order of 10^5 , and is therefore expected to be suitable for early-FTQC hardware. Assuming an available physical-qubit budget of $\mathcal{Q}_{\text{budget}} = 5 \times 10^5$, parallel execution using $k^* = 3$ QPUs is possible, reducing the time-to-solution to within 12 days. It is noteworthy that the maximum per-shot runtime \mathcal{T}_{max} is less than 30 seconds, significantly smaller than the total time-to-solution. This reflects a characteristic of single-ancilla QPE, which relies on a large number of repetitions of low-depth quantum circuits.

To complement these representative values, Fig. 6 presents the corresponding resource estimates for the full benchmark set as a function of the number of active orbitals for initial-state infidelity parameters $\xi \in \{0.1, 0.05, 0.01\}$, corresponding to initial-state overlaps $p_0 > 0.9$. Specifically, the physical qubit requirement per QPU, the maximum per-shot circuit execution time, and the single QPU time-to-solution are plotted for all molecular instances considered in this work. See Appendix E for model details and actual resource estimate values.

Across the benchmark set, Fig. 6(a) demonstrates that the physical qubit requirement per QPU grows almost linearly with active-space size and remains well below $\sim 10^6$, a typical requirement for a full-fledged FTQC setting. This linear behavior arises from the fact that the logical qubit count N_L is proportional to the number of orbitals N as $N_L = 2N + 1$, including $2N$ data qubits

encoding spin-orbitals and a single ancilla qubit for the Hadamard test.

In contrast, the maximum per-shot runtime \mathcal{T}_{max} (Fig. 6(b)) and the single QPU time-to-solution $\mathcal{T}_{\text{total}}$ (Fig. 6(c)) exhibit a much stronger and complex dependence on the number of active orbitals. This primarily reflects the combined effects of the increased gate count and sampling overhead inherent in the SMM protocol. Consequently, molecular models with more than 50 orbitals become impractical to execute on a single QPU due to the prohibitive time-to-solution.

We note that the absolute values of these resource estimates strongly depend on assumptions regarding the initial-state overlap, which are quantified by the parameter ξ . When the initial-state overlap is increased (or equivalently, ξ is decreased), the maximum per-shot runtime \mathcal{T}_{max} can be significantly reduced, largely in accordance with the algorithmic scaling shown in Table I. The behavior of the total time-to-solution $\mathcal{T}_{\text{total}}$ is primarily determined by the combined effects of the algorithmic scaling and the error mitigation cost of SMM. Specifically, $\mathcal{T}_{\text{total}}$ increases exponentially, as shown in Eq. (45), when both the maximum circuit depth and the resulting total logical error rate P_{total} are relatively large. Such behavior is observed in Fig. 6(c) for models with more than 50 orbitals, where the value of $\mathcal{T}_{\text{total}}$ increases exponentially for larger ξ .

3. Feasibility map

To synthesize the resource estimates presented previously and to clarify the practical scope of early-FTQC

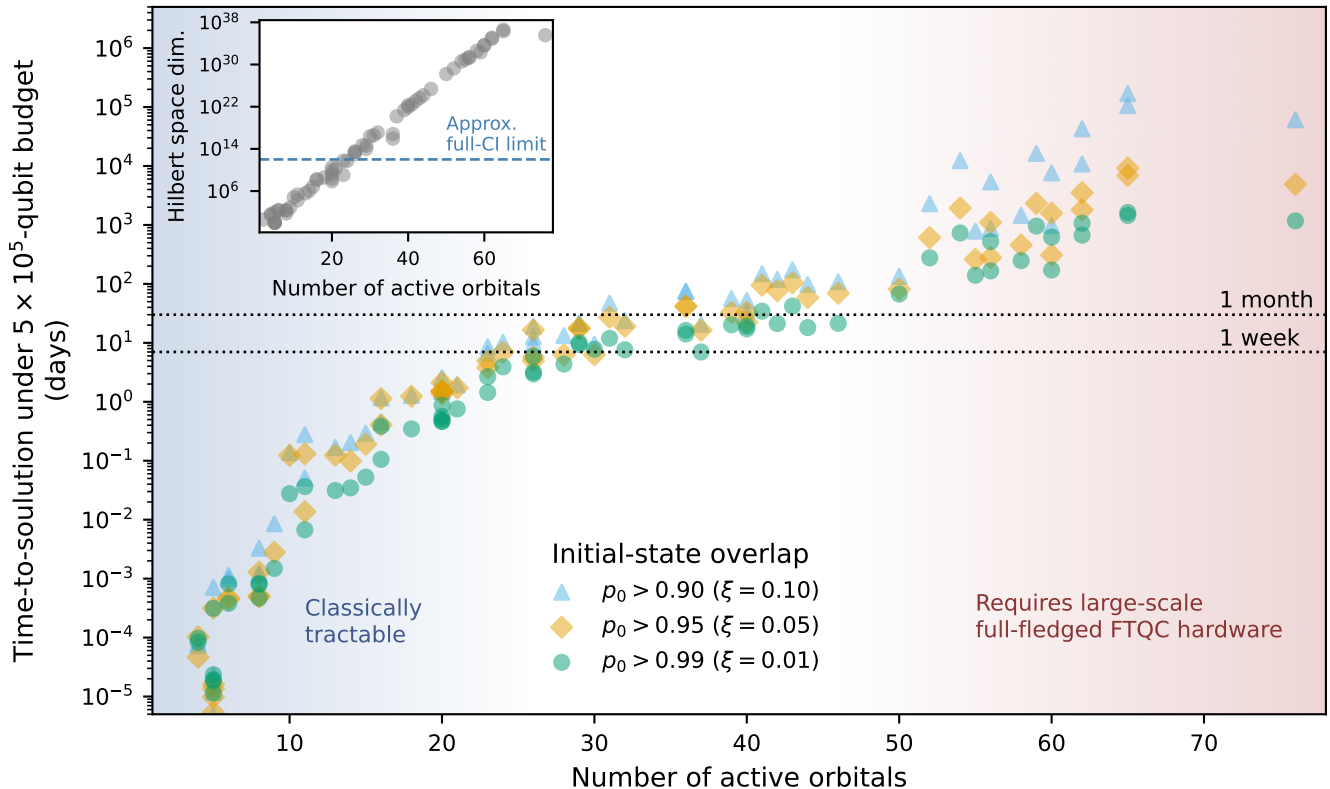


FIG. 7. Feasibility map for ground-state energy estimation via partially randomized RPE under a fixed physical-qubit budget of $Q_{\text{budget}} = 5 \times 10^5$. The figure shows the time-to-solution within the SMM-based partially fault-tolerant quantum computing architecture as a function of the number of active orbitals. For each system, the degree of parallelism is chosen as the maximum allowed by the qubit budget, enabling the independent execution of Hadamard test circuits. The marker shape indicates the initial-state infidelity parameter ξ , along with the corresponding lower bound for the initial-state overlap $p_0 = |\langle \psi_0 | \psi \rangle|^2$. The horizontal dotted lines mark representative timescales of 1 week and 1 month, indicating practical targets for sustained quantum-chemical calculations. Shaded regions denote regimes that are classically tractable (blue-gray) and those requiring large-scale full-fledged FTQC hardware with substantially larger qubit counts (red-gray), while the intermediate region highlights the operating window of early-FTQC processors. The inset shows the Hilbert space dimension as a function of the number of active orbitals; the approximate full-CI limit of $\sim 10^{12}$ is indicated by the dashed line. Together, this map identifies a range of chemically relevant systems beyond the reach of classical full-CI methods for which accurate ground-state energy estimation may be achievable on early-FTQC hardware. For each data point, the reported time-to-solution corresponds to the value obtained for UWC-optimized Hamiltonian representations of benchmark molecular active-space models, detailed in Appendix E 1, encompassing hydrogen chains, iron-sulfur clusters, P450 active sites, and ruthenium-based catalysts. The target accuracy ϵ and physical error rate p_{ph} are assumed to be $\epsilon = 1.6$ mHa and $p_{\text{ph}} = 10^{-3}$, respectively.

for chemistry, we construct a feasibility map that summarizes the execution requirements across system size and runtime constraints. This map provides a compact, architecture-aware view of which molecular active-space models can realistically be addressed within a fixed physical-qubit budget and execution-time horizon.

Figure 7 plots the estimated time-to-solution for executing the partially randomized RPE algorithm under a fixed total physical-qubit budget of $Q_{\text{budget}} = 5 \times 10^5$ as a function of the number of active orbitals N . For each molecular instance, the plotted time-to-solution is derived assuming parallel execution using k^* QPUs, as described in Sec. V B. This representation explicitly incorporates the trade-off among circuit depth, repeated

sampling, and available parallelism, which is central to single-ancilla QPE algorithms in the early-FTQC regime.

The feasibility map delineates three qualitatively distinct regions. At small orbital counts, specifically $N \lesssim 20$, the problem lies within the reach of classical full-CI methods [2, 3], as also shown in the inset of Fig. 7, implying that quantum computation offers no clear advantage. Conversely, for very large orbital counts, $N \gtrsim 50$, the required time-to-solution far exceeds practical limits even when full parallelism under the fixed qubit budget is exploited, placing these systems beyond the reach of early-FTQC hardware. Between these extremes, the map identifies an intermediate regime in which ground-state energy estimation via RPE can be executed within days

TABLE IV. Sensitivity of resource estimates to the assumed physical error rate. This table compares the physical space-time cost for representative benchmark systems under two different physical error rates, $p_{\text{ph}} = 10^{-3}$, $p_{\text{ph}} = 5 \times 10^{-4}$, and $p_{\text{ph}} = 10^{-4}$, for $\xi = 0.01$. Specifically, it lists the physical qubits per QPU and single-QPU time-to-solution for selected models. The data for $p_{\text{ph}} = 10^{-4}$ is derived using the SMM protocol’s performance calibrated at $p_{\text{ph}} = 5 \times 10^{-4}$, as further explained in the text.

Molecule ID	Orbitals	Physical qubits per QPU			Time-to-solution (single QPU) [days]		
		$p_{\text{ph}} = 10^{-3}$	$p_{\text{ph}} = 5 \times 10^{-4}$	$p_{\text{ph}} = 10^{-4}$	$p_{\text{ph}} = 10^{-3}$	$p_{\text{ph}} = 5 \times 10^{-4}$	$p_{\text{ph}} = 10^{-4}$
(a) Iron-sulfur clusters							
$[2\text{Fe-2S}]^{-3}$	20	8.02×10^4	5.00×10^4	1.80×10^4	2.81×10^0	1.55×10^0	6.20×10^{-1}
$[2\text{Fe-2S}]^{-2}$	20	8.02×10^4	5.00×10^4	1.80×10^4	3.39×10^0	1.94×10^0	7.87×10^{-1}
$[4\text{Fe-4S}]^{-2}$	36	1.60×10^5	1.05×10^5	4.38×10^4	4.23×10^1	2.59×10^1	1.29×10^1
$[4\text{Fe-4S}]$	36	1.60×10^5	1.05×10^5	4.38×10^4	4.88×10^1	2.74×10^1	1.31×10^1
(b) Cytochrome P450							
P450-Cpd I (D)	23	8.98×10^4	5.60×10^4	2.02×10^4	7.19×10^0	3.70×10^0	1.58×10^0
P450-Cpd I (E)	31	1.41×10^5	9.22×10^4	3.86×10^4	3.58×10^1	1.98×10^1	8.90×10^0
P450-Cpd I (F)	41	2.15×10^5	1.17×10^5	4.91×10^4	6.89×10^1	3.51×10^1	1.65×10^1
P450-Cpd I (G)	43	2.24×10^5	1.22×10^5	5.12×10^4	8.40×10^1	4.13×10^1	1.92×10^1
(c) Ruthenium-based catalysts for CO ₂ utilization							
Ru-XVIII (Md)	20	8.02×10^4	5.00×10^4	1.80×10^4	2.78×10^0	1.67×10^0	6.96×10^{-1}
Ru-IX (Md)	26	1.21×10^5	6.19×10^4	2.23×10^4	2.36×10^1	1.11×10^1	4.35×10^0
Ru-II-III (Md)	29	1.33×10^5	6.78×10^4	2.44×10^4	2.81×10^1	1.17×10^1	4.57×10^0
Ru-VIII (Md)	29	1.33×10^5	6.78×10^4	3.65×10^4	3.03×10^1	1.21×10^1	5.80×10^0

to weeks, utilizing $\sim 10^5$ physical qubits. Importantly, **this qubit scale remains below the regime** typically associated with multi-cryostat distributed architectures [53], reinforcing the practical relevance of this intermediate window within the early-FTQC regime.

Notably, this intermediate region encompasses active-space models with approximately 20–50 orbitals, which are already well beyond the capabilities of classical full-CI computation [2, 3]. Although these systems remain smaller than those with more than 50 orbitals—typically targeted in proposals for full-fledged fault-tolerant, millions-of-qubit quantum computers [20–26, 51, 55]—they represent a scientifically meaningful and practically relevant class of problems for early fault-tolerant quantum chemistry simulations.

We emphasize that the boundaries shown in Fig. 7 are not sharp transitions but rather reflect smooth crossovers determined by time-to-solution thresholds, qubit-budget constraints, and assumptions regarding initial-state overlap and error tolerance. Nevertheless, the feasibility map provides a concrete and experimentally relevant target for early-FTQC hardware, clarifying how algorithmic optimizations, such as partially randomized time evolution and UWC, translate into practical capabilities at the system level.

4. Resource estimates at reduced physical error rates

To assess the sensitivity of resource requirements to hardware performance, we present resource estimation data for reduced physical error rates of $p_{\text{ph}} = 5 \times 10^{-4}$

and $p_{\text{ph}} = 10^{-4}$. By providing these estimates and comparing them with those for $p_{\text{ph}} = 10^{-3}$, we demonstrate the significant impact of improved hardware fidelity on required quantum resources.

Table IV summarizes the physical space-time cost, physical qubits per QPU and time-to-solution under single-QPU execution, for representative molecular models (as detailed in Table II) at both $p_{\text{ph}} = 10^{-3}$ and the more optimistic $p_{\text{ph}} = 5 \times 10^{-4}$ and $p_{\text{ph}} = 10^{-4}$. While this table highlights the reductions for representative molecules, a comprehensive analysis of the resource scaling trends across the full benchmark set at $p_{\text{ph}} = 5 \times 10^{-4}$ and $p_{\text{ph}} = 10^{-4}$ is provided in Appendix G. For the $p_{\text{ph}} = 10^{-4}$ case, the data are obtained by leveraging the SMM protocol’s performance calibrated at $p_{\text{ph}} = 5 \times 10^{-4}$ (see Fig. 9 in Appendix F). This approach is necessitated because the performance data for $p_{\text{ph}} = 10^{-4}$ is not directly available in Ref. [85] for magic state cultivation protocols, which form the basis for SMM [52]. Crucially, since the SMM protocol’s performance at $p_{\text{ph}} = 10^{-4}$ is guaranteed to be no worse than at $p_{\text{ph}} = 5 \times 10^{-4}$ (due to higher fidelity), our resource estimates for $p_{\text{ph}} = 10^{-4}$ provide a conservative upper bound.

As quantitatively demonstrated in Table IV, reducing the physical error rate has significant impacts on resource requirements. Halving the physical error rate from the baseline $p_{\text{ph}} = 10^{-3}$ to $p_{\text{ph}} = 5 \times 10^{-4}$ reduces the number of physical qubits by approximately 34–49% and the single-QPU time-to-solution by about 39–60%. This effect is even more pronounced as the error rate improves to $p_{\text{ph}} = 10^{-4}$, leading to a substantial reduction of approximately 73–82% in physical qubits and 70–84% in

the time-to-solution, compared to the $p_{\text{ph}} = 10^{-3}$ case. These findings underscore that lowering the physical error rate directly expands the scope of solvable problems under practical time and qubit constraints. This improvement translates to an effective expansion of the feasibility window shown in Fig. 7, critically advancing the timeline for achieving practical chemistry simulations on quantum computers.

VI. CONCLUSION

In this work, we have investigated the feasibility of QPE-based ground-state energy estimation for chemically relevant molecular systems on early-FTQC hardware. Focusing on hardware platforms with physical qubit budgets on the order of 10^5 , we combined single-ancilla QPE with partially randomized product formula and introduced a novel Hamiltonian-optimization strategy, UWC, to reduce algorithmic cost under early-FTQC constraints.

We demonstrated that the partially randomized product formula alone yields substantial reductions in gate count relative to deterministic Trotterization. Furthermore, the additional application of UWC systematically enhances these gains by concentrating the Hamiltonian coefficient distribution. Across a diverse benchmark set of molecular active-space models, including iron-sulfur clusters, cytochrome P450 active sites, and ruthenium-based catalysts, the combined approach achieves gate-count reductions of approximately three orders of magnitude relative to deterministic Trotter baselines. These algorithmic improvements translate directly into reduced circuit depth and non-Clifford gate overheads, which are critical bottlenecks in the early-FTQC regime.

Building on these algorithmic improvements, we performed an end-to-end resource estimation for the STAR architecture using a framework that incorporates the SMM improvement [52]. Our analysis accounts for physical qubit overhead, per-shot circuit runtime, and total time-to-solution, including the effects of parallel execution under a fixed qubit budget. Our results identify a concrete feasibility window in which active-space models with approximately 20–50 orbitals—well beyond the reach of classical full-CI computations—can be addressed within days to weeks of time-to-solution using at most 5×10^5 physical qubits. The resulting feasibility map delineates a practically meaningful intermediate regime between classically tractable systems and the large-scale molecular targets envisioned for full-fledged fault-tolerant, millions-of-qubit quantum computers. Notably, this feasibility window lies below the scale at which distributed, multi-cryostat architectures become necessary for fault-tolerant operation [53], underscoring its relevance as a realistic intermediate milestone.

Several important algorithmic directions remain for future work. First, the resource estimates presented here assume a relatively high overlap between the prepared

initial state and the true ground state. While algorithms capable of achieving such overlaps are known [19, 34, 60–64], their resource requirements can be substantial for strongly correlated molecules and, in some cases, may be comparable or exceed the cost of the time-evolution circuits used in QPE itself [64, 94]. Achieving practical quantum advantage in quantum chemistry will therefore necessitate the development of state-preparation techniques that can reliably produce high-overlap initial states at a cost comparable to—or lower than—that of the subsequent time-evolution operations. In addition, while this work focused on Pauli-LCU representations, extending partially randomized time evolution and UWC to alternative LCU forms, such as double factorized LCU representation [59] and other fermionic LCU representations [36, 95], is an interesting avenue for future research. If the effective weight concentration in such LCU representations can be enhanced, even larger gate-count reductions may become possible. Finally, the UWC framework itself is flexible and could incorporate alternative cost metrics beyond gate count. These could include rotation angles that directly affect execution time and logical error rates in STAR-based architectures [30, 52].

From an architectural perspective, our resource estimates considered two representative operating modes of the STAR architecture, corresponding to accuracy-prioritized and speed-prioritized configurations. In practice, these choices could be optimized in a problem-dependent manner, and further runtime reductions may be achievable through architecture-aware compilation. In particular, the STAR architecture admits parallel execution of rotation gates utilizing fermionic swap operations [31]. This suggests additional opportunities for acceleration by developing appropriate scheduling and compilation strategies, potentially utilizing a generalized fermionic swap protocol for molecular electronic structure Hamiltonians [96]. Moreover, the STAR architecture itself admits further improvement. Integrating recently proposed techniques [97, 98] may help reduce effective logical error rates, potentially increasing the tolerable circuit depth and relaxing initial-state overlap requirements for reliable QPE. While our analysis focused on superconducting platforms, extending this framework to other hardware modalities, such as neutral-atom arrays [99] and trapped-ion systems [100], is an important future direction. Differences in native gates, physical error rates, and execution times may substantially reshape the resulting feasibility landscape [101–103]. Finally, the implementation cost of fault-tolerant operations is continuously improving, as exemplified by recent advances such as magic state cultivation [85–87]. The precise physical resources required for full-fledged FTQC simulations using state-of-the-art qubitization-based QPE on these emerging architectures are not yet fully characterized. Therefore, continuously benchmarking early-FTQC approaches, such as the one presented here, against the evolving landscape of full-fledged FTQC is a crucial area for future work.

Taken together, our results demonstrate that while full-fledged fault-tolerant quantum computers are envisioned for simulations of even larger molecular models, chemically meaningful quantum chemistry problems can already become accessible in an experimentally relevant early fault-tolerant regime through co-designed algorithms, Hamiltonian representations, and error correction architecture optimized for early-FTQC constraints.

ACKNOWLEDGMENTS

We are grateful to Yutaro Akahoshi, Norifumi Matsumoto, Shinichiro Yamano, Koki Chinzei, and Quoc Hoan Tran for fruitful discussions. We are indebted to Jun Fujisaki, Shintaro Sato, and Keisuke Fujii for their support in fostering a conducive research environment. We also acknowledge Shintaro Sato and Keisuke Fujii for reviewing the manuscript. We acknowledge Masatoshi Ishii for technical support in performing numerical simulations.

DATA AVAILABILITY

The data that support the findings of this article are openly available [104].

AUTHOR CONTRIBUTIONS

S. K. was responsible for the detailed theoretical framework conceptualization, methodology development, and performing numerical simulations and resource estimation for all figures and tables. S. K. also led the primary investigation, performed formal data analysis, and prepared the original draft of the manuscript. R. T. contributed to the technical discussion on resource estimation in Sec. V and provided numerical data for the performance of the STAR-magic mutation protocol in Fig. 9. K. M. and H. O. were instrumental in securing necessary resources and overseeing project administration. All authors participated in the review and editing of the manuscript.

Appendix A: Robust phase estimation

In this Appendix, we detail the RPE algorithm [41, 47], which is briefly reviewed in Sec. II and serves as the cost model throughout this work. The analysis presented here follows the results detailed in Refs. [41, 47].

The core idea of RPE is to estimate the signal $g(t) := \langle \psi | e^{-it\hat{H}} | \psi \rangle$ for a given state $|\psi\rangle$ at timesteps $t = 2^m$ for $m = 0, 1, \dots, M$. The integer M is set to $M = \lceil \log_2 \epsilon^{-1} \rceil$ for estimating the ground state energy E_0 with target precision ϵ . In the m -th round, the Hadamard test shown

Algorithm 1 RPE algorithm for the large initial-state overlap regime [41, 47].

1: **Input:** ϵ : target precision, η : lower bound for the squared overlap $p_0 = |\langle \psi_0 | \psi \rangle|^2$, ξ : prefactor for the maximal timestep satisfying $1 > \xi > \frac{3}{\pi} \arcsin(\frac{1-\eta}{\eta})$, $M = \lceil \log_2(\frac{\xi}{\epsilon}) \rceil$: number of iterations, $\{N_m\}_{m=0}^M$: schedule of sample numbers per iteration.

2: $\vartheta_{-1} \leftarrow 0$

3: **for** $m = 0, 1, \dots, M$ **do**

4: Construct the estimator \bar{Z}_m by performing the Hadamard test (Fig. 1) with $t = 2^m$ for $N_m/2$ shots each for the real and imaginary parts.

5: Define a candidate set:

$$\mathcal{S}_m = \left\{ \frac{\arg(\bar{Z}_m) + 2\pi k}{2^m} \right\}_{k=0,1,\dots,2^m-1}.$$

6: Update the estimate by selecting the candidate closest to the previous estimate:

$$\vartheta_m \leftarrow \arg \min_{\vartheta \in \mathcal{S}_m} |\vartheta - \vartheta_{m-1}|_{2\pi}.$$

7: **end for**

8: $\vartheta^* \leftarrow \vartheta_M$

9: **Output:** ϑ^* as an estimate of E_0 .

in Fig. 1 with $t = 2^m$ is repeated $N_m/2$ times each for both the real part ($W = I$) and imaginary part ($W = S^\dagger$) to obtain the sampling mean \bar{Z}_m , which is an estimate of $g(2^m) = \langle \psi | e^{-i2^m \hat{H}} | \psi \rangle$. The angle $\arg(\bar{Z}_m)$ provides an estimate of $2^m E_0$ modulo 2π [47]. Then, the candidate set for E_0 at the m -th round is obtained as

$$\mathcal{S}_m := \left\{ \frac{\arg(\bar{Z}_m) + 2\pi k}{2^m} \right\}_{k=0,1,\dots,2^m-1}. \quad (\text{A1})$$

Given an estimate ϑ_{m-1} for E_0 from the previous $m-1$ rounds, an updated estimate of the ground-state energy, ϑ_m , is selected from the set \mathcal{S}_m as

$$\vartheta_m = \operatorname{argmin}_{\vartheta \in \mathcal{S}_m} |\vartheta - \vartheta_{m-1}|_{2\pi}, \quad (\text{A2})$$

where $|\vartheta_1 - \vartheta_2|_{2\pi} := \min_{n \in \mathbb{Z}} |\vartheta_1 - \vartheta_2 + 2n\pi|$ denotes the angular distance between ϑ_1 and ϑ_2 . If the input state $|\psi\rangle$ satisfies $p_0 := |\langle \psi | \psi_0 \rangle|^2 > \eta > 4 - 2\sqrt{3} \simeq 0.54$, this procedure achieves the Heisenberg-limited scaling in total runtime [47].

The RPE algorithm can be further refined for the regime where the initial-state overlap p_0 approaches 1 (i.e., $\eta \rightarrow 1$). In such a scenario, the maximum circuit depth can be reduced to $T_{\max} = \mathcal{O}((1-p_0)\epsilon^{-1})$ [47]. Specifically, the maximum number of iterations M is modified to $M = \lceil \log_2(\xi\epsilon^{-1}) \rceil$ with a prefactor ξ satisfying $1 > \xi > \frac{3}{\pi} \arcsin(\frac{1-\eta}{\eta})$. The modified RPE algorithm then proceeds as summarized in Algorithm 1.

In Algorithm 1, the number of samples $\{N_m\}$ is determined following Ref. [41]. For $m < M$, N_m is chosen

as

$$N_{m < M} = \frac{2}{\beta^2} (\log(\xi^{-1}) + \log 2(\alpha(M - m) + 1)), \quad (\text{A3})$$

where $\beta := \eta(1 + \sin(\frac{\pi}{3})) - 1$ and $\alpha > 1$ is a constant. Based on Hoeffding's inequality, this choice of N_m ensures that [41]

$$\mathbb{P}\left(\left|\arg(\bar{\mathcal{Z}}_m) - 2^m E_0\right|_{2\pi} \geq \frac{\pi}{3}\right) \leq \xi^2 4^{-\alpha(M-m)}. \quad (\text{A4})$$

The final round ($m = M$) requires $N_M = 2\xi^{-2}$ samples, leading to the following bound [41]:

$$\mathbb{E}\left(\left|\arg(\bar{\mathcal{Z}}_M) - 2^M E_0\right|_{2\pi}\right) \lesssim \xi^2. \quad (\text{A5})$$

Under the conditions in Eqs. (A4) and (A5), Ref. [41] shows that Algorithm 1 yields an estimate ϑ^* of E_0 such that

$$\mathbb{E}\left(\left|\vartheta^* - E_0\right|_{2\pi}^2\right) \leq (1 + \rho)\xi^2 4^{-M}, \quad (\text{A6})$$

where $\rho = \frac{1}{4^{\alpha-1}-1}(\frac{16\pi}{3})^2$ is a constant determined by the choice of $\alpha > 1$. In this work, we set $\alpha \simeq 10$ such that $\rho \simeq 10^{-3}$, which ensures that the prefactor $(1 + \rho)$ on the right-hand side of Eq. (A6) is close to unity. Consequently, the total evolution time T_{total} scales as $T_{\text{total}} \simeq N_M T_{\text{max}} = \mathcal{O}(\xi^{-1}\epsilon^{-1})$, exhibiting the trade-off between T_{max} and T_{total} , governed by ξ [41, 47].

Appendix B: Gate counts for partially randomized robust phase estimation

In this Appendix, we outline the gate cost model for the RPE algorithm when implemented with partially randomized product formulas. The analysis presented here follows the framework detailed in Ref. [41].

As described in Appendix A, the RPE algorithm proceeds by performing the Hadamard test on the time-evolution unitary $e^{-it\hat{H}}$ for $t = 2^m$, where $m = 0, 1, \dots, M$. We approximate this unitary using a quantum circuit based on the partially randomized product formulas introduced in Sec. II B. The Trotter step size δ is chosen to suppress this error to a negligible level. In this approach, only a part of the Trotter circuit $\hat{S}_p(\delta)^r \approx e^{-it\hat{H}}$ is stochastically implemented by randomized product formulas. Consequently, the overall circuit is subject to the inherent Trotter discretization error. The step size δ is determined to suppress this Trotter error to a negligible level. For QPE, the Trotter error is naturally quantified by the resulting bias in the ground-state energy, $\epsilon_{\text{trrot}} := |E_0 - E_{\text{eff},0}| \leq C_{\text{gs}}\delta^p$, as given in Eq. (8). The total estimation error arises from two independent sources: this Trotter error and the algorithmic error from the QPE protocol itself, ϵ_{qpe} . To achieve a total target precision ϵ for the true ground-state energy

E_0 , these errors are typically combined in quadrature, requiring:

$$\epsilon^2 = \epsilon_{\text{qpe}}^2 + \epsilon_{\text{trrot}}^2 \leq \epsilon_{\text{qpe}}^2 + C_{\text{gs}}^2 \delta^{2p}. \quad (\text{B1})$$

Applying the RPE algorithm to the Trotter unitary $\hat{S}_p(\delta)$ to estimate its eigenenergy $E_{\text{eff},0}$ with precision ϵ_{qpe} requires a maximum evolution time of $\mathcal{O}(\epsilon_{\text{qpe}}^{-1})$. This corresponds to $T_{\text{max}}/\delta \simeq \xi(\epsilon_{\text{qpe}}\delta)^{-1}$ applications of the Trotter step unitary $\hat{S}_p(\delta)$. Thus, the number of RPE rounds becomes $M = \lceil \log_2(\xi\epsilon_{\text{qpe}}^{-1}\delta^{-1}) \rceil$. The total number of Trotter steps, and therefore the gate count, scales as $\mathcal{O}(\epsilon_{\text{qpe}}^{-1}\delta^{-1}) = \mathcal{O}(\epsilon_{\text{qpe}}^{-1}(C_{\text{gs}}/\epsilon_{\text{trrot}})^{-1/p})$. Under the constraint of Eq. (B1), this gate count is minimized when $\epsilon_{\text{qpe}} = \epsilon\sqrt{\frac{p}{1+p}}$, which corresponds to the optimal Trotter step size:

$$\delta = \left(\frac{\epsilon}{C_{\text{gs}}}\right)^{\frac{1}{p}} \left(\frac{1}{1+p}\right)^{\frac{1}{2p}}. \quad (\text{B2})$$

As mentioned in Sec. II B 1, we determine the Trotter constant $C_{\text{gs}} = C_{\text{gs}}(p, \{\hat{H}_\ell\})$ using the heuristic estimate from Ref. [41], which shows a strong correlation between C_{gs} and the Hamiltonian's ℓ_1 -norm, λ . Specifically, for second-order Trotterization ($p = 2$), numerical results in Ref. [41] indicate an approximate scaling of $C_{\text{gs}} \simeq a\lambda^b$ with $a \simeq 3.41 \times 10^{-5}$ and $b \simeq 2.09$.

In the partially randomized RPE framework, the Hamiltonian \hat{H} is decomposed into a deterministic part \hat{H}_D and a randomized part \hat{H}_R , as in Eq. (14). In the m -th round of RPE, the evolution corresponding to \hat{H}_R within the full Trotterized unitary $(\hat{S}_p(\delta))^{2^m}$ is implemented using a randomized product formula. The resulting gate count in the m -th round, G_m , is given by [41]:

$$G_m = G_m^{(\text{det})} + G_m^{(\text{rand})}, \quad (\text{B3})$$

$$G_m^{(\text{det})} = \frac{1}{2} C_{\text{gate}} N_{\text{stage}} 2^m L_D =: g_m^{(\text{det})} L_D, \quad (\text{B4})$$

$$G_m^{(\text{rand})} = C_{\text{gate}} \gamma \delta^2 2^{2m} \lambda_R^2 =: g_m^{(\text{rand})} \lambda_R^2, \quad (\text{B5})$$

where $G_m^{(\text{det})}$ and $G_m^{(\text{rand})}$ are the gate counts for the deterministic and randomized contributions, respectively. Here, N_{stage} is the number of stages in the symmetric decomposition, e.g., $N_{\text{stage}} = 2 \cdot 5^{k-1}$ for a $2k$ -th order Suzuki-Trotter product formula. The factor of 1/2 in Eq. (B4) arises from the ‘‘halving trick’’ applicable to the Hadamard test for symmetric Suzuki-Trotter product formulas [20, 41]. The constant γ depends on the chosen randomized protocol: $\gamma = 1$ for qDRIFT and $\gamma = 2$ for RTE [41], and $\gamma = 2$ for TE-PAI [77]. In Eqs. (B4) and (B5), C_{gate} is a factor that converts the number of Pauli rotation gates into the number of elementary gates for a specific hardware architecture. For the STAR architecture considered in this work, we set $C_{\text{gate}} = 1$, as single-qubit Pauli rotations are native elementary gates [29, 30].

Appendix C: Spin-extended BLISS transformation

In this Appendix, we detail the extension of the BLISS transformation to incorporate spin symmetries. As explained in Sec. III B 2, the BLISS transformation is conventionally formulated for particle-number symmetry only [35, 36]. However, the framework can be extended to other symmetries, such as spin and spatial symmetries, a possibility mentioned in the original proposal [35]. If the target eigenstate $|\psi_k\rangle$ is known to be an eigenstate of a set of symmetry operators $\{\hat{Q}_i\}$ with eigenvalues $\{Q_i\}$, such that $\hat{Q}_i|\psi_k\rangle = Q_i|\psi_k\rangle$, a corresponding BLISS transformation can be systematically constructed as $\hat{H}' = \hat{H} - \hat{O}_i(\hat{Q}_i - Q_i)$, where \hat{O}_i is an arbitrary Hermitian operator that commutes with \hat{Q}_i . A key constraint for this construction, imposed to simplify subsequent optimization, is that the BLISS operator $\hat{O}_i(\hat{Q}_i - Q_i)$ must have the same polynomial degree in its fermionic operator expansion as the original Hamiltonian \hat{H} [35].

For molecular electronic structure Hamiltonians, the relevant symmetries are the conserved total electron number $\hat{N}_e = \sum_{p\sigma} \hat{a}_{p\sigma}^\dagger \hat{a}_{p\sigma}$, the spin projection \hat{S}_z , and the total spin \hat{S}^2 . Note that the chemically complex molecules considered in this work generally do not exhibit spatial point-group symmetries. The total spin operator \hat{S}^2 , however, presents a challenge. These spin operators

are defined as

$$\hat{S}_z := \frac{1}{2} \sum_{p,\sigma} \sigma \hat{a}_{p\sigma}^\dagger \hat{a}_{p\sigma}, \quad (\text{C1})$$

$$\hat{S}^2 := \hat{S}_+ \hat{S}_- + \hat{S}_z(\hat{S}_z - 1), \quad (\text{C2})$$

where $\hat{S}_+ := \sum_p \hat{a}_{p\uparrow}^\dagger \hat{a}_{p\downarrow}$ and $\hat{S}_- := \sum_p \hat{a}_{p\downarrow}^\dagger \hat{a}_{p\uparrow}$, involves spin-flipping terms. We define a spin variable σ such that an up-spin (\uparrow) corresponds to $\sigma = +1$ and a down-spin (\downarrow) corresponds to $\sigma = -1$. In this context, σ effectively acts as a sign function for the spin state. The off-diagonal part $\hat{S}_+ \hat{S}_- = \sum_{pq} \hat{a}_{p\uparrow}^\dagger \hat{a}_{p\downarrow} \hat{a}_{q\downarrow}^\dagger \hat{a}_{q\uparrow}$ introduces four-fermion operators with mixed spin indices that are absent in the original electronic structure Hamiltonian (19). Consequently, a BLISS transformation based on \hat{S}^2 would introduce new Pauli strings not present in \hat{H} , increasing the Hamiltonian's ℓ_1 -norm and, therefore, the simulation cost. To maintain or reduce the gate count, as is the goal of UWC, we thus exclude the \hat{S}^2 symmetry from our BLISS construction.

To incorporate the \hat{S}_z symmetry into the BLISS framework, we first express the electronic structure Hamiltonian in a spin-explicit representation:

$$\begin{aligned} \hat{H} &= \sum_{pq} \sum_{\sigma} h_{pq}^{(\sigma)} \hat{a}_{p\sigma}^\dagger \hat{a}_{q\sigma} + \frac{1}{2} \sum_{pqrs} \sum_{\sigma\tau} g_{pqrs}^{(\sigma\tau)} \hat{a}_{p\sigma}^\dagger \hat{a}_{r\tau}^\dagger \hat{a}_{s\tau} \hat{a}_{q\sigma} \\ &=: \sum_{pq} \sum_{\sigma} k_{pq}^{(\sigma)} \hat{f}_{pq}^{(\sigma)} + \frac{1}{2} \sum_{pqrs} \sum_{\sigma\tau} g_{pqrs}^{(\sigma\tau)} \hat{f}_{pq}^{(\sigma)} \hat{f}_{rs}^{(\tau)}, \quad (\text{C3}) \end{aligned}$$

where $\hat{f}_{pq}^{(\sigma)} := \hat{a}_{p\sigma}^\dagger \hat{a}_{q\sigma}$ and $k_{pq}^{(\sigma)} := h_{pq}^{(\sigma)} - \frac{1}{2} \sum_r g_{prrq}^{(\sigma\sigma)}$. This representation reduces to the conventional form in Eq. (19) under the assumption that $h_{pq} = h_{pq}^{(\uparrow)} = h_{pq}^{(\downarrow)}$ and $g_{pqrs} = g_{pqrs}^{(\uparrow\uparrow)} = g_{pqrs}^{(\downarrow\downarrow)} = g_{pqrs}^{(\uparrow\downarrow)} = g_{pqrs}^{(\downarrow\uparrow)}$. Analogous to the derivation leading to Eq. (20), the corresponding Majorana representation is obtained as

$$\hat{H} = \frac{i}{2} \sum_{pq,\sigma} \left(k_{pq}^{(\sigma)} + \frac{1}{2} \sum_{r,\tau} g_{pqrr}^{(\sigma\tau)} \right) \hat{\gamma}_{p\sigma} \hat{\gamma}_{q\sigma} + \frac{1}{4} \sum_{p>r,s>q} \sum_{\sigma} (g_{pqrs}^{(\sigma\sigma)} - g_{psrq}^{(\sigma\sigma)}) \hat{\gamma}_{p\sigma} \hat{\gamma}_{r\sigma} \hat{\gamma}_{q\sigma} \hat{\gamma}_{s\sigma} + \frac{1}{4} \sum_{pqrs} g_{pqrs}^{(\uparrow\downarrow)} \hat{\gamma}_{p\uparrow} \hat{\gamma}_{r\downarrow} \hat{\gamma}_{q\uparrow} \hat{\gamma}_{s\downarrow} + \text{const.} \quad (\text{C4})$$

Using this spin-explicit representation, we can now define a BLISS operator that incorporates both particle-number and spin-projection symmetries. For a target eigenstate $|\psi_k\rangle$ with well-defined quantum numbers N_e and S_z , such that $\hat{N}_e|\psi_k\rangle = N_e|\psi_k\rangle$ and $\hat{S}_z|\psi_k\rangle = S_z|\psi_k\rangle$, the spin-extended BLISS operator is defined as

$$\begin{aligned} \hat{T}_S(\vec{\nu}, \vec{\zeta}) &:= \nu_1 (\hat{S}_z - S_z) + \nu_2 \left(\left(\hat{S}_z^2 - \frac{1}{4} \hat{N}_e \right) - \left(S_z^2 - \frac{1}{4} N_e \right) \right) + \nu_3 \left(\hat{S}_z (\hat{N}_e - 1) - S_z (N_e - 1) \right) \\ &+ \sum_{pq} \zeta_{pq}^{(1)} \hat{F}_{pq} (\hat{S}_z - S_z) + \sum_{pq} \zeta_{pq}^{(2)} \hat{F}_{pq}^{(z)} (\hat{N}_e - N_e) + \sum_{pq} \zeta_{pq}^{(3)} \hat{F}_{pq}^{(z)} (\hat{S}_z - S_z), \quad (\text{C5}) \end{aligned}$$

where $\nu_i, \zeta_{pq}^{(j)} \in \mathbb{R}$ with $\zeta_{pq}^{(j)} = \zeta_{qp}^{(j)}$, and $\hat{F}_{pq} := \sum_{\sigma} \hat{f}_{pq}^{(\sigma)}$ and $\hat{F}_{pq}^{(z)} := \sum_{\sigma} \sigma \hat{f}_{pq}^{(\sigma)}$. The parameters are denoted as $\vec{\nu} = \{\nu_1, \nu_2, \nu_3\}$ and $\vec{\zeta} = \{\zeta_{pq}^{(j)} \mid p \leq q; j = 1, 2, 3\}$, leading to $3 + \frac{3}{2}N(N-1)$ independent parameters in total. Each term in Eq. (C5) is constructed to be a quadratic or quartic fermionic operator, thereby matching the polynomial

degree of the electronic Hamiltonian. Specifically, the terms associated with ν_2 and ν_3 are quartic operators:

$$\hat{S}_z^2 - \frac{1}{4}\hat{N}_e = \frac{1}{4} \sum_{pqrs} \sum_{\sigma\tau} \sigma\tau \delta_{pq} \delta_{rs} \hat{a}_{p\sigma}^\dagger \hat{a}_{r\tau}^\dagger \hat{a}_{s\tau} \hat{a}_{q\sigma}, \quad (\text{C6})$$

$$\hat{N}_e \hat{S}_z - \hat{S}_z = \frac{1}{4} \sum_{pqrs} \sum_{\sigma\tau} (\sigma + \tau) \delta_{pq} \delta_{rs} \hat{a}_{p\sigma}^\dagger \hat{a}_{r\tau}^\dagger \hat{a}_{s\tau} \hat{a}_{q\sigma}, \quad (\text{C7})$$

These expressions are consistent with the fermionic representation in Eq. (C3). The spin-extended BLISS transformation is then defined by $\hat{H}'(\vec{\nu}, \vec{\zeta}) := \hat{H} - \hat{T}_S(\vec{\nu}, \vec{\zeta})$, yielding a transformed Hamiltonian

$$\hat{H}'(\vec{\nu}, \vec{\zeta}) := \hat{H} - \hat{T}_S(\vec{\nu}, \vec{\zeta}) = \sum_{pq} \sum_{\sigma} k_{pq}^{(\sigma)'}(\vec{\nu}, \vec{\zeta}) \hat{f}_{pq}^{(\sigma)} + \frac{1}{2} \sum_{pqrs} \sum_{\sigma\tau} g_{pqrs}^{(\sigma\tau)'}(\vec{\nu}, \vec{\zeta}) \hat{f}_{pq}^{(\sigma)} \hat{f}_{rs}^{(\tau)}, \quad (\text{C8})$$

with the transformed one- and two-electron integrals

$$h_{pq}^{(\sigma)'}(\vec{\nu}, \vec{\zeta}) = h_{pq}^{(\sigma)} - \frac{1}{2} \nu_1 \sigma \delta_{pq} + \left(S_z - \frac{1}{2} \sigma \right) \zeta_{pq}^{(1)} + \sigma (N_e - 1) \zeta_{pq}^{(2)} + \left(\sigma S_z - \frac{1}{2} \right) \zeta_{pq}^{(3)}, \quad (\text{C9})$$

$$g_{pqrs}^{(\sigma\tau)'}(\vec{\nu}, \vec{\zeta}) = g_{pqrs}^{(\sigma\tau)} - \frac{1}{2} [\nu_2 \sigma\tau + \nu_3 (\sigma + \tau)] \delta_{pq} \delta_{rs} - \frac{1}{2} [\tau \zeta_{pq}^{(1)} \delta_{rs} + \sigma \zeta_{rs}^{(1)} \delta_{pq}] - [\sigma \zeta_{pq}^{(2)} \delta_{rs} + \tau \zeta_{rs}^{(2)} \delta_{pq}] - \frac{1}{2} \sigma\tau [\zeta_{pq}^{(3)} \delta_{rs} + \zeta_{rs}^{(3)} \delta_{pq}], \quad (\text{C10})$$

and $k_{pq}^{(\sigma)'}(\vec{\nu}, \vec{\zeta}) := h_{pq}^{(\sigma)'}(\vec{\nu}, \vec{\zeta}) - \frac{1}{2} \sum_r g_{prrq}^{(\sigma\sigma)'}(\vec{\nu}, \vec{\zeta})$.

In the UWC optimization detailed in Appendix D, we implemented this spin-extended BLISS transformation alongside both orbital optimization and the conventional particle-number BLISS. For the systems studied, the additional resource reduction from spin-extended BLISS was typically negligible compared to that from conventional BLISS alone, a finding consistent with previous works [35, 36]. Nevertheless, we included it in our analysis for all molecules to ensure our resource estimates are as accurate as possible, capturing even minor constant-factor improvements.

Appendix D: Details of the UWC optimization

In this Appendix, we provide the technical details of the UWC optimization introduced in Sec. III C. We also describe the computational methods used to obtain the numerical results presented in Sec. IV and V.

1. Iterative optimization procedure

First, we detail the iterative UWC optimization procedure employed in this work. As outlined in Sec. III C, our approach combines OO and BLISS transformations within a sequential, iterative framework. The precise procedure is summarized in Algorithm 2.

The optimization begins with an *orbital initialization* step. Since a sparse Hamiltonian representation often corresponds to a small ℓ_1 -norm, a good initial guess for

the UWC optimization is a basis that minimizes this norm. To find such a basis, we compare the initial canonical molecular orbital basis with a set of alternative bases derived from a *double factorization* procedure, which we term the *Cholesky orbital bases* [59]. This procedure involves first performing a Cholesky decomposition of the two-electron integral tensor g_{pqrs} , viewed as an $N^2 \times N^2$ positive-semidefinite matrix:

$$g_{pqrs} = \sum_{t=1}^{N_{\text{DF}}} L_{pq}^{(t)} (L_{rs}^{(t)})^\dagger, \quad (\text{D1})$$

where $N_{\text{DF}} \leq N^2$ and each $L^{(t)}$ is a real symmetric $N \times N$ matrix. A second factorization is then performed via eigenvalue decomposition of each Cholesky vector $L^{(t)}$:

$$L_{pq}^{(t)} = \sum_{i=1}^N U_{pi}^{(t)} W_i^{(t)} U_{qi}^{(t)}, \quad (\text{D2})$$

where $W_i^{(t)}$ are the real-valued eigenvalues and $U^{(t)}$ are the $N \times N$ unitary matrices of eigenvectors. We compute the ℓ_1 -norm for the Hamiltonian expressed in the canonical basis and in each of these Cholesky bases, selecting the one with the smallest ℓ_1 -norm as the starting point, \hat{H} , for the main optimization loop. This choice was motivated by our observation, consistent with Ref. [41], that rotation to a Cholesky orbital basis often reduces the ℓ_1 -norm.

Following initialization, we evaluate the initial gate cost G_M using the discrete cost function (Eq. (17)) and enter the main iterative loop. In each iteration, we first determine the optimal partitioning boundary

Algorithm 2 Iterative UWC optimization procedure.

```

1: Input: Initial Hamiltonian  $\hat{H}_{\text{init}}$ , target electron number  $N_e$ , target spin projection  $S_z$ .
2: Parameters: Convergence threshold  $\delta_{\text{th}}$ , max iterations  $N_{\text{iter}}$ .
   Orbital Initialization
3: Generate a set of Cholesky orbital basis representations for  $\hat{H}_{\text{init}}$ .
4: Select the representation with the minimum  $\ell_1$ -norm as the starting Hamiltonian,  $\hat{H}$ .
   Initial Cost Evaluation
5: Calculate the initial gate cost  $G_M$  for  $\hat{H}$  using Eq. (17).
6:  $G_{\text{prev}} \leftarrow G_M$ 
7:  $\hat{H}_{\text{best}} \leftarrow \hat{H}$ 
   Main Optimization Loop
8: for  $n = 1, 2, \dots, N_{\text{iter}}$  do
9:   Determine the optimal partition  $L_D^*$  and weight parameter  $w_{\text{soft}}$  for  $\hat{H}$ , according to Eqs. (37) and (36).
10:   $\vec{\kappa}^* \leftarrow \arg \min_{\vec{\kappa}} G_{\text{soft}}(\hat{H}(\vec{\kappa}))$ 
11:   $\hat{H}_{\text{OO}} \leftarrow \hat{H}(\vec{\kappa}^*)$ 
12:   $(\vec{\mu}^*, \vec{\xi}^*) \leftarrow \arg \min_{(\vec{\mu}, \vec{\xi})} G_{\text{soft}}(\hat{H}_{\text{OO}}(\vec{\mu}, \vec{\xi}))$ 
13:   $\hat{H}_{\text{BLISS}} \leftarrow \hat{H}_{\text{OO}}(\vec{\mu}^*, \vec{\xi}^*)$ 
14:   $(\vec{\nu}^*, \vec{\zeta}^*) \leftarrow \arg \min_{(\vec{\nu}, \vec{\zeta})} G_{\text{soft}}(\hat{H}_{\text{BLISS}}(\vec{\nu}, \vec{\zeta}))$ 
15:   $\hat{H}_{\text{next}} \leftarrow \hat{H}_{\text{BLISS}}(\vec{\nu}^*, \vec{\zeta}^*)$ 
   Convergence and Degradation Check
16:   Calculate the discrete gate cost  $G_{\text{next}}$  for  $\hat{H}_{\text{next}}$ .
17:   if  $|G_{\text{next}} - G_{\text{prev}}|/|G_{\text{prev}}| < \delta_{\text{th}}$  then
18:      $\hat{H}_{\text{best}} \leftarrow \hat{H}_{\text{next}}$ 
19:     terminate loop ▷ Converged
20:   else if  $G_{\text{next}} > G_{\text{prev}}$  then
21:     terminate loop ▷ Cost increased, discard result
    and terminate
22:   end if
   Update for Next Iteration
23:    $\hat{H} \leftarrow \hat{H}_{\text{next}}$ 
24:    $G_{\text{prev}} \leftarrow G_{\text{next}}$ 
25:    $\hat{H}_{\text{best}} \leftarrow \hat{H}_{\text{next}}$ 
26: end for
27: Output: The UWC-optimized Hamiltonian representation  $\hat{H}_{\text{best}}$ .

```

L_D^* (Eq. (37)) and the corresponding soft-gate-cost hyperparameter w_{soft} (Eq. (36)) for the current Hamiltonian representation \hat{H} . We then minimize the soft-gate cost function G_{soft} (Eq. (35)) by applying a sequence of transformations: first OO, then the standard particle-number BLISS, and finally the spin-extended BLISS (Appendix C). This specific order was chosen based on empirical tests showing that performing OO first consistently yielded the best results.

After completing this sequence, we obtain the optimized Hamiltonian for the current iteration, \hat{H}_{next} , and evaluate its true cost by calculating the discrete gate count, G_{next} . This cost is then compared to the cost from the previous iteration, G_{prev} . The iterative process is terminated under two conditions: (1) if the relative

improvement in cost is below a threshold δ_{th} (convergence), or (2) if the cost has increased ($G_{\text{next}} > G_{\text{prev}}$). If the cost increased, the results of the current iteration are discarded, and the optimization stops. If neither termination condition is met, the procedure continues to the next iteration, using the newly improved Hamiltonian \hat{H}_{next} as the starting point. The final output is the best Hamiltonian representation found before the loop terminated.

2. Computational details

Here, we specify the computational settings used to obtain the UWC-optimized Hamiltonians for the numerical results in Sec. IV and V.

To generate the Cholesky orbital basis representations, we employed the double factorization functionality implemented in the `ffsim` library [105]. The subsequent OO and BLISS optimizations were performed using the sequential least squares programming (SLSQP) optimizer available in the `SciPy` package [106]. The choice of SLSQP was motivated by the nature of our soft-gate cost function, G_{soft} (Eq. (35)). This function includes an absolute value term $|c_{L_D}|$, which makes its gradient discontinuous. We empirically observed that optimizers reliant on continuous gradients, such as L-BFGS-B, often failed to minimize G_{soft} effectively. To accelerate the optimization, all gradients were computed using automatic differentiation via the `JAX` library [107]. We also found that the raw values of G_{soft} and its gradients could become very large, leading to numerical instability in the optimization process. This issue was mitigated by rescaling the cost function by the initial gate cost G_M for the starting Hamiltonian \hat{H} .

The sigmoid regularization parameter ϵ_{soft} in Eq. (35) was set to 10^{-4} for the majority of calculations. This value was empirically determined to provide a robust balance between two competing requirements: (1) ensuring that the soft cost G_{soft} is a faithful approximation of the discrete gate count G_M , and (2) maintaining numerical stability for the gradient-based optimization. A value of ϵ_{soft} that is too large would cause the sigmoid to deviate significantly from a step function, hindering effective gate count minimization. Conversely, a value that is too small makes the cost function landscape overly sharp and numerically ill-conditioned, with exploding gradients that derail the optimization. We observed this failure mode consistently across all molecular systems when ϵ_{soft} was set to 10^{-5} . While $\epsilon_{\text{soft}} = 10^{-4}$ provided a reliable and broadly applicable default choice, we found that for certain smaller-scale models—particularly those with a small number of Hamiltonian coefficients—slightly larger values of ϵ_{soft} (e.g., $\epsilon_{\text{soft}} = 10^{-3}$) could yield marginally improved optimization performance. Unless otherwise noted, however, almost all reported results employ $\epsilon_{\text{soft}} = 10^{-4}$. Detailed instance-specific choices are provided in the supplementary data repository associated

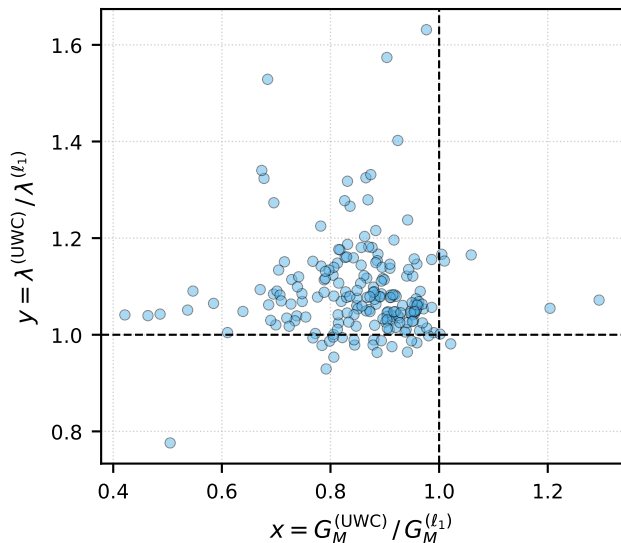


FIG. 8. Performance comparison of UWC and ℓ_1 -norm optimization for all benchmark molecules. The plot compares the final ℓ_1 -norm (λ) and maximum gate count (G_M) from the two methods. The vertical axis shows the ratio $\lambda^{(\text{UWC})}/\lambda^{(\ell_1)}$, while the horizontal axis shows the ratio $G_M^{(\text{UWC})}/G_M^{(\ell_1)}$. Points to the left of the vertical dashed line ($x = 1$) indicate that UWC achieved a lower gate count, the primary optimization target.

with this work [104].

For all numerical results presented, the UWC optimization (Algorithm 2) was executed with a maximum of $N_{\text{iter}} = 10$ iterations and a convergence threshold of $\delta_{\text{th}} = 0.1\%$. While these strict criteria ensure thorough optimization, we note for practical purposes that they could likely be relaxed. Empirically, we consistently observed that the majority of the cost reduction occurred during the first iteration, with subsequent iterations providing only minor refinements.

3. Comparison of UWC and ℓ_1 -norm optimization

As discussed in Sec. III C, minimizing the Hamiltonian’s ℓ_1 -norm, λ , is a common heuristic for reducing quantum simulation costs. This principle, borrowed from machine learning’s ℓ_1 -norm regularization, promotes a sparse coefficient distribution. This sparsity is expected to reduce the gate count in partially randomized algorithms, making the ℓ_1 -norm a valuable proxy for the true computational cost. Here, we directly compare the performance of this heuristic approach against our proposed UWC method, which targets the gate count itself.

To perform this comparison, we applied the ℓ_1 -norm optimization procedure, incorporating OO, conventional BLISS, and spin-extended BLISS, to all benchmark systems (see Appendix E 1). The main difference between the two approaches was the cost function driving the opti-

mization: the UWC method used the soft-gate cost G_{soft} , while the ℓ_1 -norm optimization method used the ℓ_1 -norm λ directly.

The results are summarized in Fig. 8. As expected, directly optimizing the ℓ_1 -norm consistently yields a lower value of λ (most points are above the $y = 1$ line). Conversely, our UWC method consistently achieves a lower gate count G_M (almost all points are to the left of the $x = 1$ line). While the resulting Hamiltonian representations from both methods are often similar, the direct optimization of the gate count leads to significant practical advantages. This is highlighted by cases where UWC achieves a gate count reduction of up to 60% compared to ℓ_1 -norm optimization. Since the total simulation runtime is directly proportional to this gate count, this translates to a commensurate reduction in the overall computational time. Therefore, when the primary goal is to minimize the runtime of partially randomized Hamiltonian simulation, UWC is demonstrably superior to using the ℓ_1 -norm as a proxy.

Appendix E: Detailed resource estimation data for molecular models

In this Appendix, we provide comprehensive resource estimation data for all molecular models investigated in this work. The results presented in Sec. IV and Sec. V are derived from and substantiated by the detailed information compiled within this Appendix.

1. Details of molecular models

This section provides essential information for the molecular active-space models investigated in this work. We focus on four distinct families: hydrogen chains, iron-sulfur clusters (including FeMoco), cytochrome P450 active sites, and ruthenium-based catalysts for CO_2 utilization. All Hamiltonian data were sourced from publicly available datasets accompanying the relevant literature [19, 20, 22, 34, 50, 51, 108].

The pertinent details for each molecular family, including the number of orbitals, number of electrons, and Hilbert space dimension, are summarized in Tables V (hydrogen chain models), VI (iron-sulfur clusters), VII (cytochrome P450 active-site models), and VIII (ruthenium-based catalyst series). For consistency, each table includes columns for

- **“Molecule ID”**: Identifier for specific molecular active-space models.
- **“Orbitals”**: Number of spatial orbitals, N .
- **“Electrons”**: Number of spin-up and spin-down electrons, $(N_{\uparrow}, N_{\downarrow})$.
- **“Hilbert space dimension”**: Dimension of the Hilbert space calculated as $\binom{N}{N_{\uparrow}} \binom{N}{N_{\downarrow}}$.

TABLE V. Summary of molecular active-space models for hydrogen chain models. H_x identifies a linear hydrogen chain model with x hydrogen atoms. The Hamiltonian data for these models were obtained from a publicly available Zenodo repository [109] associated with Ref. [23].

Molecule ID	Orbitals	Electrons (N_\uparrow, N_\downarrow)	Hilbert space dimension
H_{10}	10	(5, 5)	6.35×10^4
H_{20}	20	(10, 10)	3.41×10^{10}
H_{30}	30	(15, 15)	2.41×10^{16}
H_{40}	40	(20, 20)	1.90×10^{22}
H_{50}	50	(25, 25)	1.60×10^{28}

TABLE VI. Summary of molecular active-space models for iron-sulfur clusters. The Hamiltonian data for $[2\text{Fe-2S}]^{-2}$, $[2\text{Fe-2S}]^{-3}$, $[4\text{Fe-4S}]$, and $[4\text{Fe-4S}]^{-2}$ were retrieved from a publicly available Zenodo repository [110] associated with Ref. [34]. FeMoco (Sm) and FeMoco (Lg) denote the smaller 54-orbital and larger 76-orbital models for FeMoco, respectively, derived in Refs. [20] and [108]. The Hamiltonian data for these FeMoco models were obtained from a separate publicly available Zenodo repository [109] linked to Ref. [23].

Molecule ID	Orbitals	Electrons (N_\uparrow, N_\downarrow)	Hilbert space dimension
$[2\text{Fe-2S}]^{-3}$	20	(16, 15)	7.51×10^7
$[2\text{Fe-2S}]^{-2}$	20	(15, 15)	2.40×10^8
$[4\text{Fe-4S}]^{-2}$	36	(27, 27)	8.86×10^{15}
$[4\text{Fe-4S}]$	36	(26, 26)	6.46×10^{16}
FeMoco (Sm)	54	(27, 27)	3.79×10^{30}
FeMoco (Lg)	76	(58, 55)	3.64×10^{35}

Specific naming conventions and data sources for each model are elaborated within the respective table captions.

It is important to note that the number of orbitals in a model can vary even for the same molecule, depending on the chosen active space. Such variations are distinguished by identifiers in parentheses, for example, FeMoco (Sm) and FeMoco (Lg) denote smaller and larger active-space models for FeMoco, respectively.

2. Full list of resource estimates

This section summarizes the logical and physical resource estimates for all molecular active-space models introduced previously. These estimates specifically pertain to partially randomized RPE under the UWC-optimized Hamiltonian representation. The calculations are performed for three different control parameters: $\xi = 0.1$, $\xi = 0.05$, and $\xi = 0.01$. It is important to note that the UWC-optimized Hamiltonian representation is distinct for each ξ value. Furthermore, the partially randomized circuits are assumed to comprise deterministic second-order Trotterization and randomized qDRIFT

TABLE VII. Summary of molecular active-space models for the cytochrome P450 active site. The Hamiltonian data for these models were obtained from a publicly available Zenodo repository [111] associated with Ref. [51]. The Molecule IDs ‘‘Cpd I’’, ‘‘water’’, ‘‘inhibited’’, and ‘‘empty’’ denote the Compound I intermediate and various ligand-bound or empty states in the P450 catalytic cycle, as described in Ref. [51]. The active space labels A-G-X follow a hierarchical construction introduced in Ref. [51], where orbitals are progressively added based on their relevance to spin character, ligand binding, and spatial proximity to the iron center: ‘A’: Five open-shell orbitals crucial for spin character; ‘B’: Adds iron 3d/4s and iron-nitrogen antibonding orbitals; ‘C’: Further includes iron 4p/d’ and iron-axial ligand bonding/antibonding orbitals; ‘D’: Incorporates spatially closest iron-nitrogen σ orbitals; ‘E’: Adds heme π orbitals on nitrogen atoms; ‘F’: Adds heme π orbitals on carbon atoms; ‘G’: Includes distal carbon-sulfur bonding/antibonding orbitals; ‘X’: Finally adds less-important heme carbon-nitrogen σ orbitals.

Molecule ID	Orbitals	Electrons (N_\uparrow, N_\downarrow)	Hilbert space dimension
(a) Compound I (Cpd I)			
P450-Cpd I (A)	5	(5, 0)	1.00×10^0
P450-Cpd I (B)	8	(8, 3)	5.60×10^1
P450-Cpd I (C)	15	(11, 6)	6.83×10^6
P450-Cpd I (D)	23	(15, 10)	5.61×10^{11}
P450-Cpd I (E)	31	(19, 14)	3.74×10^{16}
P450-Cpd I (F)	41	(25, 20)	2.77×10^{22}
P450-Cpd I (G)	43	(26, 21)	4.43×10^{23}
P450-Cpd I (X)	58	(34, 29)	3.86×10^{32}
(b) Resting state with water bound to heme			
P450-rest (A)	5	(5, 0)	1.00×10^0
P450-rest (B)	8	(7, 2)	2.24×10^2
P450-rest (C)	13	(10, 5)	3.68×10^5
P450-rest (D)	20	(14, 9)	6.51×10^9
P450-rest (E)	28	(18, 13)	4.91×10^{14}
P450-rest (F)	40	(24, 19)	8.25×10^{21}
P450-rest (G)	42	(25, 20)	1.31×10^{23}
P450-rest (X)	56	(33, 28)	2.42×10^{31}
(c) Pyridine inhibitor bound model complex			
P450-inhibited (A)	5	(5, 0)	1.00×10^0
P450-inhibited (B)	9	(8, 3)	7.56×10^2
P450-inhibited (C)	14	(11, 6)	1.09×10^6
P450-inhibited (D)	21	(15, 10)	1.91×10^{10}
P450-inhibited (E)	32	(20, 15)	1.28×10^{17}
P450-inhibited (F)	44	(27, 22)	1.44×10^{24}
P450-inhibited (G)	46	(28, 23)	2.32×10^{25}
P450-inhibited (X)	60	(36, 31)	4.13×10^{33}
(d) Pentacoordinated empty state with no ligands			
P450-empty (A)	5	(5, 0)	1.00×10^0
P450-empty (B)	8	(7, 2)	2.24×10^2
P450-empty (C)	11	(9, 4)	1.82×10^4
P450-empty (D)	18	(13, 8)	3.75×10^8
P450-empty (E)	26	(17, 12)	3.02×10^{13}
P450-empty (F)	37	(22, 17)	1.49×10^{20}
P450-empty (G)	39	(23, 18)	2.35×10^{21}
P450-empty (X)	55	(31, 26)	8.86×10^{30}

TABLE VIII. Summary of molecular active-space models for ruthenium-based catalysts used in CO₂ utilization. The Hamiltonian data for these models were retrieved from a publicly available Zenodo repository [112], associated with Ref. [22]. The numerical labels in the Molecule IDs (i.e., I, II, II-III, V, VIII, VIII-IX, IX, and XVIII) correspond to specific intermediate and transition state structures within the catalytic cycle, as detailed in Ref. [22]. The active space labels ‘Sm’, ‘Md’, and ‘Lg’ denote a hierarchical construction introduced in Ref. [22], where orbitals are progressively added based on their electronic correlation and chemical relevance: ‘Sm’ represents a small active space constructed from orbitals selected via an entanglement criterion; ‘Md’ designates a middle-sized active space, adding valence orbitals of ruthenium/ligands and ligand-metal bonding orbitals; ‘Lg’ refers to a large active space, further incorporating additional π/π^* orbitals on the triphos ligand.

Molecule ID	Orbitals	Electrons ($N_{\uparrow}, N_{\downarrow}$)	Hilbert space dimension
(a) Stable intermediate I			
Ru-I (Sm)	5	(2, 2)	1.00×10^2
Ru-I (Md)	16	(7, 7)	1.31×10^8
Ru-I (Lg)	52	(24, 24)	1.82×10^{29}
(b) Stable intermediate II			
Ru-II (Sm)	6	(4, 4)	2.25×10^2
Ru-II (Md)	26	(17, 17)	9.76×10^{12}
Ru-II (Lg)	62	(35, 35)	7.82×10^{34}
(c) Transition state II-III			
Ru-II-III (Sm)	6	(4, 4)	2.25×10^2
Ru-II-III (Md)	29	(19, 19)	4.01×10^{14}
Ru-II-III (Lg)	65	(37, 37)	3.86×10^{36}
(e) Stable intermediate V			
Ru-V (Sm)	11	(6, 6)	2.13×10^5
Ru-V (Md)	24	(16, 16)	5.41×10^{11}
Ru-V (Lg)	60	(34, 34)	4.88×10^{33}
(f) Stable intermediate VIII			
Ru-VIII (Sm)	2	(1, 1)	4.00×10^0
Ru-VIII (Md)	29	(20, 20)	1.00×10^{14}
Ru-VIII (Lg)	65	(38, 38)	2.10×10^{36}
(g) Transition state VIII-IX			
Ru-VIII-IX (Sm)	4	(2, 2)	3.60×10^1
Ru-VIII-IX (Md)	23	(18, 18)	1.13×10^9
Ru-VIII-IX (Lg)	59	(36, 36)	2.08×10^{32}
(d) Stable intermediate IX			
Ru-IX (Sm)	16	(8, 8)	1.66×10^8
Ru-IX (Md)	26	(16, 16)	2.82×10^{13}
Ru-IX (Lg)	62	(34, 34)	1.22×10^{35}
(h) Stable intermediate XVIII			
Ru-XVIII (Sm)	4	(2, 2)	3.60×10^1
Ru-XVIII (Md)	20	(14, 14)	1.50×10^9
Ru-XVIII (Lg)	56	(32, 32)	1.90×10^{31}

parts. For all resource estimates, a realistic physical error rate of $p_{\text{ph}} = 10^{-3}$ and the chemical accuracy target $\epsilon = 1.6 \times 10^{-3}$ are adopted.

a. Logical resource estimates

Logical resource estimates, encompassing information on the UWC-optimized Hamiltonian representations, logical circuits for RPE, and partial fault tolerance based on the SMM protocol, are detailed in Tables IX (hydrogen chain models), X (iron-sulfur clusters), XI, XII (cytochrome P450 active-site models), and XIII, XIV (ruthenium-based catalyst series). For consistency, each table features “Hamiltonian”, “Logical circuit”, and “Error correction” sections.

- The **“Hamiltonian”** columns report the number of deterministically treated terms (L_D), the total weight for the randomized part (λ_R), and the ℓ_1 -norm (λ). L_D and λ_R represent the optimal values for the last round $m = M$, chosen to minimize the gate count as defined in Eq. (17).
- The **“Logical circuit”** columns provide the number of logical data qubits ($N_L = 2N + 1$) and the maximum gate count (G_M) at the last round, also obtained from Eq. (17).
- The **“Error correction”** columns detail the partially fault-tolerant setup for the last round $m = M$, including the selected SMM priority (“accuracy” or “speed” prioritized setting in Appendix F), the code distance (d), the average rotation angle ($\bar{\theta}_L$) within the partially randomized circuit, and the total logical error rate (P_{total}).

The partially randomized circuit consists of second-order Trotterization and qDRIFT. The deterministic component involves Pauli rotations with angles $\{c_{\ell} \frac{\delta}{2}\}_{\ell=1, \dots, L_D}$, where δ is the Trotterization step size (Eq. (B2)). The randomized part uses Pauli rotation gates with a fixed angle $\arctan(1/(2\lambda_R \delta 2^m))$ for the m -th round [41, 72]. Using this information alongside the angular dependence of $\alpha_{\text{RUS}}(\theta_L)$ and $C_{\text{smm}}(\theta_L)$, determined from Fig. 9, the values of d and P_{total} are derived according to the procedure outlined in Sec. VB.

b. Physical resource estimates

Physical resource estimates, derived from the logical resource estimates, are summarized in Tables XV (hydrogen chain models), XVI (iron-sulfur clusters), XVII, XVIII (cytochrome P450 active-site models), and XIX, XX (ruthenium-based catalyst series). For consistency, each table presents columns for:

- **“Physical qubits per QPU”**: Required physical qubit count per QPU determined as $\mathcal{Q}_{\text{QPU}} =$

TABLE IX. Logical resource requirements for the hydrogen chain models across three initial-state infidelity parameter values: (a) $\xi = 0.1$, (b) $\xi = 0.05$, and (c) $\xi = 0.01$. Columns are grouped into “Hamiltonian” (L_D , λ_R , λ), “Logical circuit” (N_L , G_M), and “Error correction” (SMM priority, d , $\bar{\theta}_L$, P_{total}). Detailed definitions for these parameters and the underlying assumptions can be found in Appendix E 2 a.

Molecule ID	Hamiltonian			Logical circuit		Error correction			
	L_D	λ_R	λ	N_L	G_M	SMM priority	d	$\bar{\theta}_L$	P_{total}
(a) $\xi = 0.1$									
H ₁₀	217	2.66	25.52	21	1.36×10^5	accuracy	21	7.19×10^{-3}	3.98×10^{-2}
H ₂₀	552	7.59	62.54	41	9.49×10^5	accuracy	23	2.52×10^{-3}	1.04×10^{-1}
H ₃₀	1030	13.56	106.02	61	3.05×10^6	accuracy	25	1.33×10^{-3}	1.85×10^{-1}
H ₄₀	1609	19.90	150.75	81	6.78×10^6	accuracy	25	8.51×10^{-4}	2.82×10^{-1}
H ₅₀	2344	30.14	202.62	101	1.42×10^7	accuracy	25	5.48×10^{-4}	4.07×10^{-1}
(b) $\xi = 0.05$									
H ₁₀	165	3.14	24.41	21	4.89×10^4	speed	19	9.58×10^{-3}	6.86×10^{-1}
H ₂₀	466	8.93	62.45	41	3.75×10^5	accuracy	23	3.19×10^{-3}	5.07×10^{-2}
H ₃₀	873	15.97	105.12	61	1.20×10^6	accuracy	23	1.67×10^{-3}	9.02×10^{-2}
H ₄₀	1302	24.59	150.87	81	2.69×10^6	accuracy	25	1.07×10^{-3}	1.40×10^{-1}
H ₅₀	1772	33.51	198.31	101	4.91×10^6	accuracy	25	7.73×10^{-4}	1.96×10^{-1}
(c) $\xi = 0.01$									
H ₁₀	103	5.39	23.51	21	5.83×10^3	speed	17	1.55×10^{-2}	1.50×10^{-1}
H ₂₀	268	16.31	61.86	41	4.52×10^4	speed	19	5.26×10^{-3}	2.67×10^{-1}
H ₃₀	473	28.11	103.49	61	1.36×10^5	speed	21	2.93×10^{-3}	3.27×10^{-1}
H ₄₀	671	43.45	148.50	81	2.94×10^5	speed	21	1.94×10^{-3}	2.47×10^{-1}
H ₅₀	853	66.53	200.75	101	5.79×10^5	speed	23	1.33×10^{-3}	1.90×10^{-1}

TABLE X. Logical resource requirements for the iron-sulfur cluster models (listed in Table VI) across three initial-state infidelity parameter values: (a) $\xi = 0.1$, (b) $\xi = 0.05$, and (c) $\xi = 0.01$. Columns are grouped into “Hamiltonian” (L_D , λ_R , λ), “Logical circuit” (N_L , G_M), and “Error correction” (SMM priority, d , $\bar{\theta}_L$, P_{total}). Detailed definitions for these parameters and the underlying assumptions can be found in Appendix E 2 a.

Molecule ID	Hamiltonian			Logical circuit		Error correction			
	L_D	λ_R	λ	N_L	G_M	SMM priority	d	$\bar{\theta}_L$	P_{total}
(a) $\xi = 0.1$									
[2Fe-2S] ⁻³	922	12.88	45.35	41	1.70×10^6	accuracy	23	1.02×10^{-3}	8.66×10^{-2}
[2Fe-2S] ⁻²	1000	15.58	46.01	41	2.23×10^6	accuracy	23	7.91×10^{-4}	9.07×10^{-2}
[4Fe-4S] ⁻²	3707	68.58	136.89	73	3.69×10^7	accuracy	25	1.42×10^{-4}	3.25×10^{-1}
[4Fe-4S]	3831	68.39	138.73	73	3.72×10^7	accuracy	25	1.43×10^{-4}	3.24×10^{-1}
FeMoco (Sm)	12312	268.82	400.52	109	5.18×10^8	accuracy	27	2.96×10^{-5}	1.01×10^0
FeMoco (Lg)	15086	273.27	521.58	153	5.90×10^8	accuracy	29	3.38×10^{-5}	1.32×10^0
(b) $\xi = 0.05$									
[2Fe-2S] ⁻³	578	14.95	43.70	41	5.50×10^5	accuracy	23	1.52×10^{-3}	4.01×10^{-2}
[2Fe-2S] ⁻²	759	16.89	40.77	41	6.89×10^5	accuracy	23	1.13×10^{-3}	3.96×10^{-2}
[4Fe-4S] ⁻²	1793	73.61	141.80	73	1.03×10^7	accuracy	25	2.64×10^{-4}	1.60×10^{-1}
[4Fe-4S]	2181	74.96	135.50	73	1.09×10^7	accuracy	25	2.37×10^{-4}	1.57×10^{-1}
FeMoco (Sm)	5679	286.18	396.64	109	1.42×10^8	accuracy	27	5.36×10^{-5}	4.95×10^{-1}
FeMoco (Lg)	10429	294.98	522.53	153	1.80×10^8	accuracy	27	5.55×10^{-5}	6.52×10^{-1}
(c) $\xi = 0.01$									
[2Fe-2S] ⁻³	196	19.75	41.26	41	3.71×10^4	speed	19	4.27×10^{-3}	1.53×10^{-1}
[2Fe-2S] ⁻²	220	22.81	43.02	41	4.70×10^4	speed	19	3.50×10^{-3}	1.37×10^{-1}
[4Fe-4S] ⁻²	515	90.84	131.42	73	6.07×10^5	speed	21	8.29×10^{-4}	7.73×10^{-2}
[4Fe-4S]	483	91.92	133.98	73	6.14×10^5	speed	21	8.36×10^{-4}	1.10×10^{-1}
FeMoco (Sm)	1065	326.46	385.47	109	7.04×10^6	speed	25	2.10×10^{-4}	1.15×10^{-1}
FeMoco (Lg)	2362	369.30	506.14	153	1.03×10^7	speed	25	1.88×10^{-4}	1.40×10^{-1}

TABLE XI. Logical resource requirements for the P450-Cpd I and P450-rest models across three initial-state infidelity parameter values: (a) $\xi = 0.1$, (b) $\xi = 0.05$, and (c) $\xi = 0.01$. Columns are grouped into ‘‘Hamiltonian’’ (L_D , λ_R , λ), ‘‘Logical circuit’’ (N_L , G_M), and ‘‘Error correction’’ (SMM priority, d , $\bar{\theta}_L$, P_{total}). Detailed definitions for these parameters and the underlying assumptions can be found in Appendix E 2 a.

Molecule ID	Hamiltonian			Logical circuit		Error correction			
	L_D	λ_R	λ	N_L	G_M	SMM priority	d	$\bar{\theta}_L$	P_{total}
(a) $\xi = 0.1$									
P450-Cpd I (A)	15	0.13	0.87	11	2.96×10^2	speed	13	1.14×10^{-1}	5.59×10^{-2}
P450-Cpd I (B)	52	0.62	8.08	17	9.12×10^3	speed	17	3.41×10^{-2}	5.16×10^{-1}
P450-Cpd I (C)	343	4.98	24.52	31	2.89×10^5	accuracy	23	3.25×10^{-3}	4.16×10^{-2}
P450-Cpd I (D)	1447	21.93	65.08	47	4.49×10^6	accuracy	25	5.55×10^{-4}	1.32×10^{-1}
P450-Cpd I (E)	3088	44.61	115.12	63	1.81×10^7	accuracy	25	2.43×10^{-4}	2.56×10^{-1}
P450-Cpd I (F)	4343	61.06	153.96	83	3.41×10^7	accuracy	25	1.73×10^{-4}	3.55×10^{-1}
P450-Cpd I (G)	4596	67.50	164.61	87	4.06×10^7	accuracy	25	1.55×10^{-4}	3.82×10^{-1}
P450-Cpd I (X)	7150	124.60	287.23	117	1.30×10^8	accuracy	27	8.47×10^{-5}	6.89×10^{-1}
P450-rest (A)	17	0.18	1.39	11	5.42×10^2	speed	13	9.82×10^{-2}	8.85×10^{-2}
P450-rest (B)	70	0.70	5.11	17	8.61×10^3	speed	17	2.29×10^{-2}	3.25×10^{-1}
P450-rest (C)	253	3.33	21.58	27	1.58×10^5	accuracy	21	5.24×10^{-3}	3.46×10^{-2}
P450-rest (D)	893	13.71	46.14	41	1.82×10^6	accuracy	23	9.69×10^{-4}	8.79×10^{-2}
P450-rest (E)	1799	27.16	82.64	57	6.98×10^6	accuracy	25	4.53×10^{-4}	1.71×10^{-1}
P450-rest (F)	3230	46.13	129.59	81	2.01×10^7	accuracy	25	2.47×10^{-4}	2.91×10^{-1}
P450-rest (G)	3431	53.52	143.43	85	2.58×10^7	accuracy	25	2.13×10^{-4}	3.24×10^{-1}
P450-rest (X)	5853	98.74	253.19	113	8.49×10^7	accuracy	27	1.14×10^{-4}	5.93×10^{-1}
(b) $\xi = 0.05$									
P450-Cpd I (A)	12	0.19	0.87	11	1.44×10^2	speed	13	1.26×10^{-1}	3.01×10^{-2}
P450-Cpd I (B)	48	0.76	8.18	17	4.08×10^3	speed	17	3.86×10^{-2}	2.62×10^{-1}
P450-Cpd I (C)	233	5.79	24.08	31	9.70×10^4	speed	19	4.76×10^{-3}	5.13×10^{-1}
P450-Cpd I (D)	916	24.98	62.31	47	1.42×10^6	accuracy	23	8.40×10^{-4}	6.27×10^{-2}
P450-Cpd I (E)	2064	49.83	113.38	63	5.76×10^6	accuracy	25	3.77×10^{-4}	1.26×10^{-1}
P450-Cpd I (F)	2705	72.82	156.44	83	1.17×10^7	accuracy	25	2.57×10^{-4}	1.80×10^{-1}
P450-Cpd I (G)	2947	76.61	163.93	87	1.31×10^7	accuracy	25	2.40×10^{-4}	1.90×10^{-1}
P450-Cpd I (X)	4556	137.00	286.09	117	3.98×10^7	accuracy	27	1.38×10^{-4}	3.42×10^{-1}
P450-rest (A)	15	0.20	1.38	11	2.28×10^2	speed	13	1.23×10^{-1}	4.63×10^{-2}
P450-rest (B)	54	0.87	5.25	17	3.39×10^3	speed	15	2.97×10^{-2}	1.67×10^{-1}
P450-rest (C)	170	4.24	22.46	27	5.89×10^4	speed	19	7.32×10^{-3}	5.70×10^{-1}
P450-rest (D)	568	15.57	46.20	41	5.85×10^5	accuracy	23	1.51×10^{-3}	4.22×10^{-2}
P450-rest (E)	1180	31.04	81.66	57	2.27×10^6	accuracy	23	6.87×10^{-4}	8.40×10^{-2}
P450-rest (F)	2246	53.03	130.31	81	6.80×10^6	accuracy	25	3.67×10^{-4}	1.46×10^{-1}
P450-rest (G)	2391	61.29	143.26	85	8.64×10^6	accuracy	25	3.17×10^{-4}	1.62×10^{-1}
P450-rest (X)	3513	109.51	251.50	113	2.59×10^7	accuracy	25	1.86×10^{-4}	2.93×10^{-1}
(c) $\xi = 0.01$									
P450-Cpd I (A)	8	0.23	0.84	11	2.42×10^1	speed	11	2.13×10^{-1}	8.58×10^{-3}
P450-Cpd I (B)	36	1.59	4.74	17	4.56×10^2	speed	15	4.22×10^{-2}	3.20×10^{-2}
P450-Cpd I (C)	90	8.39	23.31	31	7.81×10^3	speed	17	1.15×10^{-2}	1.49×10^{-1}
P450-Cpd I (D)	266	33.07	60.16	47	9.34×10^4	speed	19	2.48×10^{-3}	1.46×10^{-1}
P450-Cpd I (E)	554	71.03	114.20	63	4.13×10^5	speed	21	1.06×10^{-3}	1.36×10^{-1}
P450-Cpd I (F)	839	94.38	150.98	83	7.58×10^5	speed	23	7.65×10^{-4}	1.18×10^{-1}
P450-Cpd I (G)	878	102.04	163.69	87	8.76×10^5	speed	23	7.16×10^{-4}	1.31×10^{-1}
P450-Cpd I (X)	1305	173.17	283.31	117	2.46×10^6	speed	23	4.41×10^{-4}	1.37×10^{-1}
P450-rest (A)	7	0.40	1.39	11	4.02×10^1	speed	11	1.89×10^{-1}	1.26×10^{-2}
P450-rest (B)	28	1.63	5.10	17	4.42×10^2	speed	15	4.89×10^{-2}	3.59×10^{-2}
P450-rest (C)	93	5.75	20.88	27	5.37×10^3	speed	17	1.52×10^{-2}	1.35×10^{-1}
P450-rest (D)	179	21.42	43.42	41	4.07×10^4	speed	19	4.10×10^{-3}	1.47×10^{-1}
P450-rest (E)	411	41.16	77.35	57	1.58×10^5	speed	21	1.89×10^{-3}	1.34×10^{-1}
P450-rest (F)	666	68.76	121.47	81	4.27×10^5	speed	21	1.09×10^{-3}	1.20×10^{-1}
P450-rest (G)	695	74.42	130.42	85	4.93×10^5	speed	21	1.02×10^{-3}	1.34×10^{-1}
P450-rest (X)	1234	137.58	244.10	113	1.68×10^6	speed	23	5.58×10^{-4}	1.37×10^{-1}

TABLE XII. Logical resource requirements for the P450-inhibited and P450-empty models across three initial-state infidelity parameter values: (a) $\xi = 0.1$, (b) $\xi = 0.05$, and (c) $\xi = 0.01$. Columns are grouped into ‘‘Hamiltonian’’ (L_D , λ_R , λ), ‘‘Logical circuit’’ (N_L , G_M), and ‘‘Error correction’’ (SMM priority, d , $\bar{\theta}_L$, P_{total}). Detailed definitions for these parameters and the underlying assumptions can be found in Appendix E 2 a.

Molecule ID	Hamiltonian			Logical circuit		Error correction			
	L_D	λ_R	λ	N_L	G_M	SMM priority	d	$\bar{\theta}_L$	P_{total}
(a) $\xi = 0.1$									
P450-inhibited (A)	32	0.21	1.02	11	8.13×10^2	speed	15	5.06×10^{-2}	6.83×10^{-2}
P450-inhibited (B)	70	1.17	10.18	19	1.97×10^4	speed	17	1.97×10^{-2}	6.32×10^{-1}
P450-inhibited (C)	303	3.71	21.28	29	1.90×10^5	accuracy	21	4.30×10^{-3}	3.48×10^{-2}
P450-inhibited (D)	1256	15.83	48.07	43	2.53×10^6	accuracy	23	7.28×10^{-4}	9.55×10^{-2}
P450-inhibited (E)	2628	42.04	109.39	65	1.56×10^7	accuracy	25	2.69×10^{-4}	2.39×10^{-1}
P450-inhibited (F)	3110	45.11	129.15	89	1.93×10^7	accuracy	25	2.57×10^{-4}	2.87×10^{-1}
P450-inhibited (G)	3317	49.58	136.88	93	2.27×10^7	accuracy	25	2.31×10^{-4}	3.06×10^{-1}
P450-inhibited (X)	6878	98.79	261.40	121	9.10×10^7	accuracy	27	1.10×10^{-4}	6.20×10^{-1}
P450-empty (A)	25	0.20	1.58	11	8.77×10^2	speed	15	7.19×10^{-2}	1.05×10^{-1}
P450-empty (B)	64	0.81	5.27	17	9.35×10^3	speed	17	2.18×10^{-2}	3.36×10^{-1}
P450-empty (C)	166	2.08	14.30	23	6.49×10^4	accuracy	21	8.44×10^{-3}	2.21×10^{-2}
P450-empty (D)	918	11.59	36.15	37	1.36×10^6	accuracy	23	1.02×10^{-3}	6.96×10^{-2}
P450-empty (E)	2156	25.16	74.83	53	6.59×10^6	accuracy	25	4.35×10^{-4}	1.60×10^{-1}
P450-empty (F)	2318	34.49	106.47	75	1.14×10^7	accuracy	25	3.56×10^{-4}	2.28×10^{-1}
P450-empty (G)	4140	44.14	135.12	79	2.17×10^7	accuracy	25	2.39×10^{-4}	3.08×10^{-1}
P450-empty (X)	5359	90.43	247.71	111	7.28×10^7	accuracy	27	1.30×10^{-4}	5.81×10^{-1}
(b) $\xi = 0.05$									
P450-inhibited (A)	26	0.28	0.94	11	3.53×10^2	speed	13	5.84×10^{-2}	3.42×10^{-2}
P450-inhibited (B)	48	1.54	9.82	19	7.39×10^3	speed	17	2.56×10^{-2}	3.14×10^{-1}
P450-inhibited (C)	214	4.35	20.52	29	6.51×10^4	speed	19	6.05×10^{-3}	4.79×10^{-1}
P450-inhibited (D)	775	18.22	47.26	43	8.09×10^5	accuracy	23	1.12×10^{-3}	4.53×10^{-2}
P450-inhibited (E)	1706	44.80	105.44	65	4.57×10^6	accuracy	25	4.42×10^{-4}	1.15×10^{-1}
P450-inhibited (F)	1938	51.00	126.01	89	6.04×10^6	accuracy	25	3.99×10^{-4}	1.39×10^{-1}
P450-inhibited (G)	2144	56.95	137.71	93	7.45×10^6	accuracy	25	3.54×10^{-4}	1.54×10^{-1}
P450-inhibited (X)	3766	113.63	260.04	121	2.81×10^7	accuracy	25	1.77×10^{-4}	3.07×10^{-1}
P450-empty (A)	19	0.27	1.62	11	3.68×10^2	speed	13	8.92×10^{-2}	5.44×10^{-2}
P450-empty (B)	48	0.98	5.33	17	3.51×10^3	speed	15	2.94×10^{-2}	1.71×10^{-1}
P450-empty (C)	130	2.46	13.05	23	2.32×10^4	speed	17	1.09×10^{-2}	3.91×10^{-1}
P450-empty (D)	479	14.15	36.94	37	4.47×10^5	accuracy	23	1.58×10^{-3}	3.39×10^{-2}
P450-empty (E)	1429	29.31	74.87	53	2.21×10^6	accuracy	23	6.47×10^{-4}	7.91×10^{-2}
P450-empty (F)	1535	38.11	103.98	75	3.58×10^6	accuracy	25	5.57×10^{-4}	1.10×10^{-1}
P450-empty (G)	2501	51.57	129.99	79	6.87×10^6	accuracy	25	3.62×10^{-4}	1.47×10^{-1}
P450-empty (X)	3589	102.53	243.59	111	2.36×10^7	accuracy	25	1.98×10^{-4}	2.86×10^{-1}
(c) $\xi = 0.01$									
P450-inhibited (A)	13	0.42	0.90	11	4.97×10^1	speed	11	1.04×10^{-1}	8.57×10^{-3}
P450-inhibited (B)	22	2.37	9.54	19	7.00×10^2	speed	15	5.35×10^{-2}	6.22×10^{-2}
P450-inhibited (C)	86	7.54	19.21	29	6.30×10^3	speed	17	1.19×10^{-2}	1.24×10^{-1}
P450-inhibited (D)	222	25.08	44.75	43	5.52×10^4	speed	19	3.14×10^{-3}	1.21×10^{-1}
P450-inhibited (E)	547	57.76	97.77	65	2.94×10^5	speed	21	1.28×10^{-3}	1.13×10^{-1}
P450-inhibited (F)	704	68.73	123.61	89	4.38×10^5	speed	21	1.08×10^{-3}	1.26×10^{-1}
P450-inhibited (G)	759	75.17	134.12	93	5.20×10^5	speed	21	9.90×10^{-4}	1.23×10^{-1}
P450-inhibited (X)	1285	144.77	253.32	121	1.84×10^6	speed	23	5.27×10^{-4}	1.21×10^{-1}
P450-empty (A)	8	0.36	1.44	11	3.80×10^1	speed	11	2.00×10^{-1}	1.26×10^{-2}
P450-empty (B)	28	1.54	5.39	17	4.03×10^2	speed	13	5.35×10^{-2}	3.58×10^{-2}
P450-empty (C)	55	4.26	13.58	23	2.37×10^3	speed	15	2.24×10^{-2}	8.80×10^{-2}
P450-empty (D)	190	18.12	34.90	37	3.13×10^4	speed	19	4.32×10^{-3}	1.23×10^{-1}
P450-empty (E)	462	42.87	73.53	53	1.70×10^5	speed	21	1.66×10^{-3}	1.07×10^{-1}
P450-empty (F)	590	52.53	98.79	75	2.69×10^5	speed	21	1.41×10^{-3}	1.15×10^{-1}
P450-empty (G)	778	75.48	127.92	79	5.18×10^5	speed	21	9.48×10^{-4}	1.09×10^{-1}
P450-empty (X)	1231	131.89	237.01	111	1.57×10^6	speed	23	5.79×10^{-4}	1.11×10^{-1}

TABLE XIII. Logical resource requirements for the ruthenium-based catalyst models, listed for structures I, II, II-III, and V (first half of the catalytic cycle [22]), across three initial-state infidelity parameter values: (a) $\xi = 0.1$, (b) $\xi = 0.05$, and (c) $\xi = 0.01$. Columns are grouped into “Hamiltonian” (L_D, λ_R, λ), “Logical circuit” (N_L, G_M), and “Error correction” (SMM priority, $d, \bar{\theta}_L, P_{\text{total}}$). Detailed definitions for these parameters and the underlying assumptions can be found in Appendix E 2 a.

Molecule ID	Hamiltonian			Logical circuit		Error correction			
	L_D	λ_R	λ	N_L	G_M	SMM priority	d	$\bar{\theta}_L$	P_{total}
(a) $\xi = 0.1$									
Ru-I (Sm)	60	0.68	4.59	11	7.11×10^3	speed	17	2.48×10^{-2}	2.91×10^{-1}
Ru-I (Md)	576	8.88	26.85	33	7.27×10^5	accuracy	23	1.41×10^{-3}	5.00×10^{-2}
Ru-I (Lg)	8235	192.44	270.04	105	2.59×10^8	accuracy	27	3.99×10^{-5}	6.73×10^{-1}
Ru-II (Sm)	60	0.77	5.49	13	8.77×10^3	speed	17	2.40×10^{-2}	3.48×10^{-1}
Ru-II (Md)	1355	26.36	77.56	53	5.95×10^6	accuracy	25	4.99×10^{-4}	1.57×10^{-1}
Ru-II (Lg)	11174	319.64	454.93	125	6.96×10^8	accuracy	29	2.50×10^{-5}	1.14×10^0
Ru-II-III (Sm)	70	0.68	5.92	13	9.38×10^3	speed	17	2.42×10^{-2}	3.76×10^{-1}
Ru-II-III (Md)	2280	42.87	108.56	59	1.53×10^7	accuracy	25	2.72×10^{-4}	2.33×10^{-1}
Ru-II-III (Lg)	13172	380.88	538.84	131	9.88×10^8	accuracy	29	2.09×10^{-5}	1.36×10^0
Ru-V (Sm)	460	5.03	24.35	23	3.40×10^5	accuracy	23	2.75×10^{-3}	4.11×10^{-2}
Ru-V (Md)	2264	26.93	85.83	49	7.74×10^6	accuracy	25	4.25×10^{-4}	1.87×10^{-1}
Ru-V (Lg)	9829	234.12	383.24	121	3.93×10^8	accuracy	27	3.73×10^{-5}	9.45×10^{-1}
(b) $\xi = 0.05$									
Ru-I (Sm)	50	0.85	4.81	11	3.04×10^3	speed	15	3.09×10^{-2}	1.56×10^{-1}
Ru-I (Md)	376	9.98	26.88	33	2.33×10^5	speed	21	2.21×10^{-3}	4.14×10^{-1}
Ru-I (Lg)	3901	203.69	268.25	105	7.06×10^7	accuracy	27	7.27×10^{-5}	3.32×10^{-1}
Ru-II (Sm)	54	1.01	5.50	13	3.87×10^3	speed	15	2.73×10^{-2}	1.75×10^{-1}
Ru-II (Md)	725	29.88	78.24	53	1.81×10^6	accuracy	23	8.25×10^{-4}	7.76×10^{-2}
Ru-II (Lg)	5436	332.03	453.13	125	1.85×10^8	accuracy	27	4.68×10^{-5}	5.56×10^{-1}
Ru-II-III (Sm)	46	0.97	5.83	13	3.55×10^3	speed	15	3.17×10^{-2}	1.86×10^{-1}
Ru-II-III (Md)	1175	47.26	106.71	59	4.41×10^6	accuracy	25	4.63×10^{-4}	1.13×10^{-1}
Ru-II-III (Lg)	6159	402.12	537.80	131	2.69×10^8	accuracy	27	3.83×10^{-5}	6.64×10^{-1}
Ru-V (Sm)	229	5.43	22.78	23	8.80×10^4	speed	19	4.97×10^{-3}	5.07×10^{-1}
Ru-V (Md)	1291	31.12	87.14	49	2.43×10^6	accuracy	23	6.86×10^{-4}	9.08×10^{-2}
Ru-V (Lg)	5247	257.34	391.86	121	1.17×10^8	accuracy	27	6.43×10^{-5}	4.80×10^{-1}
(c) $\xi = 0.01$									
Ru-I (Sm)	29	1.29	4.43	11	3.60×10^2	speed	13	5.37×10^{-2}	3.21×10^{-2}
Ru-I (Md)	127	13.31	25.61	33	1.61×10^4	speed	17	6.12×10^{-3}	1.28×10^{-1}
Ru-I (Lg)	621	226.40	264.02	105	3.32×10^6	speed	23	3.05×10^{-4}	8.62×10^{-2}
Ru-II (Sm)	50	1.17	5.28	13	5.42×10^2	speed	15	3.98×10^{-2}	3.58×10^{-2}
Ru-II (Md)	246	36.57	74.27	53	1.12×10^5	speed	21	2.55×10^{-3}	2.00×10^{-1}
Ru-II (Lg)	830	366.97	443.02	125	8.61×10^6	accuracy	25	1.97×10^{-4}	1.07×10^{-1}
Ru-II-III (Sm)	32	1.33	5.61	13	3.93×10^2	speed	13	5.48×10^{-2}	3.57×10^{-2}
Ru-II-III (Md)	330	57.79	101.61	59	2.57×10^5	speed	21	1.51×10^{-3}	1.99×10^{-1}
Ru-II-III (Lg)	986	436.84	525.08	131	1.22×10^7	accuracy	25	1.65×10^{-4}	1.28×10^{-1}
Ru-V (Sm)	103	7.95	21.83	23	7.52×10^3	speed	17	1.11×10^{-2}	1.37×10^{-1}
Ru-V (Md)	470	43.90	88.12	49	1.89×10^5	speed	21	1.80×10^{-3}	1.35×10^{-1}
Ru-V (Lg)	1134	287.05	382.91	121	5.67×10^6	speed	25	2.59×10^{-4}	1.31×10^{-1}

$N_{\text{patch}} \times 2d^2$, where $N_{\text{patch}} = 2N_L + \sqrt{8N_L} + 11$ is the number of surface code patches under the fast block layout [52, 84].

- **“Maximum per-shot runtime”**: Execution time for the deepest circuit $\mathcal{T}_{\text{max}} = \mathcal{T}_M$ as defined in Eq. (44).
- **“Time-to-solution (single QPU)”**: Total runtime $\mathcal{T}_{\text{total}}$ as defined in Eq. (45).

- **“QPU parallelism k^* ”**: Achievable QPU parallelism $k^* = \lfloor Q_{\text{budget}}/Q_{\text{QPU}} \rfloor$ under a fixed physical qubit budget of $Q_{\text{budget}} = 5 \times 10^5$.

- **“Time-to-solution (k^* QPUs)”**: Total runtime under parallel execution using k^* QPUs.

Selected results are shown in Table III in the main text.

TABLE XIV. Logical resource requirements for the ruthenium-based catalyst models, listed for structures VIII, VIII-IX, IX, and XVIII (second half of the catalytic cycle [22]), across three initial-state infidelity parameter values: (a) $\xi = 0.1$, (b) $\xi = 0.05$, and (c) $\xi = 0.01$. Columns are grouped into “Hamiltonian” (L_D , λ_R , λ), “Logical circuit” (N_L , G_M), and “Error correction” (SMM priority, d , $\bar{\theta}_L$, P_{total}). Detailed definitions for these parameters and the underlying assumptions can be found in Appendix E 2 a.

Molecule ID	Hamiltonian			Logical circuit		Error correction			
	L_D	λ_R	λ	N_L	G_M	SMM priority	d	$\bar{\theta}_L$	P_{total}
(a) $\xi = 0.1$									
Ru-VIII (Sm)	7	0.02	0.88	5	9.42×10^1	speed	11	3.57×10^{-1}	5.58×10^{-2}
Ru-VIII (Md)	2380	42.87	104.81	59	1.53×10^7	accuracy	25	2.63×10^{-4}	2.28×10^{-1}
Ru-VIII (Lg)	13649	410.72	573.09	131	1.14×10^9	accuracy	29	1.92×10^{-5}	1.45×10^0
Ru-VIII-IX (Sm)	38	0.24	2.77	9	1.97×10^3	speed	15	5.37×10^{-2}	1.76×10^{-1}
Ru-VIII-IX (Md)	1913	27.10	64.70	47	6.50×10^6	accuracy	25	3.81×10^{-4}	1.42×10^{-1}
Ru-VIII-IX (Lg)	10952	286.81	421.44	119	5.71×10^8	accuracy	29	2.83×10^{-5}	1.05×10^0
Ru-IX (Sm)	872	12.16	45.01	33	1.55×10^6	accuracy	23	1.11×10^{-3}	8.58×10^{-2}
Ru-IX (Md)	2284	35.13	103.21	53	1.15×10^7	accuracy	25	3.44×10^{-4}	2.19×10^{-1}
Ru-IX (Lg)	10847	246.37	407.31	125	4.40×10^8	accuracy	27	3.54×10^{-5}	1.01×10^0
Ru-XVIII (Sm)	30	0.30	3.50	9	2.17×10^3	speed	15	6.18×10^{-2}	2.23×10^{-1}
Ru-XVIII (Md)	961	15.83	42.57	41	2.18×10^6	accuracy	23	7.47×10^{-4}	8.57×10^{-2}
Ru-XVIII (Lg)	9370	235.63	343.63	113	3.87×10^8	accuracy	27	3.40×10^{-5}	8.53×10^{-1}
(b) $\xi = 0.05$									
Ru-VIII (Sm)	7	0.02	0.87	5	5.00×10^1	speed	11	3.62×10^{-1}	3.00×10^{-2}
Ru-VIII (Md)	1252	47.89	105.81	59	4.56×10^6	accuracy	25	4.44×10^{-4}	1.13×10^{-1}
Ru-VIII (Lg)	6559	428.57	574.56	131	3.06×10^8	accuracy	27	3.60×10^{-5}	7.12×10^{-1}
Ru-VIII-IX (Sm)	23	0.35	2.77	9	6.88×10^2	speed	15	7.88×10^{-2}	9.00×10^{-2}
Ru-VIII-IX (Md)	1087	30.39	66.71	47	2.00×10^6	accuracy	23	6.40×10^{-4}	7.09×10^{-2}
Ru-VIII-IX (Lg)	5285	306.84	423.25	119	1.59×10^8	accuracy	27	5.08×10^{-5}	5.18×10^{-1}
Ru-IX (Sm)	538	13.77	43.19	33	4.82×10^5	accuracy	23	1.72×10^{-3}	3.92×10^{-2}
Ru-IX (Md)	1716	39.28	103.12	53	3.86×10^6	accuracy	25	5.11×10^{-4}	1.12×10^{-1}
Ru-IX (Lg)	5496	265.51	406.07	125	1.25×10^8	accuracy	27	6.23×10^{-5}	5.00×10^{-1}
Ru-XVIII (Sm)	37	0.55	3.41	9	1.45×10^3	speed	15	4.56×10^{-2}	1.10×10^{-1}
Ru-XVIII (Md)	539	17.87	40.96	41	6.62×10^5	accuracy	23	1.19×10^{-3}	3.98×10^{-2}
Ru-XVIII (Lg)	4188	249.08	337.38	113	1.04×10^8	accuracy	27	6.19×10^{-5}	4.13×10^{-1}
(c) $\xi = 0.01$									
Ru-VIII (Sm)	6	0.07	0.84	5	1.28×10^1	speed	9	4.02×10^{-1}	8.54×10^{-3}
Ru-VIII (Md)	324	59.28	102.57	59	2.68×10^5	speed	21	1.47×10^{-3}	2.07×10^{-1}
Ru-VIII (Lg)	1008	468.01	555.35	131	1.39×10^7	accuracy	25	1.53×10^{-4}	1.35×10^{-1}
Ru-VIII-IX (Sm)	16	0.68	2.82	9	1.15×10^2	speed	13	1.07×10^{-1}	2.04×10^{-2}
Ru-VIII-IX (Md)	223	41.03	66.78	47	1.26×10^5	speed	21	2.04×10^{-3}	1.41×10^{-1}
Ru-VIII-IX (Lg)	962	336.42	414.35	119	7.41×10^6	accuracy	25	2.14×10^{-4}	1.00×10^{-1}
Ru-IX (Sm)	215	18.84	41.56	33	3.69×10^4	speed	19	4.35×10^{-3}	1.43×10^{-1}
Ru-IX (Md)	443	53.23	99.07	53	2.46×10^5	speed	21	1.54×10^{-3}	1.68×10^{-1}
Ru-IX (Lg)	1367	298.78	397.15	125	6.27×10^6	speed	25	2.42×10^{-4}	1.24×10^{-1}
Ru-XVIII (Sm)	16	0.68	3.31	9	1.32×10^2	speed	13	1.11×10^{-1}	2.44×10^{-2}
Ru-XVIII (Md)	159	22.79	39.39	41	4.20×10^4	speed	19	3.63×10^{-3}	1.14×10^{-1}
Ru-XVIII (Lg)	704	275.00	338.47	113	4.90×10^6	speed	25	2.65×10^{-4}	1.23×10^{-1}

Appendix F: Detailed performance of STAR-magic mutation

Here, we describe some technical details regarding the STAR-magic mutation (SMM) protocol [52], necessary to derive our resource estimates in Sec. V.

As discussed in Sec. V A, both the logical error factor $\alpha_{\text{RUS}}(\theta_L)$ and the execution time $C_{\text{smm}}(\theta_L)$ associated

with a single analog rotation gate $\hat{R}_P(\theta_L) = e^{i\theta_L \hat{P}}$ are sensitive to the adjustment of the threshold angle θ_{th} on the SMM architecture. Consequently, while optimizing performance specifically for each rotation angle θ_L is desirable, such fine-grained optimization is computationally demanding. For simplicity in this study, we therefore conducted resource estimation using two distinct patterns of threshold angle adjustment. The functional de-

TABLE XV. Physical resource estimates for the hydrogen chain models across three initial-state infidelity parameter values: (a) $\xi = 0.1$, (b) $\xi = 0.05$, and (c) $\xi = 0.01$. Columns include “Physical qubits per QPU”, “Maximum per-shot runtime”, “Time-to-solution (single QPU)”, “QPU parallelism k^* ”, and “Time-to-solution (k^* QPUs)”. Detailed definitions for these parameters and the underlying assumptions can be found in Appendix E 2 b.

Molecule ID	Physical qubits per QPU	Maximum per-shot runtime [s]	Time-to-solution (single QPU) [days]	QPU parallelism k^* ($Q_{\text{budget}} = 5 \times 10^5$)	Time-to-solution (k^* QPUs) [days]
(a) $\xi = 0.1$					
H ₁₀	5.82×10^4	9.53×10^1	1.13×10^0	10	1.37×10^{-1}
H ₂₀	1.18×10^5	4.40×10^2	1.07×10^1	5	2.57×10^0
H ₃₀	1.94×10^5	1.06×10^3	2.17×10^1	3	9.52×10^0
H ₄₀	2.48×10^5	1.96×10^3	6.72×10^1	2	3.36×10^1
H ₅₀	3.02×10^5	3.20×10^3	1.35×10^2	1	1.34×10^2
(b) $\xi = 0.05$					
H ₁₀	4.76×10^4	3.03×10^0	1.24×10^0	10	1.23×10^{-1}
H ₂₀	1.18×10^5	2.23×10^2	8.74×10^0	5	2.12×10^0
H ₃₀	1.64×10^5	4.65×10^2	1.89×10^1	3	6.29×10^0
H ₄₀	2.48×10^5	8.58×10^2	4.50×10^1	2	2.25×10^1
H ₅₀	3.02×10^5	1.37×10^3	8.20×10^1	1	8.17×10^1
(c) $\xi = 0.01$					
H ₁₀	3.81×10^4	3.12×10^{-1}	3.60×10^{-1}	13	2.76×10^{-2}
H ₂₀	8.02×10^4	2.87×10^0	5.26×10^0	6	8.77×10^{-1}
H ₃₀	1.37×10^5	1.00×10^1	2.34×10^1	3	7.79×10^0
H ₄₀	1.75×10^5	2.24×10^1	3.83×10^1	2	1.92×10^1
H ₅₀	2.55×10^5	4.98×10^1	6.73×10^1	1	6.72×10^1

TABLE XVI. Physical resource estimates for the iron-sulfur cluster models across three initial-state infidelity parameter values: (a) $\xi = 0.1$, (b) $\xi = 0.05$, and (c) $\xi = 0.01$. Columns include “Physical qubits per QPU”, “Maximum per-shot runtime”, “Time-to-solution (single QPU)”, “QPU parallelism k^* ”, and “Time-to-solution (k^* QPUs)”. Detailed definitions for these parameters and the underlying assumptions can be found in Appendix E 2 b.

Molecule ID	Physical qubits per QPU	Maximum per-shot runtime [s]	Time-to-solution (single QPU) [days]	QPU parallelism k^* ($Q_{\text{budget}} = 5 \times 10^5$)	Time-to-solution (k^* QPUs) [days]
(a) $\xi = 0.1$					
[2Fe-2S] ⁻³	1.18×10^5	3.77×10^2	6.34×10^0	4	1.50×10^0
[2Fe-2S] ⁻²	1.18×10^5	4.73×10^2	7.28×10^0	4	1.74×10^0
[4Fe-4S] ⁻²	2.26×10^5	3.68×10^3	1.50×10^2	2	7.49×10^1
[4Fe-4S]	2.26×10^5	3.66×10^3	1.48×10^2	2	7.41×10^1
FeMoco (Sm)	3.77×10^5	3.28×10^4	1.23×10^4	1	1.23×10^4
FeMoco (Lg)	5.92×10^5	4.10×10^4	6.08×10^4	1	6.08×10^4
(b) $\xi = 0.05$					
[2Fe-2S] ⁻³	1.18×10^5	1.90×10^2	6.25×10^0	5	1.52×10^0
[2Fe-2S] ⁻²	1.18×10^5	1.85×10^2	6.22×10^0	5	1.51×10^0
[4Fe-4S] ⁻²	2.26×10^5	1.48×10^3	8.35×10^1	2	4.16×10^1
[4Fe-4S]	2.26×10^5	1.51×10^3	8.41×10^1	2	4.20×10^1
FeMoco (Sm)	3.77×10^5	1.02×10^4	1.93×10^3	1	1.93×10^3
FeMoco (Lg)	5.13×10^5	1.31×10^4	4.91×10^3	1	4.91×10^3
(c) $\xi = 0.01$					
[2Fe-2S] ⁻³	8.02×10^4	2.40×10^0	2.81×10^0	6	4.68×10^{-1}
[2Fe-2S] ⁻²	8.02×10^4	3.09×10^0	3.39×10^0	6	5.65×10^{-1}
[4Fe-4S] ⁻²	1.60×10^5	4.92×10^1	4.23×10^1	3	1.41×10^1
[4Fe-4S]	1.60×10^5	4.97×10^1	4.88×10^1	3	1.63×10^1
FeMoco (Sm)	3.23×10^5	7.29×10^2	7.31×10^2	1	7.31×10^2
FeMoco (Lg)	4.40×10^5	1.06×10^3	1.17×10^3	1	1.17×10^3

TABLE XVII. Physical resource estimates for the P450-Cpd I and P450-rest models across three initial-state infidelity parameter values: (a) $\xi = 0.1$, (b) $\xi = 0.05$, and (c) $\xi = 0.01$. Columns include “Physical qubits per QPU”, “Maximum per-shot runtime”, “Time-to-solution (single QPU)”, “QPU parallelism k^* ”, and “Time-to-solution (k^* QPUs)”. Detailed definitions for these parameters and the underlying assumptions can be found in Appendix E 2 b.

Molecule ID	Physical qubits per QPU	Maximum per-shot runtime [s]	Time-to-solution (single QPU) [days]	QPU parallelism k^* ($Q_{\text{budget}} = 5 \times 10^5$)	Time-to-solution (k^* QPUs) [days]
(a) $\xi = 0.1$					
P450-Cpd I (A)	1.43×10^4	1.22×10^{-2}	1.72×10^{-4}	34	4.73×10^{-6}
P450-Cpd I (B)	3.28×10^4	4.89×10^{-1}	4.97×10^{-2}	15	3.27×10^{-3}
P450-Cpd I (C)	9.39×10^4	1.37×10^2	1.58×10^0	6	2.92×10^{-1}
P450-Cpd I (D)	1.55×10^5	9.32×10^2	2.04×10^1	3	6.65×10^0
P450-Cpd I (E)	1.99×10^5	2.35×10^3	9.50×10^1	2	4.72×10^1
P450-Cpd I (F)	2.53×10^5	3.64×10^3	1.52×10^2	1	1.49×10^2
P450-Cpd I (G)	2.64×10^5	4.09×10^3	1.77×10^2	1	1.74×10^2
P450-Cpd I (X)	4.02×10^5	1.07×10^4	1.45×10^3	1	1.45×10^3
P450-rest (A)	1.43×10^4	2.23×10^{-2}	4.15×10^{-4}	34	1.18×10^{-5}
P450-rest (B)	3.28×10^4	4.60×10^{-1}	1.81×10^{-2}	15	1.16×10^{-3}
P450-rest (C)	7.03×10^4	9.53×10^1	1.20×10^0	8	1.68×10^{-1}
P450-rest (D)	1.18×10^5	3.97×10^2	6.39×10^0	4	1.52×10^0
P450-rest (E)	1.83×10^5	1.35×10^3	2.81×10^1	3	1.33×10^1
P450-rest (F)	2.48×10^5	2.62×10^3	1.05×10^2	2	5.24×10^1
P450-rest (G)	2.59×10^5	3.06×10^3	1.23×10^2	1	1.20×10^2
P450-rest (X)	3.89×10^5	7.86×10^3	8.69×10^2	1	8.69×10^2
(b) $\xi = 0.05$					
P450-Cpd I (A)	1.43×10^4	5.90×10^{-3}	1.89×10^{-4}	34	5.37×10^{-6}
P450-Cpd I (B)	3.28×10^4	2.19×10^{-1}	1.97×10^{-2}	15	1.29×10^{-3}
P450-Cpd I (C)	6.41×10^4	6.44×10^0	1.34×10^0	7	1.90×10^{-1}
P450-Cpd I (D)	1.32×10^5	2.84×10^2	1.17×10^1	3	3.80×10^0
P450-Cpd I (E)	1.99×10^5	1.03×10^3	5.48×10^1	2	2.72×10^1
P450-Cpd I (F)	2.53×10^5	1.64×10^3	9.72×10^1	1	9.49×10^1
P450-Cpd I (G)	2.64×10^5	1.76×10^3	1.07×10^2	1	1.05×10^2
P450-Cpd I (X)	4.02×10^5	4.11×10^3	4.56×10^2	1	4.56×10^2
P450-rest (A)	1.43×10^4	9.35×10^{-3}	3.44×10^{-4}	34	9.86×10^{-6}
P450-rest (B)	2.55×10^4	1.60×10^{-1}	9.39×10^{-3}	19	4.90×10^{-4}
P450-rest (C)	5.75×10^4	3.80×10^0	9.97×10^{-1}	8	1.24×10^{-1}
P450-rest (D)	1.18×10^5	1.80×10^2	6.12×10^0	5	1.48×10^0
P450-rest (E)	1.55×10^5	4.65×10^2	1.87×10^1	3	6.24×10^0
P450-rest (F)	2.48×10^5	1.21×10^3	6.62×10^1	2	3.31×10^1
P450-rest (G)	2.59×10^5	1.40×10^3	7.87×10^1	1	7.66×10^1
P450-rest (X)	3.34×10^5	2.88×10^3	2.81×10^2	1	2.81×10^2
(c) $\xi = 0.01$					
P450-Cpd I (A)	1.03×10^4	8.41×10^{-4}	5.49×10^{-4}	48	1.14×10^{-5}
P450-Cpd I (B)	2.55×10^4	2.16×10^{-2}	1.55×10^{-2}	19	8.16×10^{-4}
P450-Cpd I (C)	5.13×10^4	4.12×10^{-1}	4.74×10^{-1}	9	5.26×10^{-2}
P450-Cpd I (D)	8.98×10^4	6.36×10^0	7.19×10^0	5	1.44×10^0
P450-Cpd I (E)	1.41×10^5	3.29×10^1	3.58×10^1	3	1.19×10^1
P450-Cpd I (F)	2.15×10^5	6.76×10^1	6.89×10^1	2	3.44×10^1
P450-Cpd I (G)	2.24×10^5	7.85×10^1	8.40×10^1	2	4.20×10^1
P450-Cpd I (X)	2.92×10^5	2.26×10^2	2.48×10^2	1	2.48×10^2
P450-rest (A)	1.03×10^4	1.39×10^{-3}	9.29×10^{-4}	48	1.94×10^{-5}
P450-rest (B)	2.55×10^4	2.09×10^{-2}	1.53×10^{-2}	19	8.05×10^{-4}
P450-rest (C)	4.61×10^4	2.87×10^{-1}	3.13×10^{-1}	10	3.13×10^{-2}
P450-rest (D)	8.02×10^4	2.66×10^0	3.04×10^0	6	5.06×10^{-1}
P450-rest (E)	1.29×10^5	1.21×10^1	1.31×10^1	3	4.36×10^0
P450-rest (F)	1.75×10^5	3.39×10^1	3.46×10^1	2	1.73×10^1
P450-rest (G)	1.83×10^5	3.94×10^1	4.24×10^1	2	2.12×10^1
P450-rest (X)	2.83×10^5	1.52×10^2	1.67×10^2	1	1.66×10^2

TABLE XVIII. Physical resource estimates for the P450-inhibited and P450-empty models across three initial-state infidelity parameter values: (a) $\xi = 0.1$, (b) $\xi = 0.05$, and (c) $\xi = 0.01$. Columns include “Physical qubits per QPU”, “Maximum per-shot runtime”, “Time-to-solution (single QPU)”, “QPU parallelism k^* ”, and “Time-to-solution (k^* QPUs)”. Detailed definitions for these parameters and the underlying assumptions can be found in Appendix E 2 b.

Molecule ID	Physical qubits per QPU	Maximum per-shot runtime [s]	Time-to-solution (single QPU) [days]	QPU parallelism k^* ($Q_{\text{budget}} = 5 \times 10^5$)	Time-to-solution (k^* QPUs) [days]
(a) $\xi = 0.1$					
P450-inhibited (A)	1.91×10^4	3.85×10^{-2}	4.72×10^{-4}	26	1.65×10^{-5}
P450-inhibited (B)	3.54×10^4	1.08×10^0	1.20×10^{-1}	14	8.54×10^{-3}
P450-inhibited (C)	7.43×10^4	1.00×10^2	1.26×10^0	6	2.03×10^{-1}
P450-inhibited (D)	1.22×10^5	5.24×10^2	7.80×10^0	4	1.93×10^0
P450-inhibited (E)	2.05×10^5	2.14×10^3	4.81×10^1	2	2.38×10^1
P450-inhibited (F)	2.70×10^5	2.56×10^3	1.01×10^2	1	9.80×10^1
P450-inhibited (G)	2.80×10^5	2.83×10^3	1.12×10^2	1	1.09×10^2
P450-inhibited (X)	4.14×10^5	8.34×10^3	9.76×10^2	1	9.76×10^2
P450-empty (A)	1.91×10^4	4.15×10^{-2}	6.70×10^{-4}	26	2.31×10^{-5}
P450-empty (B)	3.28×10^4	4.97×10^{-1}	1.94×10^{-2}	15	1.25×10^{-3}
P450-empty (C)	6.22×10^4	5.13×10^1	4.20×10^{-1}	9	5.09×10^{-2}
P450-empty (D)	1.08×10^5	2.98×10^2	5.48×10^0	4	1.28×10^0
P450-empty (E)	1.72×10^5	1.26×10^3	2.71×10^1	3	1.27×10^1
P450-empty (F)	2.32×10^5	1.91×10^3	4.16×10^1	2	2.06×10^1
P450-empty (G)	2.43×10^5	2.80×10^3	1.13×10^2	2	5.65×10^1
P450-empty (X)	3.83×10^5	7.19×10^3	7.85×10^2	1	7.85×10^2
(b) $\xi = 0.05$					
P450-inhibited (A)	1.43×10^4	1.45×10^{-2}	4.63×10^{-4}	34	1.35×10^{-5}
P450-inhibited (B)	3.54×10^4	3.90×10^{-1}	3.96×10^{-2}	14	2.80×10^{-3}
P450-inhibited (C)	6.08×10^4	4.24×10^0	7.96×10^{-1}	8	9.89×10^{-2}
P450-inhibited (D)	1.22×10^5	2.07×10^2	6.94×10^0	4	1.72×10^0
P450-inhibited (E)	2.05×10^5	9.01×10^2	3.84×10^1	2	1.90×10^1
P450-inhibited (F)	2.70×10^5	1.13×10^3	6.07×10^1	1	5.86×10^1
P450-inhibited (G)	2.80×10^5	1.30×10^3	7.13×10^1	1	6.94×10^1
P450-inhibited (X)	3.55×10^5	3.06×10^3	3.08×10^2	1	3.08×10^2
P450-empty (A)	1.43×10^4	1.51×10^{-2}	5.49×10^{-4}	34	1.60×10^{-5}
P450-empty (B)	2.55×10^4	1.66×10^{-1}	9.78×10^{-3}	19	5.11×10^{-4}
P450-empty (C)	4.08×10^4	1.28×10^0	1.64×10^{-1}	12	1.37×10^{-2}
P450-empty (D)	1.08×10^5	1.53×10^2	5.14×10^0	5	1.24×10^0
P450-empty (E)	1.46×10^5	4.33×10^2	1.74×10^1	3	5.73×10^0
P450-empty (F)	2.32×10^5	7.86×10^2	3.31×10^1	2	1.64×10^1
P450-empty (G)	2.43×10^5	1.21×10^3	6.60×10^1	2	3.30×10^1
P450-empty (X)	3.28×10^5	2.74×10^3	2.61×10^2	1	2.61×10^2
(c) $\xi = 0.01$					
P450-inhibited (A)	1.03×10^4	1.72×10^{-3}	1.13×10^{-3}	48	2.34×10^{-5}
P450-inhibited (B)	2.76×10^4	3.31×10^{-2}	2.68×10^{-2}	18	1.49×10^{-3}
P450-inhibited (C)	4.87×10^4	3.32×10^{-1}	3.47×10^{-1}	10	3.47×10^{-2}
P450-inhibited (D)	8.34×10^4	3.68×10^0	3.78×10^0	5	7.56×10^{-1}
P450-inhibited (E)	1.44×10^5	2.30×10^1	2.29×10^1	3	7.63×10^0
P450-inhibited (F)	1.90×10^5	3.48×10^1	3.63×10^1	2	1.81×10^1
P450-inhibited (G)	1.98×10^5	4.16×10^1	4.28×10^1	2	2.14×10^1
P450-inhibited (X)	3.01×10^5	1.68×10^2	1.72×10^2	1	1.72×10^2
P450-empty (A)	1.03×10^4	1.32×10^{-3}	8.79×10^{-4}	48	1.83×10^{-5}
P450-empty (B)	1.92×10^4	1.65×10^{-2}	1.21×10^{-2}	26	4.67×10^{-4}
P450-empty (C)	3.18×10^4	1.12×10^{-1}	1.01×10^{-1}	15	6.73×10^{-3}
P450-empty (D)	7.38×10^4	2.02×10^0	2.08×10^0	6	3.47×10^{-1}
P450-empty (E)	1.21×10^5	1.31×10^1	1.28×10^1	4	3.20×10^0
P450-empty (F)	1.64×10^5	2.09×10^1	2.10×10^1	3	7.00×10^0
P450-empty (G)	1.71×10^5	4.15×10^1	4.05×10^1	2	2.02×10^1
P450-empty (X)	2.78×10^5	1.42×10^2	1.40×10^2	1	1.40×10^2

TABLE XIX. Physical resource estimates for the ruthenium-based catalyst models, listed for structures I, II, II-III, and V (first half of the catalytic cycle [22]), across three initial-state infidelity parameter values: (a) $\xi = 0.1$, (b) $\xi = 0.05$, and (c) $\xi = 0.01$. Columns include “Physical qubits per QPU”, “Maximum per-shot runtime [s]”, “Time-to-solution (single QPU) [days]”, “QPU parallelism k^* ”, and “Time-to-solution (k^* QPUs)”. Detailed definitions for these parameters and the underlying assumptions can be found in Appendix E 2 b.

Molecule ID	Physical qubits per QPU	Maximum per-shot runtime [s]	Time-to-solution (single QPU) [days]	QPU parallelism k^* ($Q_{\text{budget}} = 5 \times 10^5$)	Time-to-solution (k^* QPUs) [days]
(a) $\xi = 0.1$					
Ru-I (Sm)	2.45×10^4	3.80×10^{-1}	1.48×10^{-2}	20	7.06×10^{-4}
Ru-I (Md)	9.87×10^4	2.01×10^2	2.42×10^0	6	4.48×10^{-1}
Ru-I (Lg)	3.64×10^5	1.74×10^4	2.29×10^3	1	2.29×10^3
Ru-II (Sm)	2.73×10^4	4.66×10^{-1}	1.86×10^{-2}	18	9.95×10^{-4}
Ru-II (Md)	1.72×10^5	1.14×10^3	2.33×10^1	3	9.82×10^0
Ru-II (Lg)	4.92×10^5	4.61×10^4	4.27×10^4	1	4.27×10^4
Ru-II-III (Sm)	2.73×10^4	5.01×10^{-1}	2.12×10^{-2}	18	1.14×10^{-3}
Ru-II-III (Md)	1.88×10^5	2.01×10^3	4.44×10^1	2	2.14×10^1
Ru-II-III (Lg)	5.14×10^5	6.38×10^4	1.06×10^5	1	1.06×10^5
Ru-V (Sm)	7.47×10^4	1.61×10^2	1.85×10^0	8	2.77×10^{-1}
Ru-V (Md)	1.61×10^5	1.46×10^3	3.09×10^1	3	1.02×10^1
Ru-V (Lg)	4.14×10^5	2.59×10^4	7.64×10^3	1	7.64×10^3
(b) $\xi = 0.05$					
Ru-I (Sm)	1.91×10^4	1.44×10^{-1}	8.29×10^{-3}	26	3.16×10^{-4}
Ru-I (Md)	8.22×10^4	1.79×10^1	2.46×10^0	6	4.07×10^{-1}
Ru-I (Lg)	3.64×10^5	5.66×10^3	6.10×10^2	1	6.10×10^2
Ru-II (Sm)	2.12×10^4	1.83×10^{-1}	1.10×10^{-2}	23	4.74×10^{-4}
Ru-II (Md)	1.46×10^5	3.74×10^2	1.51×10^1	3	4.94×10^0
Ru-II (Lg)	4.27×10^5	1.29×10^4	3.52×10^3	1	3.52×10^3
Ru-II-III (Sm)	2.12×10^4	1.68×10^{-1}	1.03×10^{-2}	23	4.43×10^{-4}
Ru-II-III (Md)	1.88×10^5	8.49×10^2	3.61×10^1	3	1.76×10^1
Ru-II-III (Lg)	4.45×10^5	1.79×10^4	6.93×10^3	1	6.93×10^3
Ru-V (Sm)	5.09×10^4	5.81×10^0	1.18×10^0	9	1.31×10^{-1}
Ru-V (Md)	1.36×10^5	5.17×10^2	2.11×10^1	3	6.95×10^0
Ru-V (Lg)	4.14×10^5	8.88×10^3	1.58×10^3	1	1.58×10^3
(c) $\xi = 0.01$					
Ru-I (Sm)	1.43×10^4	1.48×10^{-2}	1.06×10^{-2}	34	3.12×10^{-4}
Ru-I (Md)	5.39×10^4	9.00×10^{-1}	9.50×10^{-1}	9	1.06×10^{-1}
Ru-I (Lg)	2.64×10^5	3.11×10^2	2.77×10^2	1	2.76×10^2
Ru-II (Sm)	2.12×10^4	2.56×10^{-2}	1.88×10^{-2}	23	8.16×10^{-4}
Ru-II (Md)	1.21×10^5	8.44×10^0	1.19×10^1	4	2.97×10^0
Ru-II (Lg)	3.66×10^5	1.11×10^3	1.07×10^3	1	1.07×10^3
Ru-II-III (Sm)	1.60×10^4	1.61×10^{-2}	1.18×10^{-2}	31	3.82×10^{-4}
Ru-II-III (Md)	1.33×10^5	2.01×10^1	2.81×10^1	3	9.37×10^0
Ru-II-III (Lg)	3.82×10^5	1.38×10^3	1.45×10^3	1	1.45×10^3
Ru-V (Sm)	4.08×10^4	3.99×10^{-1}	4.37×10^{-1}	12	3.64×10^{-2}
Ru-V (Md)	1.14×10^5	1.45×10^1	1.57×10^1	4	3.92×10^0
Ru-V (Lg)	3.55×10^5	5.83×10^2	6.20×10^2	1	6.20×10^2

dependencies of the performance parameters ($\alpha_{\text{RUS}}(\theta_L)$ and $C_{\text{smm}}(\theta_L)$) for each pattern are shown in Fig. 9.

The first pattern, termed “accuracy prioritized,” involves an implementation that emphasizes minimizing the logical error rate $P_L(\theta_L) = \alpha_{\text{RUS}}(\theta_L) \cdot \theta_L \cdot p_{\text{ph}}$. In this setting, the threshold angle θ_{th} is determined for each θ_L by selecting the optimal integer n (from $\theta_{\text{th}} = 2^n \theta_L$, $n \in \mathbb{N}$) that yields the lowest $P_L(\theta_L)$. The second pattern, “speed prioritized,” focuses on accelerating the ex-

ecution of large-angle rotation gates. For this setting, the threshold angle is chosen to satisfy $\theta_{\text{th}}/\theta_L \geq 2^5$ when $p_{\text{ph}} = 10^{-3}$, and $\theta_{\text{th}}/\theta_L \geq 2^6$ when $p_{\text{ph}} = 5 \times 10^{-4}$. By actively setting the threshold angle through these criteria, the RUS protocol is configured to delay the transition to the slow T -gate execution, effectively accelerating the overall execution time at the cost of accuracy [52]. Figure 9 clearly demonstrates the trade-off existing between the error rate and execution speed, par-

TABLE XX. Physical resource estimates for the ruthenium-based catalyst models, listed for structures VIII, VIII-IX, IX, and XVIII (second half of the catalytic cycle [22]), across three initial-state infidelity parameter values: (a) $\xi = 0.1$, (b) $\xi = 0.05$, and (c) $\xi = 0.01$. Columns include “Physical qubits per QPU”, “Maximum per-shot runtime [s]”, “Time-to-solution (single QPU) [days]”, “QPU parallelism k^* ”, and “Time-to-solution (k^* QPUs) [days]”. Detailed definitions for these parameters and the underlying assumptions can be found in Appendix E 2 b.

Molecule ID	Physical qubits per QPU	Maximum per-shot runtime [s]	Time-to-solution (single QPU) [days]	QPU parallelism k^* ($Q_{\text{budget}} = 5 \times 10^5$)	Time-to-solution (k^* QPUs) [days]
(a) $\xi = 0.1$					
Ru-VIII (Sm)	6.61×10^3	3.27×10^{-3}	5.52×10^{-5}	75	7.24×10^{-7}
Ru-VIII (Md)	1.88×10^5	2.00×10^3	4.44×10^1	2	2.14×10^1
Ru-VIII (Lg)	5.14×10^5	7.30×10^4	1.69×10^5	1	1.69×10^5
Ru-VIII-IX (Sm)	1.69×10^4	9.35×10^{-2}	2.24×10^{-3}	29	7.27×10^{-5}
Ru-VIII-IX (Md)	1.55×10^5	1.14×10^3	2.62×10^1	3	8.59×10^0
Ru-VIII-IX (Lg)	4.71×10^5	3.85×10^4	1.64×10^4	1	1.64×10^4
Ru-IX (Sm)	9.87×10^4	3.73×10^2	6.06×10^0	5	1.16×10^0
Ru-IX (Md)	1.72×10^5	1.86×10^3	4.01×10^1	2	1.91×10^1
Ru-IX (Lg)	4.27×10^5	2.88×10^4	1.08×10^4	1	1.08×10^4
Ru-XVIII (Sm)	1.69×10^4	1.03×10^{-1}	2.42×10^{-3}	29	7.93×10^{-5}
Ru-XVIII (Md)	1.18×10^5	4.34×10^2	6.81×10^0	4	1.62×10^0
Ru-XVIII (Lg)	3.89×10^5	2.51×10^4	5.37×10^3	1	5.37×10^3
(b) $\xi = 0.05$					
Ru-VIII (Sm)	6.61×10^3	1.73×10^{-3}	5.91×10^{-5}	75	7.79×10^{-7}
Ru-VIII (Md)	1.88×10^5	8.55×10^2	3.64×10^1	3	1.78×10^1
Ru-VIII (Lg)	4.45×10^5	2.00×10^4	9.23×10^3	1	9.23×10^3
Ru-VIII-IX (Sm)	1.69×10^4	3.26×10^{-2}	1.41×10^{-3}	29	4.65×10^{-5}
Ru-VIII-IX (Md)	1.32×10^5	3.71×10^2	1.50×10^1	3	4.92×10^0
Ru-VIII-IX (Lg)	4.08×10^5	1.13×10^4	2.32×10^3	1	2.32×10^3
Ru-IX (Sm)	9.87×10^4	1.75×10^2	5.80×10^0	6	1.13×10^0
Ru-IX (Md)	1.72×10^5	8.03×10^2	3.40×10^1	3	1.65×10^1
Ru-IX (Lg)	4.27×10^5	9.40×10^3	1.81×10^3	1	1.81×10^3
Ru-XVIII (Sm)	1.69×10^4	6.85×10^{-2}	3.02×10^{-3}	29	1.03×10^{-4}
Ru-XVIII (Md)	1.18×10^5	1.67×10^2	5.65×10^0	5	1.37×10^0
Ru-XVIII (Lg)	3.89×10^5	7.87×10^3	1.10×10^3	1	1.10×10^3
(c) $\xi = 0.01$					
Ru-VIII (Sm)	4.43×10^3	3.64×10^{-4}	2.37×10^{-4}	112	2.12×10^{-6}
Ru-VIII (Md)	1.33×10^5	2.10×10^1	3.03×10^1	3	1.01×10^1
Ru-VIII (Lg)	3.82×10^5	1.49×10^3	1.63×10^3	1	1.63×10^3
Ru-VIII-IX (Sm)	1.27×10^4	4.73×10^{-3}	3.26×10^{-3}	39	8.34×10^{-5}
Ru-VIII-IX (Md)	1.10×10^5	9.63×10^0	1.07×10^1	4	2.66×10^0
Ru-VIII-IX (Lg)	3.50×10^5	1.02×10^3	9.57×10^2	1	9.57×10^2
Ru-IX (Sm)	6.73×10^4	2.40×10^0	2.70×10^0	7	3.85×10^{-1}
Ru-IX (Md)	1.21×10^5	1.91×10^1	2.36×10^1	4	5.91×10^0
Ru-IX (Lg)	3.66×10^5	6.46×10^2	6.71×10^2	1	6.71×10^2
Ru-XVIII (Sm)	1.27×10^4	5.42×10^{-3}	3.78×10^{-3}	39	9.69×10^{-5}
Ru-XVIII (Md)	8.02×10^4	2.78×10^0	2.78×10^0	6	4.63×10^{-1}
Ru-XVIII (Lg)	3.34×10^5	5.03×10^2	5.21×10^2	1	5.21×10^2

ticularly in the regime with relatively large rotation angles, i.e., $\theta_L \gtrsim 10^{-4}$ for $p_{\text{ph}} = 10^{-3}$ and $\theta_L \gtrsim 10^{-5}$ for $p_{\text{ph}} = 5 \times 10^{-4}$.

During resource estimation in Sec. V, we estimate the physical space-time cost for both patterns and ultimately select the configuration that yields the shorter time-to-solution. A smaller logical error rate can occasionally result in a shorter runtime, as the sampling overhead from the error mitigation protocol depends on $P_L(\theta_L)$

(see Eq. (40)). For both patterns, the angular dependencies of $\alpha_{\text{RUS}}(\theta_L)$ and $C_{\text{smm}}(\theta_L)$ were determined by fitting the data presented in Fig. 9 using the cubic spline method implemented in the SciPy package [106].

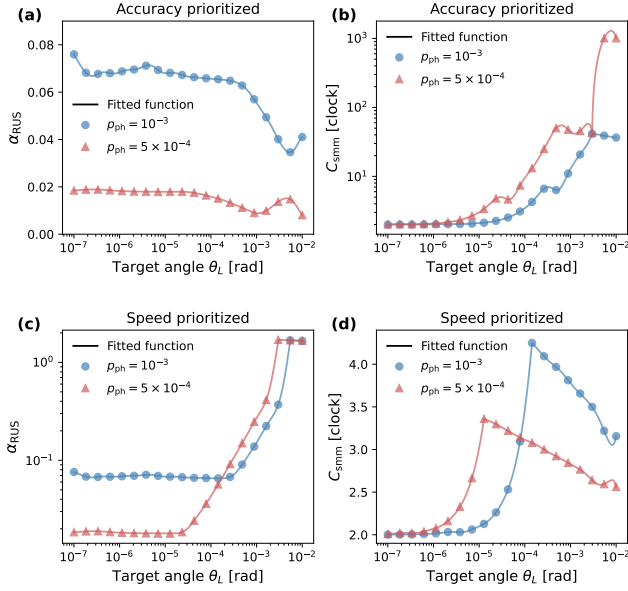


FIG. 9. Angular dependence of performance parameters for the SMM protocol. All data are obtained for a code distance of $d = 21$, with similar trends expected for other code distances. The numerical calculations utilized performance data for magic state cultivation in Ref. [85]. Blue circles (red triangles) represent the calculated data points for $p_{\text{ph}} = 10^{-3}$ ($p_{\text{ph}} = 5 \times 10^{-4}$), and solid lines indicate the cubic spline fitting curves. Panels (a) and (b) show the logical error factor $\alpha_{\text{RUS}}(\theta_L)$ and execution time $C_{\text{smm}}(\theta_L)$ in clock cycles, respectively, for the “accuracy prioritized” setting. Panels (c) and (d) display $\alpha_{\text{RUS}}(\theta_L)$ and $C_{\text{smm}}(\theta_L)$ in clock cycles for the “speed prioritized” setting.

Appendix G: Resource scaling at reduced physical error rates

In this Appendix, we present detailed resource estimates assuming reduced physical error rates of $p_{\text{ph}} = 5 \times 10^{-4}$ and $p_{\text{ph}} = 10^{-4}$. These results complement the representative values shown in Table IV and provide complete scaling trends across all benchmark systems.

Figure 10 displays the corresponding physical resource estimates for the full benchmark set as a function of the number of active orbitals N . These estimates are provided for a range of initial-state infidelity parameters $\xi \in \{0.1, 0.05, 0.01\}$. Similar to Fig. 6 (which shows results for $p_{\text{ph}} = 10^{-3}$), we plot the physical qubit requirement per QPU (Q_{QPU}), the maximum per-shot circuit execution time (\mathcal{T}_{max}), and the single-QPU time-to-solution ($\mathcal{T}_{\text{total}}$) for all molecular instances considered in this work, employing $p_{\text{ph}} = 5 \times 10^{-4}$ or $p_{\text{ph}} = 10^{-4}$. The overall scaling behaviors exhibit patterns similar to those observed in the baseline results for $p_{\text{ph}} = 10^{-3}$ (Fig. 6). However, the absolute values of Q_{QPU} and $\mathcal{T}_{\text{total}}$ are substantially lower compared to those obtained with $p_{\text{ph}} = 10^{-3}$. In contrast, the value of \mathcal{T}_{max} shows only a marginal change under reduced physical error rates. This

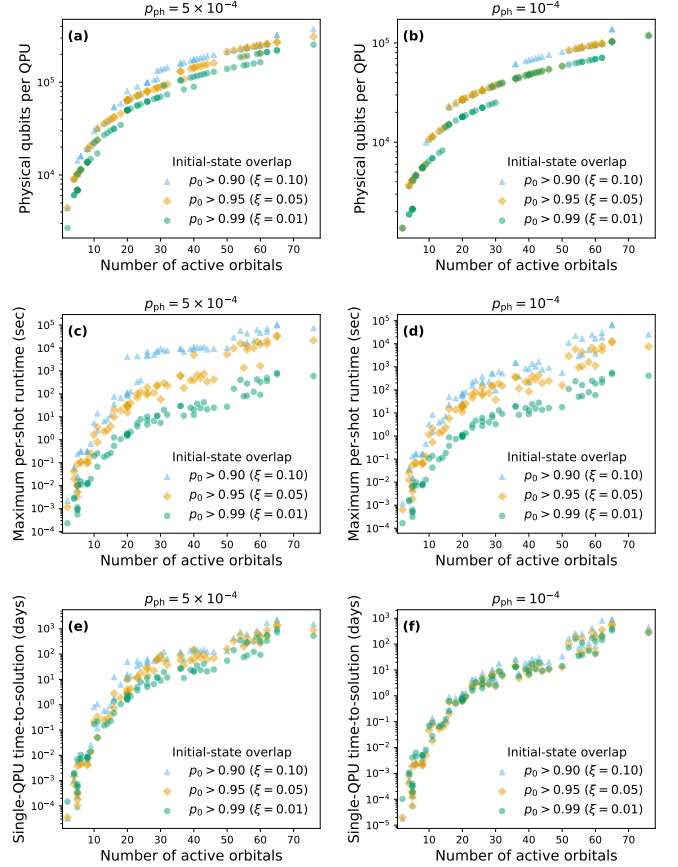


FIG. 10. Scaling of core resource components for partially randomized RPE on SMM-based partially fault-tolerant quantum computing architecture. The plots show (a,b) the number of physical qubits required per QPU, (c,d) the maximum per-shot runtime \mathcal{T}_{max} , and (e,f) the total time-to-solution assuming execution on a single QPU $\mathcal{T}_{\text{total}}$, all as a function of the number of active orbitals. For each pair, the first panel (a,c,e) corresponds to a physical error rate of $p_{\text{ph}} = 5 \times 10^{-4}$, and the second (b,d,f) to $p_{\text{ph}} = 10^{-4}$. In all panels, the shape of the markers indicates the initial-state infidelity parameter ξ , shown together with the corresponding lower bound on the initial-state overlap $p_0 = |\langle \psi_0 | \psi \rangle|^2$. Panels (c,d) and (e,f) use different time units to emphasize the distinct physical meanings of per-circuit execution cost and overall computational effort. All data points are obtained for the UWC-optimized Hamiltonian representations of benchmark molecular active-space models detailed in Appendix E 1, including hydrogen chains, iron-sulfur clusters, P450 active sites, and ruthenium-based catalysts. The target accuracy ϵ is set to be $\epsilon = 1.6$ mHa.

is because the per-shot runtime is primarily determined by the gate count, a factor largely independent of p_{ph} .

Furthermore, we highlight a crucial difference in $\mathcal{T}_{\text{total}}$ for larger orbital regimes ($N \gtrsim 50$) under higher infidelity ($\xi = 0.1, 0.05$). Unlike the exponential increase observed in Fig. 6(c) for $p_{\text{ph}} = 10^{-3}$, $\mathcal{T}_{\text{total}}$ in Figs. 10(c) and 10(f) do not exhibit such a dramatic rise in this regime. This improvement is attributed to the total logical error rate

TABLE XXI. Reference resource estimates for qubitization-based QPE, utilizing spectral amplification [26] under a full-fledged FTQC architecture. Physical qubits and time-to-solution are estimated using `Qualtran` [113] with four CCZ factories and runtime-optimized code distances. Literature values are shown in parentheses. For physical qubits, the main value denotes the total count, with a breakdown into data and factory qubits given in brackets. Minor discrepancies with literature values may arise from simplifying assumptions in `Qualtran`.

Molecule ID	Orbitals	Logical qubits	Toffoli gates	Code distance (d_1, d_2, d)	Physical qubits [Data / Factory]	Time-to-solution [hours]
$[2\text{Fe-2S}]^{-2}$	20	463	3.99×10^7	(15, 23, 27)	1.49×10^6 [1.01×10^6 / 4.81×10^5]	0.47
$[4\text{Fe-4S}]^{-2}$	36	868	1.73×10^8	(15, 27, 31)	3.03×10^6 [2.50×10^6 / 5.32×10^5]	2.05
FeMoco (Sm)	54	1132	3.42×10^8	(17, 25, 29)	3.46×10^6 (3.2×10^6 [26]) [2.86×10^6 / 6.04×10^5]	4.57 (2.7 [26])
FeMoco (Lg)	76	1454	1.00×10^9	(17, 27, 31)	4.82×10^6 (4.5×10^6 [26]) [4.19×10^6 / 6.31×10^5]	13.37 (8.6 [26])

(P_{total} , Eq. (39)) being at least one order of magnitude smaller than in the $p_{\text{ph}} = 10^{-3}$ case. Consequently, the sampling overhead of SMM (Eq. (40)) does not increase exponentially, even for the deepest circuit case of $\xi = 0.1$. These results strongly suggest that reducing the physical error rate can extend the problem size solvable within realistic time-scales and under restricted qubit budgets, potentially broadening the feasibility window shown in Fig. 7.

Appendix H: Resource estimation for full-fledged fault-tolerant quantum computing

In this Appendix, we present resource estimation results for a full-fledged FTQC setting, serving as a reference for our findings in a partially fault-tolerant setting. Specifically, we conduct resource estimation using `Qualtran` [113] for the state-of-the-art qubitization approach for molecular systems, proposed in Ref. [26].

Table XXI summarizes the estimated resources required to obtain ground-state energy estimates for representative iron-sulfur cluster models. The logical qubit count and Toffoli gate count are cited from Ref. [26]. These results were obtained by adopting the spectral amplification method for the sum-of-squares Hamiltonian representations, derived by combining double-factorized tensor hypercontraction and BLISS. The physical space-time costs (i.e., physical qubit count and time-to-solution) are estimated using `Qualtran` [113] under the AutoCCZ cost model [114]. Specifically, we assume the use of four CCZ factories with a physical error rate of $p_{\text{ph}} = 10^{-3}$, a surface code cycle time of 1 μs , and a control system reaction time of 10 μs . This setup is

consistent with that used in Refs. [23, 26]. The code distance for both distillation and data blocks is determined to minimize the total runtime cost through a grid search protocol, as implemented in `Qualtran` [113]. Here, d_1 and d_2 denote the surface-code distances used in the level-1 and level-2 magic-state distillation blocks, respectively, while d denotes the code distance for the logical data qubits implementing the algorithm.

We observe that over 1 million physical qubits are required even for the smallest $[2\text{Fe-2S}]^{-2}$ model with 20 orbitals. Notably, the majority of these are allocated to the data block, including a large amount of ancilla qubits for the qubitization protocol, which alone requires approximately one million physical qubits. This highlights that even with future improvements in magic state distillation that could reduce factory footprints, such as exemplified by magic state cultivation [85–87], the qubit requirement for data remains a formidable challenge, far exceeding tens of thousands of qubits. This indicates that conventional full-fledged FTQC necessitates millions of qubits, a significantly larger hardware scale than that of the early-FTQC setting considered in this work, as discussed in the main text. On the other hand, the time-to-solution is on the order of hours, even for the largest 76-orbital FeMoco model. This is significantly lower than that for the early fault-tolerant setting, primarily reflecting the difference in the QPE algorithms employed. The QPE protocol for the full-fledged fault-tolerant setting is executed using a single-shot measurement of a quantum Fourier transform circuit with a good input state [18]. In contrast, the single-ancilla QPE algorithms are executed via repeated measurements of the Hadamard test circuit, as described in Sec. II, thus generally requiring a longer computational time than full-fledged fault-tolerant QPE algorithms.

[1] F. Jensen, *Introduction to Computational Chemistry* (John Wiley & sons, 2017).

[2] K. D. Vogiatzis, D. Ma, J. Olsen, L. Gagliardi, and W. A. de Jong, Pushing configuration-interaction to the

- limit: Towards massively parallel MCSCF calculations, *J. Chem. Phys.* **147**, 184111 (2017).
- [3] H. Gao, S. Imamura, A. Kasagi, and E. Yoshida, Distributed implementation of full configuration interaction for one trillion determinants, *J. Chem. Theory Comput.* **20**, 1185 (2024).
 - [4] R. J. Bartlett and M. Musiał, Coupled-cluster theory in quantum chemistry, *Rev. Mod. Phys.* **79**, 291 (2007).
 - [5] A. A. Holmes, N. M. Tubman, and C. J. Umrigar, Heat-bath configuration interaction: An efficient selected configuration interaction algorithm inspired by heat-bath sampling, *J. Chem. Theory Comput.* **12**, 3674 (2016).
 - [6] G. K.-L. Chan and S. Sharma, The density matrix renormalization group in quantum chemistry, *Annual review of physical chemistry* **62**, 465 (2011).
 - [7] A. Baiardi and M. Reiher, The density matrix renormalization group in chemistry and molecular physics: Recent developments and new challenges, *The Journal of Chemical Physics* **152** (2020).
 - [8] In this work, we use the term chemical accuracy in the conventional sense of achieving energy errors of $1.6 \text{ mHa} \simeq 1 \text{ kcal/mol}$.
 - [9] Y. Cao, J. Romero, J. P. Olson, M. Degroote, P. D. Johnson, M. Kieferová, I. D. Kivlichan, T. Menke, B. Peropadre, N. P. Sawaya, *et al.*, Quantum chemistry in the age of quantum computing, *Chemical reviews* **119**, 10856 (2019).
 - [10] S. McArdle, S. Endo, A. Aspuru-Guzik, S. C. Benjamin, and X. Yuan, Quantum computational chemistry, *Rev. Mod. Phys.* **92**, 015003 (2020).
 - [11] B. Bauer, S. Bravyi, M. Motta, and G. K.-L. Chan, Quantum algorithms for quantum chemistry and quantum materials science, *Chemical reviews* **120**, 12685 (2020).
 - [12] A. Peruzzo, J. McClean, P. Shadbolt, M.-H. Yung, X.-Q. Zhou, P. J. Love, A. Aspuru-Guzik, and J. L. O'Brien, A variational eigenvalue solver on a photonic quantum processor, *Nat. Commun.* **5**, 4213 (2014).
 - [13] K. Kanno, M. Kohda, R. Imai, S. Koh, K. Mitarai, W. Mizukami, and Y. O. Nakagawa, Quantum-selected configuration interaction: classical diagonalization of hamiltonians in subspaces selected by quantum computers, *arXiv:2302.11320 [quant-ph]* (2023).
 - [14] J. Robledo-Moreno, M. Motta, H. Haas, A. Javadi-Abhari, P. Jurcevic, W. Kirby, S. Martiel, K. Sharma, S. Sharma, T. Shirakawa, I. Sitdikov, R.-Y. Sun, K. J. Sung, M. Takita, M. C. Tran, S. Yunoki, and A. Mezzacapo, Chemistry beyond the scale of exact diagonalization on a quantum-centric supercomputer, *Sci. Adv.* **11**, eadu9991 (2025).
 - [15] M. Larocca, S. Thanasilp, S. Wang, K. Sharma, J. Biamonte, P. J. Coles, L. Cincio, J. R. McClean, Z. Holmes, and M. Cerezo, Barren plateaus in variational quantum computing, *Nat. Rev. Phys.* **7**, 174 (2025).
 - [16] P. Reinholdt, K. M. Ziem, E. R. Kjellgren, S. Coriani, S. P. A. Sauer, and J. Kongsted, Critical limitations in quantum-selected configuration interaction methods, *J. Chem. Theory Comput.* **21**, 6811 (2025).
 - [17] M. Hagelueken, D. A. Kreplin, F. Wieland, M. F. Huber, and M. Roth, Exponential scaling barriers for variational quantum eigensolvers, *arXiv:2603.13073 [quant-ph]* (2026).
 - [18] A. Y. Kitaev, Quantum measurements and the Abelian stabilizer problem, *arXiv:9511026* (1995).
 - [19] S. Lee, J. Lee, H. Zhai, Y. Tong, A. M. Dalzell, A. Kumar, P. Helms, J. Gray, Z.-H. Cui, W. Liu, M. Kastoryano, R. Babbush, J. Preskill, D. R. Reichman, E. T. Campbell, E. F. Valeev, L. Lin, and G. K.-L. Chan, Evaluating the evidence for exponential quantum advantage in ground-state quantum chemistry, *Nat. Commun.* **14**, 1952 (2023).
 - [20] M. Reiher, N. Wiebe, K. M. Svore, D. Wecker, and M. Troyer, Elucidating reaction mechanisms on quantum computers, *Proc. Natl. Acad. Sci. U. S. A.* **114**, 7555 (2017).
 - [21] D. W. Berry, C. Gidney, M. Motta, J. R. McClean, and R. Babbush, Qubitization of arbitrary basis quantum chemistry leveraging sparsity and low rank factorization, *Quantum* **3**, 208 (2019).
 - [22] V. von Burg, G. H. Low, T. Häner, D. S. Steiger, M. Reiher, M. Roetteler, and M. Troyer, Quantum computing enhanced computational catalysis, *Phys. Rev. Res.* **3**, 033055 (2021).
 - [23] J. Lee, D. W. Berry, C. Gidney, W. J. Huggins, J. R. McClean, N. Wiebe, and R. Babbush, Even more efficient quantum computations of chemistry through tensor hypercontraction, *PRX Quantum* **2**, 030305 (2021).
 - [24] D. Rocca, C. L. Cortes, J. F. Gonthier, P. J. Ollitrault, R. M. Parrish, G.-L. Anselmetti, M. Degroote, N. Moll, R. Santagati, and M. Streif, Reducing the runtime of fault-tolerant quantum simulations in chemistry through symmetry-compressed double factorization, *J. Chem. Theory Comput.* **20**, 4639 (2024).
 - [25] A. Caesura, C. L. Cortes, W. Pol, S. Sim, M. Steudtner, G.-L. R. Anselmetti, M. Degroote, N. Moll, R. Santagati, M. Streif, and C. S. Tautermann, Faster quantum chemistry simulations on a quantum computer with improved tensor factorization and active volume compilation, *arXiv:2501.06165 [quant-ph]* (2025).
 - [26] G. H. Low, R. King, D. W. Berry, Q. Han, A. E. DePrince, A. F. White, R. Babbush, R. D. Somma, and N. C. Rubin, Fast quantum simulation of electronic structure by spectral amplification, *Phys. Rev. X.* **15**, 041016 (2025).
 - [27] C. Piveteau, D. Sutter, S. Bravyi, J. M. Gambetta, and K. Temme, Error mitigation for universal gates on encoded qubits, *Phys. Rev. Lett.* **127**, 200505 (2021).
 - [28] Y. Suzuki, S. Endo, K. Fujii, and Y. Tokunaga, Quantum error mitigation as a universal error reduction technique: Applications from the NISQ to the fault-tolerant quantum computing eras, *PRX Quantum* **3**, 010345 (2022).
 - [29] Y. Akahoshi, K. Maruyama, H. Oshima, S. Sato, and K. Fujii, Partially fault-tolerant quantum computing architecture with error-corrected clifford gates and space-time efficient analog rotations, *PRX Quantum* **5**, 010337 (2024).
 - [30] R. Toshio, Y. Akahoshi, J. Fujisaki, H. Oshima, S. Sato, and K. Fujii, Practical quantum advantage on partially fault-tolerant quantum computer, *Phys. Rev. X.* **15**, 021057 (2025).
 - [31] Y. Akahoshi, R. Toshio, J. Fujisaki, H. Oshima, S. Sato, and K. Fujii, Compilation of trotter-based time evolution for partially fault-tolerant quantum computing architecture, *PRX quantum* **6**, 040319 (2025).
 - [32] M.-Z. Chung, A. H. Z. Kavaki, A. Scherer, A. Khalid, X. Kong, T. Kawakubo, N. Anand, G. A. Dagnew, Z. Webb, A. Silva, G. Gyawali, T. Yan, K. Fujii, A. Ho,

- M. Mohseni, P. Ronagh, and J. Martinis, Partially fault-tolerant quantum computation for megaqubit applications, [arXiv:2603.13093 \[quant-ph\]](https://arxiv.org/abs/2603.13093) (2026).
- [33] E. Koridon, S. Yalouz, B. Senjean, F. Buda, T. E. O'Brien, and L. Visscher, Orbital transformations to reduce the 1-norm of the electronic structure hamiltonian for quantum computing applications, *Phys. Rev. Res.* **3**, 033127 (2021).
- [34] P. J. Ollitrault, C. L. Cortes, J. F. Gonthier, R. M. Parrish, D. Rocca, G.-L. Anselmetti, M. Degroote, N. Moll, R. Santagati, and M. Streif, Enhancing initial state overlap through orbital optimization for faster molecular electronic ground-state energy estimation, *Phys. Rev. Lett.* **133**, 250601 (2024).
- [35] I. Loaiza and A. F. Izmaylov, Block-invariant symmetry shift: Preprocessing technique for second-quantized hamiltonians to improve their decompositions to linear combination of unitaries, *Journal of Chemical Theory and Computation* **19**, 8201 (2023).
- [36] S. Patel, A. S. Brahmachari, J. T. Cantin, L. Wang, and A. F. Izmaylov, Global minimization of electronic hamiltonian 1-norm via linear programming in the block invariant symmetry shift (BLISS) method, *J. Chem. Theory Comput.* [10.1021/acs.jctc.4c01390](https://doi.org/10.1021/acs.jctc.4c01390) (2025).
- [37] Y. Ouyang, D. R. White, and E. T. Campbell, Compilation by stochastic hamiltonian sparsification, *Quantum* **4**, 235 (2020).
- [38] M. Hagan and N. Wiebe, Composite quantum simulations, *Quantum* **7**, 1181 (2023).
- [39] S. Jin and X. Li, A partially random trotter algorithm for quantum hamiltonian simulations, *Commun. Appl. Math. Comput.* **7**, 442 (2025).
- [40] A. Rajput, A. Roggero, and N. Wiebe, Hybridized methods for quantum simulation in the interaction picture, *Quantum* **6**, 780 (2022).
- [41] J. Günther, F. Witteveen, A. Schmidhuber, M. Miller, M. Christandl, and A. Harrow, Phase estimation with partially randomized time evolution, [arXiv:2503.05647 \[quant-ph\]](https://arxiv.org/abs/2503.05647) (2025).
- [42] M. Dobsíček, G. Johansson, V. Shumeiko, and G. Wendin, Arbitrary accuracy iterative quantum phase estimation algorithm using a single ancillary qubit: A two-qubit benchmark, *Phys. Rev. A* **76**, 030306 (2007).
- [43] N. Wiebe and C. Granade, Efficient bayesian phase estimation, *Phys. Rev. Lett.* **117**, 010503 (2016).
- [44] R. D. Somma, Quantum eigenvalue estimation via time series analysis, *New J. Phys.* **21**, 123025 (2019).
- [45] L. Lin and Y. Tong, Heisenberg-limited ground-state energy estimation for early fault-tolerant quantum computers, *PRX Quantum* **3**, 010318 (2022).
- [46] Z. Ding and L. Lin, Even shorter quantum circuit for phase estimation on early fault-tolerant quantum computers with applications to ground-state energy estimation, *PRX Quantum* **4**, 020331 (2023).
- [47] H. Ni, H. Li, and L. Ying, On low-depth algorithms for quantum phase estimation, *Quantum* **7**, 1165 (2023).
- [48] G. H. Low and I. L. Chuang, Hamiltonian simulation by qubitization, *Quantum* **3**, 163 (2019).
- [49] R. Babbush, C. Gidney, D. W. Berry, N. Wiebe, J. McClean, A. Paler, A. Fowler, and H. Neven, Encoding electronic spectra in quantum circuits with linear T complexity, *Phys. Rev. X* **8**, 041015 (2018).
- [50] H. Beinert, R. H. Holm, and E. Münck, Iron-sulfur clusters: nature's modular, multipurpose structures, *Science* **277**, 653 (1997).
- [51] J. J. Goings, A. White, J. Lee, C. S. Tautermann, M. Degroote, C. Gidney, T. Shiozaki, R. Babbush, and N. C. Rubin, Reliably assessing the electronic structure of cytochrome P450 on today's classical computers and tomorrow's quantum computers, *Proc. Natl. Acad. Sci. U. S. A.* **119**, e2203533119 (2022).
- [52] R. Toshio, S. Kanasugi, J. Fujisaki, H. Oshima, S. Sato, and K. Fujii, STAR-magic mutation: Even more efficient analog rotation gates for early fault-tolerant quantum computer, [arXiv:2603.22891 \[quant-ph\]](https://arxiv.org/abs/2603.22891) (2026).
- [53] M. Mohseni, A. Scherer, K. G. Johnson, O. Wertheim, M. Otten, N. A. Aadit, Y. Alexeev, K. M. Bresniker, K. Y. Camsari, B. Chapman, S. Chatterjee, G. A. Dagnew, A. Esposito, F. Fahim, M. Fiorentino, A. Gajjar, A. Khalid, X. Kong, B. Kulchytskyy, E. Kyoseva, R. Li, P. A. Lott, I. L. Markov, R. F. McDermott, G. Pedretti, P. Rao, E. Rieffel, A. Silva, J. Sorebo, P. Spentzouris, Z. Steiner, B. Torosov, D. Venturelli, R. J. Visser, Z. Webb, X. Zhan, Y. Cohen, P. Ronagh, A. Ho, R. G. Beausoleil, and J. M. Martinis, How to build a quantum supercomputer: Scaling from hundreds to millions of qubits, [arXiv:2411.10406 \[quant-ph\]](https://arxiv.org/abs/2411.10406) (2024).
- [54] M. Caleffi, M. Amoretti, D. Ferrari, J. Illiano, A. Manzalini, and A. S. Cacciapuoti, Distributed quantum computing: A survey, *Comput. Netw.* **254**, 110672 (2024).
- [55] R. Babbush, R. King, S. Boixo, W. Huggins, T. Khattar, G. H. Low, J. R. McClean, T. O'Brien, and N. C. Rubin, The grand challenge of quantum applications, [arXiv \[quant-ph\] 10.48550/arXiv.2511.09124](https://arxiv.org/abs/10.48550/arXiv.2511.09124) (2025).
- [56] N. Bellonzi, A. Kunitsa, J. T. Cantin, J. A. Campos-Gonzalez-Angulo, M. D. Radin, Y. Zhou, P. D. Johnson, L. A. Martínez-Martínez, M. R. Jangrouei, A. S. Brahmachari, L. Wang, S. Patel, M. Kodrycka, I. Loaiza, R. A. Lang, A. Aspuru-Guzik, A. F. Izmaylov, J. R. Fontalvo, and Y. Cao, Feasibility of accelerating homogeneous catalyst discovery with fault-tolerant quantum computers, [arXiv:2406.06335 \[quant-ph\]](https://arxiv.org/abs/2406.06335) (2024).
- [57] Y. Zhou, A. Caesura, C. Buda, X. Jackson, C. M. Abuan, and S. Guo, Assessing finite scalability in early fault-tolerant quantum computing for homogeneous catalysts, [arXiv:2511.1038 \[quant-ph\]](https://arxiv.org/abs/2511.1038) (2025).
- [58] J. Günther, T. Weymuth, M. Bensberg, F. Witteveen, M. S. Teynor, F. E. Thomasen, V. Sora, W. Bro-Jørgensen, R. T. Husstein, M. Erakovic, M. Miller, L. Weisburn, M. Cho, M. Eckhoff, A. W. Harrow, A. Krogh, T. Van Voorhis, K. Lindorff-Larsen, G. Solomon, M. Reiher, and M. Christandl, How to use quantum computers for biomolecular free energies, [arXiv:2506.20587 \[quant-ph\]](https://arxiv.org/abs/2506.20587) (2025).
- [59] M. Motta, E. Ye, J. R. McClean, Z. Li, A. J. Minnich, R. Babbush, and G. K.-L. Chan, Low rank representations for quantum simulation of electronic structure, *npj Quantum Inf* **7**, 1 (2021).
- [60] N. M. Tubman, C. Mejuto-Zaera, J. M. Epstein, D. Hait, D. S. Levine, W. Huggins, Z. Jiang, J. R. McClean, R. Babbush, M. Head-Gordon, and K. B. Whaley, Postponing the orthogonality catastrophe: efficient state preparation for electronic structure simulations on quantum devices, [arXiv:1809.05523 \[quant-ph\]](https://arxiv.org/abs/1809.05523) (2018).
- [61] S. Fomichev, K. Hejazi, M. S. Zini, M. Kiser, J. Fraxanet, P. A. M. Casares, A. Delgado, J. Huh, A.-C. Voigt, J. E. Mueller, and J. M. Arrazola, Initial state prepa-

- ration for quantum chemistry on quantum computers, *PRX quantum* **5**, 040339 (2024).
- [62] M. Mörchen, G. H. Low, T. Weymuth, H. Liu, M. Troyer, and M. Reiher, Classification of electronic structures and state preparation for quantum computation of reaction chemistry, [arXiv:2409.08910 \[physics.comp-ph\]](https://arxiv.org/abs/2409.08910) (2024).
- [63] M. Erakovic, F. Witteveen, D. Harley, J. Günther, M. Bensberg, O. R. Meitei, M. Cho, T. Van Voorhis, M. Reiher, and M. Christandl, High ground state overlap via quantum embedding methods, *PRX Life* **3**, 013003 (2025).
- [64] D. W. Berry, Y. Tong, T. Khattar, A. White, T. I. Kim, G. H. Low, S. Boixo, Z. Ding, L. Lin, S. Lee, G. K.-L. Chan, R. Babbush, and N. C. Rubin, Rapid initial-state preparation for the quantum simulation of strongly correlated molecules, *PRX quantum* **6**, 020327 (2025).
- [65] H. F. Trotter, On the product of semi-groups of operators, *Proc. Am. Math. Soc.* **10**, 545 (1959).
- [66] M. Suzuki, Fractal decomposition of exponential operators with applications to many-body theories and monte carlo simulations, *Phys. Lett. A* **146**, 319 (1990).
- [67] R. Babbush, J. McClean, D. Wecker, A. Aspuru-Guzik, and N. Wiebe, Chemical basis of trotter-suzuki errors in quantum chemistry simulation, *Phys. Rev. A* **91**, 022311 (2015).
- [68] A. M. Childs, Y. Su, M. C. Tran, N. Wiebe, and S. Zhu, Theory of trotter error with commutator scaling, *Phys. Rev. X* **11**, 011020 (2021).
- [69] B. Şahinoğlu and R. D. Somma, Hamiltonian simulation in the low-energy subspace, *npj Quantum Information* **7**, 1 (2021).
- [70] C.-F. Chen and F. G. S. L. Brandão, Average-case speedup for product formulas, *Commun. Math. Phys.* **405**, 32 (2024).
- [71] Q. Zhao, Y. Zhou, A. F. Shaw, T. Li, and A. M. Childs, Hamiltonian simulation with random inputs, *Phys. Rev. Lett.* **129**, 270502 (2022).
- [72] E. Campbell, Random compiler for fast hamiltonian simulation, *Phys. Rev. Lett.* **123**, 070503 (2019).
- [73] C.-F. Chen, H.-Y. Huang, R. Kueng, and J. A. Tropp, Concentration for random product formulas, *PRX Quantum* **2**, 040305 (2021).
- [74] K. Wan, M. Berta, and E. T. Campbell, Randomized quantum algorithm for statistical phase estimation, *Phys. Rev. Lett.* **129**, 030503 (2022).
- [75] O. Kiss, M. Grossi, and A. Roggero, Importance sampling for stochastic quantum simulations, *Quantum* **7**, 977 (2023).
- [76] E. Granet and H. Dreyer, Hamiltonian dynamics on digital quantum computers without discretization error, *Npj Quantum Inf.* **10**, 1 (2024).
- [77] C. Kiumi and B. Koczor, TE-PAI: exact time evolution by sampling random circuits, *Quantum Sci. Technol.* **10**, 045071 (2025).
- [78] A. Bocharov, M. Roetteler, and K. M. Svore, Efficient synthesis of universal repeat-until-success quantum circuits, *Phys. Rev. Lett.* **114**, 080502 (2015).
- [79] S. Bravyi and A. Kitaev, Universal quantum computation with ideal clifford gates and noisy ancillas, *Phys. Rev. A* **71**, 022316 (2005).
- [80] A. G. Fowler, M. Mariantoni, J. M. Martinis, and A. N. Cleland, Surface codes: Towards practical large-scale quantum computation, *Phys. Rev. A* **86**, 032324 (2012).
- [81] C. Gidney and A. G. Fowler, Efficient magic state factories with a catalyzed $|ccz\rangle$ to $2|t\rangle$ transformation, *Quantum* **3**, 135 (2019).
- [82] K. Temme, S. Bravyi, and J. M. Gambetta, Error mitigation for short-depth quantum circuits, *Phys. Rev. Lett.* **119**, 180509 (2017).
- [83] S. Endo, S. C. Benjamin, and Y. Li, Practical quantum error mitigation for near-future applications, *Phys. Rev. X* **8**, 031027 (2018).
- [84] D. Litinski, A game of surface codes: Large-scale quantum computing with lattice surgery, *Quantum* **3**, 128 (2019).
- [85] C. Gidney, N. Shutty, and C. Jones, Magic state cultivation: growing T states as cheap as CNOT gates, [arXiv:2409.17595 \[quant-ph\]](https://arxiv.org/abs/2409.17595) (2024).
- [86] Y. Hirano, R. Toshio, T. Itogawa, and K. Fujii, Efficient magic state cultivation with lattice surgery, [arXiv:2510.24615 \[quant-ph\]](https://arxiv.org/abs/2510.24615) (2025).
- [87] B. Hetényi, B. J. Brown, and D. J. Williamson, Constant depth magic state cultivation with clifford measurements by gauging, [arXiv:2603.05429 \[quant-ph\]](https://arxiv.org/abs/2603.05429) (2026).
- [88] A. G. Fowler and C. Gidney, Low overhead quantum computation using lattice surgery, [arXiv:1808.06709 \[quant-ph\]](https://arxiv.org/abs/1808.06709) (2018).
- [89] W. J. Huggins, T. Khattar, A. Xu, M. Harrigan, C. Kang, G. H. Low, A. Fowler, N. C. Rubin, and R. Babbush, The FLuid allocation of surface code qubits (FLASQ) cost model for early fault-tolerant quantum algorithms, [arXiv:2511.08508 \[quant-ph\]](https://arxiv.org/abs/2511.08508) (2025).
- [90] F. Arute, K. Arya, R. Babbush, D. Bacon, J. C. Bardin, R. Barends, R. Biswas, S. Boixo, F. G. S. L. Brandao, D. A. Buell, B. Burkett, Y. Chen, Z. Chen, B. Chiaro, R. Collins, W. Courtney, A. Dunsworth, E. Farhi, B. Foxen, A. Fowler, C. Gidney, M. Giustina, R. Graff, K. Guerin, S. Habegger, M. P. Harrigan, M. J. Hartmann, A. Ho, M. Hoffmann, T. Huang, T. S. Humble, S. V. Isakov, E. Jeffrey, Z. Jiang, D. Kafri, K. Kechedzhi, J. Kelly, P. V. Klimov, S. Knysh, A. Korotkov, F. Kostritsa, D. Landhuis, M. Lindmark, E. Lucero, D. Lyakh, S. Mandrà, J. R. McClean, M. McEwen, A. Megrant, X. Mi, K. Michielsen, M. Mohseni, J. Mutus, O. Naaman, M. Neeley, C. Neill, M. Y. Niu, E. Ostby, A. Petukhov, J. C. Platt, C. Quintana, E. G. Rieffel, P. Roushan, N. C. Rubin, D. Sank, K. J. Satzinger, V. Smelyanskiy, K. J. Sung, M. D. Trevithick, A. Vainsencher, B. Villalonga, T. White, Z. J. Yao, P. Yeh, A. Zalcman, H. Neven, and J. M. Martinis, Quantum supremacy using a programmable superconducting processor, *Nature* **574**, 505 (2019).
- [91] Google Quantum AI, Suppressing quantum errors by scaling a surface code logical qubit, *Nature* **614**, 676 (2023).
- [92] I. D. Kivlichan, C. Gidney, D. W. Berry, N. Wiebe, J. McClean, W. Sun, Z. Jiang, N. Rubin, A. Fowler, A. Aspuru-Guzik, H. Neven, and R. Babbush, Improved fault-tolerant quantum simulation of condensed-phase correlated electrons via trotterization, *Quantum* **4**, 296 (2020).
- [93] N. Yoshioka, T. Okubo, Y. Suzuki, Y. Koizumi, and W. Mizukami, Hunting for quantum-classical crossover in condensed matter problems, *Npj Quantum Inf.* **10**, 1 (2024).
- [94] T. W. Watts, S. Sarkar, D. Collins, N. Nguyen,

- L. Quezada, M. J. Bremner, and S. J. Elman, Rapid dissipative ground state preparation at chemical transition states, [arXiv:2602.11603 \[quant-ph\]](https://arxiv.org/abs/2602.11603) (2026).
- [95] I. Loaiza, A. Sankar Brahmachari, and A. F. Izmaylov, Majorana tensor decomposition: a unifying framework for decompositions of fermionic hamiltonians to linear combination of unitaries, *Quantum Sci. Technol.* **10**, 035035 (2025).
- [96] B. O’Gorman, W. J. Huggins, E. G. Rieffel, and K. B. Whaley, Generalized swap networks for near-term quantum computing, [arXiv:1905.05118 \[quant-ph\]](https://arxiv.org/abs/1905.05118) (2019).
- [97] J. Zhang, T.-H. Wei, X.-N. Zhuang, Z.-Y. Chen, W.-C. Kong, Y.-C. Wu, and G.-P. Guo, Low-overhead and high-fidelity preparation of logical non-clifford states with multi-level transversal injection, [arXiv:2509.23642 \[quant-ph\]](https://arxiv.org/abs/2509.23642) (2025).
- [98] Z. Pei, Z. Guo, X. Qian, and J. Liang, Error-structure-tailored early fault-tolerant quantum computing, [arXiv:2511.19983 \[quant-ph\]](https://arxiv.org/abs/2511.19983) (2025).
- [99] R. Ismail, I.-C. Chen, C. Zhao, R. Weiss, F. Liu, H. Zhou, S.-T. Wang, A. Sornborger, and M. Kojnjača, Transversal STAR architecture for megaqop-scale quantum simulation with neutral atoms, [arXiv:2509.18294 \[quant-ph\]](https://arxiv.org/abs/2509.18294) (2025).
- [100] S. Dasu, M. DeCross, A. Y. Guo, A. Lavasani, J. Behrends, A. Benhemou, Y.-H. Chen, K. Mayer, C. N. Self, S. Simsek, B. Srivastava, M. S. Allman, J. Arkininstall, J. G. Bohnet, N. Q. Burdick, J. P. Campora, III, A. Chernoguzov, S. F. Cooper, R. D. Delaney, J. M. Dreiling, B. Estey, C. Figgatt, C. Foltz, J. P. Gaebler, A. Hall, C. A. Holliman, A. A. Husain, A. Isanaka, C. J. Kennedy, Y. Kodama, N. Kotibhaskar, N. K. Lysne, I. S. Madjarov, M. Mills, A. R. Milne, B. Neyenhuis, A. J. Park, A. Ransford, A. P. Reed, S. J. Sanders, C. H. Baldwin, D. Hayes, B. Criger, A. C. Potter, and D. Amaro, Computing with many encoded logical qubits beyond break-even, [arXiv:2602.22211 \[quant-ph\]](https://arxiv.org/abs/2602.22211) (2026).
- [101] H. Leone, T. Le, S. Srikara, and S. Devitt, Resource overheads and attainable rates for trapped-ion lattice surgery, *Phys. Rev. Res.* **7**, 023088 (2025).
- [102] S. Sunami, A. Goban, and H. Yamasaki, Transversal surface-code game powered by neutral atoms, [arXiv:2506.18979 \[quant-ph\]](https://arxiv.org/abs/2506.18979) (2025).
- [103] K. Gratsea and M. Otten, Achieving utility-scale applications through full stack co-design of fault tolerant quantum computers, [arXiv:2510.26547 \[quant-ph\]](https://arxiv.org/abs/2510.26547) (2025).
- [104] S. Kanasugi, [Data and Source Code for “Enabling Chemically Accurate Quantum Phase Estimation in the Early Fault-Tolerant Regime”](https://github.com/skanasugi/chemically-accurate-quantum-phase-estimation) (2026), GitHub repository.
- [105] The ffsim developers, [ffsim: Faster simulations of fermionic quantum circuits](https://github.com/ffsim).
- [106] P. Virtanen, R. Gommers, T. E. Oliphant, M. Haberland, T. Reddy, D. Cournapeau, E. Burovski, P. Peterson, W. Weckesser, J. Bright, S. J. van der Walt, M. Brett, J. Wilson, K. J. Millman, N. Mayorov, A. R. J. Nelson, E. Jones, R. Kern, E. Larson, C. J. Carey, Í. Polat, Y. Feng, E. W. Moore, J. VanderPlas, D. Laxalde, J. Perktold, R. Cimrman, I. Henriksen, E. A. Quintero, C. R. Harris, A. M. Archibald, A. H. Ribeiro, F. Pedregosa, P. van Mulbregt, and SciPy 1.0 Contributors, SciPy 1.0: Fundamental Algorithms for Scientific Computing in Python, *Nature Methods* **17**, 261 (2020).
- [107] J. Bradbury, R. Frostig, P. Hawkins, M. J. Johnson, C. Leary, D. Maclaurin, G. Necula, A. Paszke, J. VanderPlas, S. Wanderman-Milne, and Q. Zhang, [JAX: composable transformations of Python+NumPy programs](https://github.com/pytorch/jax) (2018).
- [108] Z. Li, J. Li, N. S. Dattani, C. J. Umrigar, and G. K.-L. Chan, The electronic complexity of the ground-state of the FeMo cofactor of nitrogenase as relevant to quantum simulations, *J. Chem. Phys.* **150**, 024302 (2019).
- [109] J. Lee, D. Berry, C. Gidney, W. J. Huggins, J. R. McClean, N. Wiebe, and R. Babbush, Even more efficient quantum computations of chemistry through tensor hypercontraction, [10.5281/zenodo.4248322](https://zenodo.org/record/4248322) (2020).
- [110] P. Ollitrault, C. Cortes, J. Gonthier, R. Parrish, D. Rocca, G.-L. Anselmetti, M. Degroote, N. Moll, R. Santagati, and M. Streif, Enhancing initial state overlap through orbital optimization for faster molecular electronic ground-state energy estimation, [10.5281/zenodo.10944099](https://zenodo.org/record/10944099) (2024).
- [111] J. J. Goings, A. White, C. S. Tautermann, M. Degroote, C. Gidney, T. Shiozaki, R. Babbush, and N. C. Rubin, Data for “Reliably assessing the electronic structure of cytochrome P450 on today’s classical computers and tomorrow’s quantum computers” , [10.5281/zenodo.5941130](https://zenodo.org/record/5941130) (2022).
- [112] V. von Burg, G. H. Low, T. Häner, D. S. Steiger, M. Reiher, M. Roetteler, and M. Troyer, Quantum computing enhanced computational catalysis (Molecular integrals) , [10.5281/zenodo.4769113](https://zenodo.org/record/4769113) (2021).
- [113] M. P. Harrigan, T. Khattar, C. Yuan, A. Peduri, N. Yosri, F. D. Malone, R. Babbush, and N. C. Rubin, [Expressing and analyzing quantum algorithms with qualtran](https://arxiv.org/abs/2409.04643) (2024), [arXiv:2409.04643 \[quant-ph\]](https://arxiv.org/abs/2409.04643).
- [114] C. Gidney and A. G. Fowler, Flexible layout of surface code computations using AutoCCZ states, [arXiv \[quant-ph\] 10.48550/arXiv.1905.08916](https://arxiv.org/abs/1905.08916) (2019).